

End-to-end dosimetric verification of Cardiac Stereotactic Ablative Body Radiotherapy using a novel dynamic anthropomorphic cardiac model

*A thesis submitted to the University of Manchester
for the degree of Doctor of Clinical Science in the
Faculty of Biology, Medicine and Health*

2022

Christopher J Dean

School of Medical Sciences

Contents

Tables	5
Figures.....	7
Abbreviations	12
Abstract.....	16
Declaration.....	17
Copyright.....	17
Acknowledgments.....	18
Chapter 1: Introduction	19
1.1 The growing clinical interest in radiotherapy for cardiac indications.....	19
1.2 Existing treatments for patients with cardiac arrhythmia	21
1.3 Ablative radiation treatment for other functional pathologies.....	24
1.4 Ablative radiation treatment for cardiac arrhythmias.....	29
1.5 Risks of cardiac irradiation	31
1.6 The value of quality assurance in radiotherapy.....	40
1.6.1 The clinical importance of radiotherapy accuracy.....	40
1.6.2 Quality assurance of radiotherapy delivery accuracy.....	41
1.6.3 Dosimetric quality assurance measurement methods	43
1.6.4 Dosimetric quality assurance for SABR.....	51
1.7 Summary and Research Aims.....	56
Chapter 2: Methods	59
2.1 Phantom design & fabrication	59
2.1.1 Phantom requirements and material selection	59
2.1.2 3D computer modelling	63
2.1.3 3D Print prototyping to final phantom production and assembly.....	68
2.2 Radiochromic Film Characterisation Methodology	69
2.2.1 Introduction	69
2.2.2 Scanner configuration.....	70
2.2.3 Radiochromic film and colour channel selection for dose calibrations.....	72
2.2.4 Geometric distortion artefacts	75
2.2.5 Film post-processing	77
2.2.6 Radiochromic Film Summary and Calibration.....	78

2.3 Treatment planning	81
2.3.1 Imaging for treatment planning.....	81
2.3.2 Contouring of targets and organs at risk for treatment planning	84
2.3.3 Treatment planning objectives and evaluation metrics	86
2.3.4 Accuray CyberKnife treatment planning.....	89
2.3.5 Varian VMAT treatment planning	91
2.4 Treatment delivery.....	95
2.4.1 Accuray CyberKnife treatment delivery	95
2.4.2 Varian VMAT treatment delivery	98
2.5 Dosimetric analysis methods	101
2.5.1 Measured dose	101
2.5.2 Calculated dose	102
2.5.3 Dosimetric analyses	102
2.5.4 Measurement Reproducibility	105
Chapter 3: Results	107
3.1 Phantom design & fabrication	107
3.1.1 Material selection results.....	107
3.1.2 3D computer modelling	112
3.1.3 Prototyping to final phantom production and assembly.....	117
3.2 Radiochromic Film Characterisation	122
3.2.1 Radiochromic film colour channel for batch dose calibrations	122
3.2.2 Geometric distortion artefacts	124
3.2.3 Film dosimetric reproducibility	126
3.2.4 Overall estimate of measurement uncertainty.....	127
3.3 Treatment Planning results.....	129
3.3.1 Accuray CyberKnife	129
3.3.2 Varian VMAT	130
3.4 Treatment delivery results.....	132
Chapter 4: Discussion.....	144
4.1 Phantom design and fabrication critique.....	144
4.2 Interpretation of dosimetric verification results	148
4.3 Measurement methodology critique.....	159
4.4 Interpretation in the wider context	163
Chapter 5: Conclusions	169
References	172

Appendix I: Stakeholder engagement exercise	186
AI.1 Patty Diez interview excerpt.....	186
AI.1 Oliver Guttman interview excerpt.....	188
Appendix II: Taught Programme Elements	190

Total word count (excluding references): 35,288

Tables

	page
3.1 Relative electron densities of anatomical and analogue cardiac components based on CT scan conversion from Hounsfield Units	109
3.2 Relative electron densities for the hybrid phantom model	110
3.3 Anatomical component masks produced from the anatomical CT data using Mimics Materialise 3D modelling software. The allocated letter pertains to the position on the diagram in figure 3.3, where visible	112
3.4 Batch film calibration uncertainty characterisation	124
3.5 Calibration film reproducibility measurements	126
3.6 Planned dose statistics indicating that all treatment plans met at least the optimal dose constraints for the organs or devices at risk. Green indicates within optimal tolerance (if any) and orange indicates beyond optimal but within mandatory tolerance	129
3.7 Planned dose statistics for Varian Truebeam static plans indicating that all treatment plans met at least the optimal dose constraints for the organs or devices at risk. Green indicates within optimal tolerance (if any) and orange indicates beyond optimal but within mandatory tolerance	131
3.8 CyberKnife static summary data. Note that a maximum of 1 mm spatial correction is required in all directions	135

3.9	CyberKnife respiratory-tracked summary data. Note that a maximum of 1 mm spatial correction is required in all directions	135
3.10	Varian Truebeam static summary data. Note that a maximum of 1 mm spatial correction is required in all directions	136
3.11	Truebeam respiratory-gated summary results. Note that a maximum of 1 mm spatial correction is required in all directions	136
3.12	Table 3.12 Truebeam PTV1 end-to-end reproducibility results. Note that a maximum of 1 mm spatial correction is required in all directions and the very small range of 5%/1mm gamma pass rate results between the repeated measurements once spatial correction is applied	137

Figures

	page
1.1 Reported cardiac risk as a function of mean heart dose (Darby et. al., 2013, reproduced with permission)	33
1.2 Schematic diagram indicating the major elements in the chain in order to accurately deliver a radiotherapy plan	40
1.3 Semi-anatomical breast/chest wall phantom used in breast cancer clinical trial quality assurance (Eaton et. al., 2015, reproduced with author's permission)	44
1.4 Anatomical pelvis phantom used for audit of conformal treatment plans in the (MRC) RT01 clinical trial (Moore et. al., 2006, reproduced with author's permission)	44
2.1 3D computer modelling process flowchart to summarise the multi-step process in the production of the cardiac modular insert	65
2.2 Film cutting protocol with respect to film scanning direction. Posterior coronal plane is referred to as the AB plane and the anterior oblique plane film is the BC plane in the results section	72
2.3 Published typical pixel value to absorbed dose calibration curves, Niroomand-Rad et. al., 2020 (reproduced with author's permission)	73
2.4 Planned dose for lateral artefact testing indicating the method for producing a homogenous dose profile in the plane of interest	76
2.5 Waveform used for respiratory motion modelling, reflecting a longer period spent in end respiratory expire than in inspiration	82
2.6 CT-based contouring of normal tissues on cardiac phantom insert, A axial cross-section; B coronal. Red left ventricle, green left atrium, dark orange right ventricle, light orange aorta, cyan right atrium	85

2.7	Example targets used in this work, coronal or oblique-coronal sections left: GTV 1 and PTV 1 (VT); right: GTV 4 and PTV 4 BC plane (HOCM)	86
2.8	Organ (and device) at risk dose tolerances used in this study	88
3.1	Top: Photograph of checkerboard sample; Bottom: corresponding CT scan in water. Result demonstrated no discernible contrast horizontally between different Agilus Black rigidities, but contrast was exhibited in the vertical direction between the Vero White and the Agilus Black sections of approximately 20 - 24 HU (1 s.d. of approximately 5 HU)	108
3.2	Left: Photograph of hybrid sample; Right: corresponding CT scan. Hounsfield unit testing demonstrated contrast between the Vero White and water equivalent material of approximately 130 HU with no bleeding of one material in to the other	109
3.3	3D segmented model of anatomical heart on contrast-enhanced CT, superior-anterior-right oblique view. Labelled (where feature is visible) according to table 3.3	113
3.4	Posterior cardiac part (myocardium showing only) revealing dosimetric plane AB. Left: superior view; Right: anterior-left-superior oblique view revealing dosimetric plane AB	114
3.5	Central cardiac part (myocardium part only shown). Left: superior aspect; Right: anterior-left-superior view revealing dosimetric plane BC	115
3.6	Anterior cardiac part (myocardium part shown only). Left: superior view; Right: anterior-left-superior view revealing dosimetric plane BC	115
3.7	The final 3-part modular cardiac insert design indicating the split planes and the holes for ICD electrode positioning. Top: inferio-left lateral view; Bottom: superio-right lateral view	116

3.8	First anthropomorphic prototype. Left: 3D computer model section cut in the plane through the left ventricle and left atrium (grey) and blood pool (black); Right: a photo of the corresponding 3D printed part indicating accuracy of 3D print reproduction	117
3.9	First prototype CT scan section illustrating discernible contrast between the blood pool and myocardium elements of the structure (HU values indicated)	118
3.10	Prototype including of the addition of the extracardiac elements using Agilus Black 3D print material to surround the Vero White myocardial and vessel wall elements	119
3.11	Photograph of the insertion of the cardiac modular phantom inside the CIRS dynamic thorax phantom viewed from the superior aspect of the phantom. Note the goodness of fit both between modular components and between the insert and the thorax outer phantom	120
3.12	CT images of phantom: Left: axial cross-section indicating the AB and BC planes; Right: coronal view. Both planes indicate high quality of fit between the modules and with the thorax phantom. Also demonstrated is adequate image contrast between the cardiac and non-cardiac elements and the appropriate relative anatomical size and positioning with respect to the remainder of the thorax	121
3.13	Differences in dose calibration relationships between radiochromic film types for the green channel. Points are calibration values, dotted line 6 th order polynomial	122
3.14	First derivative of figure 19 indicating differences in film sensitivity between EBT-3 and EBT-XD radiochromic film as a function of absorbed dose, both for single (green) channel, polynomial trendline	123
3.15	Lateral film response to a homogeneous dose of radiation. Note the small magnitude systematic variation across the width of the scanner and edge of film effects	125

3.16	Example calculated dosimetry for left: PTV 1 (VT), right: PTV 4 (HO�M). Red semi-transparent structure indicates PTVs, pink structure indicates heart with PTV subtracted, isodoses listed	130
3.17	An example of a good pass (PTV1 BC plane CyberKnife dynamic). Top: gamma map overlay (5%/1mm global criterion applied); Middle: isodose overlay; Bottom: 1D profile overlay (black calculated dose, purple measured dose)	133
3.18	An example of a poor initial pass (PTV 4 AB plane Truebeam dynamic): Craniocaudal profiles displayed. Top prior to spatial correction; bottom following spatial corrections of 1 mm in craniocaudal and out-of-plane directions. Black line is calculated dose, purple line is measured dose. Blue indicates measured dose lower than calculated, red indicates measured dose higher than calculated, gamma criterion 5%/1mm applied	134
3.19	Box and whisker plot 5%/1mm gamma pass-rates prior to spatial correction. Note the low median pass rate (87.7%) and high variability for all delivery techniques	137
3.20	Box and whisker plot of 5%/1mm gamma pass-rates following applied spatial corrections. Note the resulting improvement in gamma pass rates (median 99.4%) and significant reduction in variability for each delivery technique	138
3.21	Histogram detailing corrections required in transverse direction. Note the maximum correction of 1 mm. Median for each group within 0.5 mm	139
3.22	Histogram detailing corrections required in craniocaudal direction. Note the maximum correction of 1 mm. Median for each group within 0.5 mm, excepting Truebeam dynamic data which indicates skew towards the positive craniocaudal direction with a median correction required of +1 mm	139

3.23	Histogram detailing corrections required in the out-of-plane direction. Note the closely grouped data in absolute terms. Median for each group within 0.5 mm	140
3.24	Mean dose differences between measured and calculated dose for doses above prescription dose (or above 80% of planar maximum dose) following small spatial corrections	140
3.25	Improvement in 5%/1mm global gamma pass rate as a result of small spatial corrections as a function of out-of-plane dose gradient. Indicates a signal for sensitivity. Linear trendlines	141
3.26	Apparent dose magnitude error for PTV1 AB plane CyberKnife dynamic delivery that did not diminish with simple spatial correction. Top: 5%/1mm gamma map, bottom: 1D left-right profile. Red indicates measured dose higher than calculated, blue dots indicate measured dose lower than calculated. Note how the dose difference appears to be a function of position on the left-right axis	142
3.27	Apparent dose magnitude error for PTV3 BC plane CyberKnife dynamic delivery that did not diminish with simple spatial correction. Top: 5%/1mm gamma map, bottom: 1D profile. Note how the dose difference appears to be a function of position on the left-right axis	143

Abbreviations

.flm	film (text file) format for SNC Patient software
.tif	Tagged Image File format
1D	One-dimensional
2D	Two-dimensional
3D	Three-dimensional
3DCT	3-dimensional Computed Tomography
3DOF	Three degrees of freedom
4DCT	four-dimensional computed tomography
6DOF	Six degrees of freedom
AAA	Analytical Anisotropic Algorithm
AAPM	American Association of Physicists in Medicine
AF	Atrial Fibrillation
AV (node)	Atrio-ventricular (node)
AVM	Aterio-venous malformation
CBCT	Cone beam computed tomography
cm	centimetres
Co-60	Cobalt-60
CT	Computed tomography
CVA	Cerebrovascular Accident
D _{xx cc}	Minimum dose received in a volume of xx cubic centimetres
DECT	Dual-energy CT
DICOM	Digital Imaging and Communications in Medicine
dpi	dots (pixels) per inch
E2E	end-to-end
EORTC	European Organisation for Research and Treatment of Cancer
EPID	Electronic Portal Imaging Dosimetry (Detector)
EQUAL	ESTRO Quality Assurance Network for Radiotherapy

ESTRO	European Society for Therapeutic Radiation Oncology
FFF	Flattening-Filter-Free
GTV	Gross Target Volume
Gy	Gray
HOCM	Hypertrophic obstructive cardiomyopathy
HR	Hazard ratio
HU	Hounsfield Unit
IAEA	International Atomic Energy Agency
ICD	Implanted cardioverter device
iDMS	Integrated Data Management System
IGRT	Image guided radiotherapy
ITV	Internal Target Volume
IVD	In vivo dosimetry
kV	Kilovoltage
LA	Left atrium
LAD	Left Anterior Descending
LD _{xx}	The Lethal Dose to reduce the proportion of surviving cells by xx %
LED	Light Emitting Diode
LV	Left ventricle
mAs	milliamp-seconds
MDA/IROC	MD Anderson / Imaging and Radiation Oncology Core
MI	Myocardial infarction
MLC	Multi-leaf collimator
mm	millimetres
MOSFET	Metal Oxide Semiconductor Field Effect Transistor
MRI	Magnetic Resonance Imaging
MU	Monitor Unit
MV	Megavoltage
MVD	Microvascular Decompression

NHS	National Health Service
NICE	National Institute for Health and Care Excellence
NSCLC	Non-small cell lung cancer
NTO	Normal Tissue Optimiser
OAR	Organ at Risk
OD	Optical Density
OS	Overall survival
PDD	Percentage depth dose
PRV	Planning Risk Volume
PTV	Planning Target Volume
PV	Pixel Value
QA	Quality Assurance
R&V	Record and verify
RA	Right atrium
RF	Radiofrequency
ROSE	Radiosurgery or Open Surgery for Epilepsy (clinical trial)
RTTQA	Radiotherapy Trials Quality Assurance Group
RV	Right ventricle
s	seconds
s.d.	standard deviation
SABR	Stereotactic Ablative Body Radiotherapy
SA	Sino-atrial (node)
SECT	Single-energy CT
SRS	Stereotactic Radiosurgery
SSD	Source-to-Surface Distance
SVC	Superior vena cava
TG	Task Group (of the AAPM)
TLD	Thermo-luminescent dosimeter
TMR	Tissue Maximum Ratio

TN	Trigeminal Neuralgia
TPS	Treatment Planning System
TROG	Trans-Tasman Radiation Oncology Group
UK	United Kingdom
$V_{xx\text{ Gy}}$	Volume of the structure receiving xx Gy or more
VMAT	Volumetric Modulated Arc Therapy
VT	Ventricular tachycardia
WBRT	Whole brain Radiotherapy

Abstract

Introduction

Clinical evidence demonstrating the potential of SABR to treat cardiac arrhythmic indications is growing. Despite additional risks arising from the challenging nature of cardiac SABR and a strong history of quality assurance in radiotherapy, there remains a scarcity of evidence demonstrating end-to-end dose delivery accuracy for this novel indication.

Methods

An anthropomorphic cardiac insert was produced to measure dose delivery accuracy in cardiac SABR using radiochromic film. Radiotherapy treatment plans reflective of clinical cardiac SABR practice were examined for the CyberKnife VSI and Varian Truebeam platforms, including respiratory tracking and gating, respectively.

Results

For all techniques and platforms, maximal spatial corrections of 1 mm were required in up to three orthogonal directions to achieve median global gamma 5% / 1 mm pass-rates above 99 %. Following spatial correction, median doses were within 2.5 % (Varian Truebeam) and 1.5 % (Accuray CyberKnife) of calculated dose. Gamma pass-rates were sensitive to high out-of-plane dose gradients, which must be considered when assessing 3D plan delivery accuracy with 2D methodology.

Conclusions

Cardiac SABR dosimetric accuracy is deliverable to levels commensurate with the requirements of this indication even when employing sophisticated respiratory motion management techniques. These techniques should be explored further to reduce the treated volume. This methodology facilitates direct, independent system accuracy quality assurance for cardiac SABR which, if utilised by centralised quality assurance services, could benefit standardisation and the establishment and maintenance of minimum quality standards for future cardiac SABR clinical trials and beyond.

Declaration

The author of this thesis declares that no portion of the work referred to in the thesis has been submitted in support of an application for another degree or qualification of this or any other university or other institute of learning.

Copyright

The author of this thesis (including any appendices and/or schedules to this thesis) owns certain copyright or related rights in it (the “Copyright”) and he has given The University of Manchester certain rights to use such Copyright, including for administrative purposes.

Copies of this thesis, either in full or in extracts and whether in hard or electronic copy, may be made only in accordance with the Copyright, Designs and Patents Act 1988 (as amended) and regulations issued under it or, where appropriate, in accordance with licensing agreements which the University has from time to time. This page must form part of any such copies made.

The ownership of certain Copyright, patents, designs, trademarks and other intellectual property (the “Intellectual Property”) and any reproductions of copyright works in the thesis, for example graphs and tables (“Reproductions”), which may be described in this thesis, may not be owned by the author and may be owned by third parties. Such Intellectual Property and Reproductions cannot and must not be made available for use without the prior written permission of the owner(s) of the relevant Intellectual Property and/or Reproductions.

Further information on the conditions under which disclosure, publication and commercialisation of this thesis, the Copyright and any Intellectual Property and/or Reproductions described in it may take place is available in the University IP Policy (see <http://documents.manchester.ac.uk/DocuInfo.aspx?DocID=24420>), in any relevant Thesis restriction declarations deposited in the University Library, The University Library’s regulations (see <http://www.library.manchester.ac.uk/about/regulations/>) and in The University’s policy on Presentation of Theses.

Acknowledgments

I would like to take this opportunity to thank the people that have enabled this research. Firstly, I would like to thank staff in the Clinical Physics department at Barts Health, namely Fraser Warren, Nathan Niemann and Paul Barry; without their specialist expertise in 3D design, printing and engineering it would not have been possible to produce the cardiac insert and perform the modification to the existing thorax phantom. Secondly, I would like to thank staff in Newcastle and Middlesbrough for providing advice on typical cardiac SABR targets. Thirdly, thanks go to all the staff in the Barts Health Radiotherapy Physics department that have provided direct support in allowing me the time and space to complete this research, but specifically to Dr Niall MacDougall of Barts Health and Dr Michael Taylor of the University of Manchester for their project supervision and Dr Alison Starke for proofing. Finally, I would like to thank my partner Elliott for his patience during this research and my incredible family, especially my mum and my nan. It is clear to me that without their positivity, encouragement and unwavering support through the years, I would never have got to this point. For that, I am truly grateful.

Chapter 1: Introduction

1.1 The growing clinical interest in radiotherapy for cardiac indications

Radiotherapy is a therapeutic option for many patients with solid malignant tumours in both the radical (curative) and palliative setting. It is a loco-regional treatment that combines high-quality pre-treatment imaging and the use of sophisticated computer systems that enable the precise design of high energy x-radiation external beam delivery of therapeutic dose to deep-seated tumours. Ionising radiation cannot be delivered only to the target, and so there is always a degree of collateral damage to surrounding normal tissues. In the curative setting this is usually the limiting factor in determining the maximum treatment (prescription) dose deliverable. The adoption of a fractionated approach, meaning delivering a proportion of the planned total dose daily allows for normal tissues to recover to a clinically acceptable level between fractions whilst simultaneously providing adequate cumulative tumour cell-kill to reduce tumour cells to a nonviable number.

By contrast, Stereotactic Ablative Radiotherapy (SABR) is a form of radiotherapy that delivers a much higher absorbed dose per fraction to the target over a very small number of fractions (1-8 typically) (Halvorsen, 2017). This technique has seen increasing popularity in the oncology community because of increasingly sophisticated radiation delivery methods available that are able to deliver extremely high dose-gradients between the target periphery and the surrounding normal tissues, and high precision target localisation techniques using image guidance (Benedict et. al., 2010,

for the American Association of Physicists in Medicine). These combined approaches mean that the extremely high fractional doses to surrounding normal tissues are minimised to an acceptable level whilst delivering a high biologically effective dose to the cells within the target (Timmerman, 2008). Although SABR has been delivered clinically for more than two decades (Timmerman et. al., 2003, Onishi et. al., 2004), only very recently has evidence for SABR reached the highest levels for primary NSCLC (Ball et. al., 2019) and oligometastatic disease (Palma et. al., 2018, Gomez et. al., 2016).

The efficacy and precision of SABR for both malignant and functional pathologies have not gone unnoticed by the Cardiology community, who show an increasing interest in its ablative ability for the treatment of cardiac arrhythmia (Zei & Mac, 2019) that are refractory to traditional treatment methods. SABR is potentially advantageous compared with current interventions for cardiac pathologies, but this new indication comes with its own risks that are borne out of the associated complex cardiac target shapes and novel localisation methods. The quality of dose targeting is likely to dictate the treatment efficacy whilst other aspects of dosimetric quality are potential predictors for radiation-related cardiac sequelae and so the accurate treatment planning system modelling of cardiac doses are likely to be important as its use increases.

1.2 Existing treatments for patients with cardiac arrhythmia

Cardiac arrhythmia covers a range of conditions arising from abnormal electrophysiological patterns throughout the myocardium. These commonly arise at the site of a prior myocardial infarction (MI) where vascular occlusion in the coronary arteries causes oxygen deprivation in the myocardium downstream of the affected vessel. Ventricular tachycardia (VT) is a debilitating clinical condition that arises from the abnormal electrophysiology which causes rapid, asynchronous contraction of the inferior chambers of the heart which can dramatically reduce cardiac output and lead to catastrophic consequences for the individual.

The current recommendation (Priori et. al., 2015) for patients with symptomatic cardiac arrhythmia such as VT, amongst others, is management with first line anti-arrhythmic drugs. These include negative inotropic and chronotropic drugs such as a beta-blocker, a non-hydropyridine calcium blocker, or verapamil (Pedersen et. al., 2014). However, a significant proportion of patients have persistent (drug-refractory) symptoms, find their side-effects intolerable or see an exacerbation in arrhythmic events. For those patients where drug therapy fails to relieve symptoms, invasive treatment by means of catheter ablation is recommended as the next line of therapy (Priori et. al., 2015).

Catheter ablation can be performed either by injecting radiofrequency (RF) energy or by injecting alcohol to the arrhythmogenic site, both of which carry a significant risk of post-intervention early mortality rate. For RF ablation, Satangeli (2017) report the risk as 5%, and for ethanol ablation the mortality risk is reported as approximately 1% (Gianni et. al., 2017, Veselka et. al., 2017); the main causes being vascular injury from

the catheter placement, haemorrhage, coronary artery dissection, myocardial infarction from alcohol escaping from the septal branch and subsequent cerebrovascular accidents (CVA).

In addition to the significant complication risk from catheter-based ablative procedures, there is a significant procedural failure rate of more than 50% across arrhythmic indications in providing a medium-to-long term alleviation of symptoms (Chen et. al., 2018, Sapp et. al., 2016, Jin et. al., 2017, Stephenson et. al., 2008). This failure rate appears both consistent and persistent despite combining sophisticated fluoroscopic and echocardiographic imaging techniques during the procedure along with pre-intervention cardiac MRI.

Procedural failure is usually a result of anatomical challenges; either due to inaccurate or incomplete localisation of the arrhythmogenic region or due to larger (thicker) or inaccessible targets that are beyond the anatomical reach of epicardial catheter ablation. Whichever the cause, the outcome is the same in that the region will be incompletely ablated and so the invasive procedure will ultimately be ineffective (Cuculich et. al., 2017, Zei & Mak 2019, Gianni et. al., 2017).

Patients that experience catheter ablation failure for VT and AF will go on to experience defibrillation from their implanted cardioverter device (ICD) to reset the cardiac muscle to a sinus rhythm and avoid haemodynamic collapse and likely resulting death. Although the activation of the device reduces the acute risk of death during each episode of VT, the psychological effects of high levels of defibrillation can be damaging (Dunbar et. al., 2012). For those patients that experience an early recurrence

of VT following attempted interventional treatment, the median time to death is around 2 years (Jin et. al., 2017).

Despite the high failure rate and associated complications associated with this invasive catheter ablation, in the absence of anything superior it is currently the most attractive option for patients with refractory arrhythmia. Sapp et. al. (2016) demonstrated in a phase III setting that ablative therapy was more effective than escalation to second line drug therapy in reducing subsequent patient mortality, ICD shock or VT storm. As a result, the breadth of indications for catheter ablation beyond VT is growing, with positive results emerging for the treatment of Atrial Fibrillation (AF) by treatment of the pulmonary vein ostia (Pappone et. al., 2000) and hypertrophic cardiomyopathy (Zhao et. al., 2016).

1.3 Ablative radiation treatment for other functional pathologies

Although SABR is a relatively recent advancement in treatment of malignant extracranial lesions with ablative doses of radiation, its development is a direct evolution of the treatment of intracranial lesions using Stereotactic Radiosurgery (SRS). Historically, this technique has employed a large number of very small, well-collimated radiation beams, co-focal upon the target using highly precise localisation. This technique allows for an ablatively high dose to be delivered to the target whilst minimising dose beyond to an acceptable level beyond the target surface.

The effectiveness of this ablative radiation technique has been evidenced over decades and compares well with other non-ablative techniques in the malignant setting. Brown et. al. (2016) evidenced equivalence in overall survival with less cognitive deterioration compared with whole brain radiotherapy (WBRT) for cerebral metastases, echoing earlier prospective but non-randomised large data from Yamamoto et. al. (2014). Saghal et. al., 2015 also found in their systematic review of randomised data that patient overall survival is improved with SRS alone compared with additional WBRT for patients under 50 years old corroborating earlier non-randomised data from Halasz et. al. (2016). However, in addition to treatment of such malignant lesions, there exists varying levels of evidence of its use in several non-malignant functional conditions, with varying degrees of clinical adoption.

The largest body of evidence for SRS in the treatment of functional pathologies exists for arterio-venous malformation (AVM) which results in a series of tightly packed connecting feeding and draining vasculature without a capillary bed (a nidus). Without

treatment of a ruptured AVM there is an increasingly large risk of catastrophic haemorrhage as a result of aneurysm.

The majority of SRS ablation has been using the GammaKnife platform, delivering approximately 25Gy to the periphery of the lesion in a single fraction, with approximately double this dose internally. The ablative mechanism is thought to be initial endothelial cell damage followed by thrombosis and necrosis, and it is reported to have the lowest rate of intervention-based mortality (0.5 per 100 patient-years) compared with surgery or endovascular embolization and similar levels of haemorrhage complication rates to endovascular embolization (1.7 per 100 patient-years) (Kim et. al., 2014).

Apart from its attractive relative complication risk compared with embolization, the success of SRS is likely to be at least partly due its ability to localise the nidus by external image guidance (using the bony superficial anatomy of the skull) for all treatment platforms rather than relying on anatomically-determined catheter access through the tortuous surrounding vascular architecture; this means that its ablative success is much less reliant upon good access to the nidus target from interventional catheter ablation, which is recognised in the current NHS England Commissioning Policy (2013).

Trigeminal neuralgia (TN) is a second functional clinical condition that affects the V cranial nerve typically causing severe, sudden, but short-lived episodes of pain originating in the face (Merskey et. al., 1986). Despite the quality of evidence being

low (Zhang, 2013), the current first line therapy for TN is in the form of Carbamazepine or Gabapentin medical therapy which, interestingly in addition to being used for neuropathic pain are used in the treatment of epilepsy. Fields (1996) estimated that one patient in four would be refractory to drug therapy in this setting.

Its usual aetiology is one of nervous compression and subsequent demyelination from the adjacent superior cerebellar artery (Fields, 1996). Akin to AVM treatment, microvascular surgery to physically separate the vessel from the demyelinated nerve is relatively successful with 10-year pain- and medication-free rates reported around 70% (Barker 1996); however, this method also exhibits complication risks including partial facial paralysis, cranial haematomas, cerebrospinal fluid leakage and meningitis from the interventional approach.

Guidelines produced by National Institute for Health and Care Excellence in the UK and the International Radiosurgery Association (2009) both advocate consideration of SRS where pharmaceutical therapies have failed and in patients that are not suitable for microvascular decompression (MVD), or where previous decompression surgery has failed. This is reflected in the current NHS England commissioning policy for this indication (2013). SRS treatment is usually prescribed as 35-50Gy at the periphery of the target which in this case is the V cranial nerve itself at the location of the compression.

Finally, from a functional perspective, there is a long investigation history for the efficacy of SRS in the treatment of epilepsy. In the late 1990s, a group was examining

the second order effect of the radiation treatment of cerebral tumours that were thought to be causing epilepsy. Schrottner et. al. (1998) observed that patients that received higher intermediate doses outside the solid tumour target, and those that had tumours in the medial lobe suffered fewer epileptic events following SRS treatment. This initial work was broadened by Régis et. al. (1999) who examined the effects of delivering SRS to seven patients with drug-refractory epilepsy originating from the mesial-temporal lobe in the absence of solid tumours that were in Schrottner's group. Initial results indicated resulting clinical benefit as six of the seven patients were seizure-free following treatment even in the absence of a space occupying lesion.

Despite its apparent success in reducing seizure numbers, McDonald et. al. (2004) followed three patients after SRS and documented significant verbal memory decline and oedema compared with pre-treatment baseline, which they interpreted as being due to collateral radiation effects in the 2-year follow up period. Régis also ran a multi-centre prospective trial following 21 patients with a mean peripheral dose of 24 Gy and demonstrated a seizure-cessation rate of 65% at 2 years minimum follow up but did acknowledge the delay to clinical benefit with SRS compared with an almost immediate result from MVD. The longer-terms effects were corroborated by Bartolomei et. al. (2008) following patients over six years found long-term success in reducing seizures, but also observed a mean delay to seizure cessation of 12 months from treatment.

Although SRS in the treatment of epilepsy is not yet commonplace worldwide, there is a growing interest in this field of functional treatment compared with gold standard

MVD surgery. Surgery is expensive and comes with a mortality risk of 0.2% and 2% for serious permanent complications alongside neurocognitive decline risk of 10-60% when operating on the dominant hemisphere (Quigg & Harden 2014). When the risks of SRS – a non-invasive, less costly alternative – treatment are put into context with surgery in the elective treatment context, it is understandable that there is an appetite to consider focal irradiation in the Phase III setting. The ROSE (Radiosurgery or Open Surgery for Epilepsy), which closed to recruitment in 2016 was designed specifically to definitively answer the question of relative clinical efficacy in patients with drug refractory epilepsy. Results indicate that SRS is non-inferior to open surgery as an effective treatment for epilepsy (Barbaro et. al., 2018).

There exist many examples of clinical successes from delivering non-invasive therapy via ablatively high doses of radiation in the treatment of functional conditions in the intracranial setting that have the additional benefit of not being subject to the limitations of surgical or a catheter interventional approach. Although most of the treatments to date have been performed using dedicated stereotactic platforms such as Elekta Gamma Knife using fixed geometry stereotactic frames or Accuray CyberKnife which uses imaging for target localisation, the data is compelling that high-energy high-dose stereotactic radiotherapy is a successful therapeutic option for a number of existing functional indications.

1.4 Ablative radiation treatment for cardiac arrhythmias

As early as 2010, a pre-clinical study (Sharma et. al., 2010) had shown positive results in producing an accurately positioned myocardial scar in porcine hearts. The pigs were imaged for treatment with CT and underwent electrophysiological mapping prior to delivery of image-guided SABR with dose escalation . The group inferred that by delivering a dose of at least 25Gy to the periphery of the intended site, a functional change in the electrophysiology would result in that region (cavotricuspid isthmus block or AV nodal block) 90 days after irradiation without the induction of spontaneous arrhythmias. The accuracy of the location and the histology of the scar was confirmed following the sacrifice of the animals and myocardial samples taken for examination.

Blanck et. al. (2014) performed a similar study to the Sharma group but dose escalated from range 17.5Gy to 35Gy in 2.5Gy increments and inferred from their scar scoring system that 32.5Gy was required to produce adequate functional changes in electrophysiology in porcine myocardia. Despite this finding, Loo et. al. (2015) went on to deliver 25Gy to the periphery of human heart arrhythmogenic regions that were causing episodes of sustained VT in the first reported study of this kind. Target definition was performed using pre-treatment electrophysiological mapping on the patient's anatomical CT scan. SABR was delivered using a CyberKnife (Accuray Inc, Sunnyvale CA) using respiratory motion compensation. The authors reported no acute complications and a significant reduction in the number of episodes of VT following the irradiation. Although this case study provided proof of concept in the human setting for the first time, it was severely very limited in its generalisable conclusions due to the single patient nature of the study.

This limitation was overcome by Cuculich et. al. (2017) whose group treated 6 patients with SABR for VT using a similar pre-treatment target definition method but without respiratory compensation at treatment meaning the volumes of the patient treated to high doses were significantly larger than the patient in the Loo (2015) study. Despite these major differences in the delivery method, the functional patient outcomes remained impressive with the authors reporting an acute reduction of more than 99% in episodic frequency of ICD-detected VT events requiring defibrillation following cardiac SABR treatment.

More recently, a very limited number of UK institutions have worked to the first clinical services for cardiac SABR in collaboration with the Cuculich group in order to offer cardiac SABR for patients with drug-refractory VT (Lee et. al., 2021).

The time between treatment and functional change for cardiac SABR is similar to those seen previously in the radiation treatment of for epilepsy and AVM indicating a similar underlying subacute biological process; unlike the immediate effects of catheter ablation. Pre-existing data indicating pro-fibrotic cytokines are secreted from neutrophils which are recruited to irradiated tissues (Cuomo et. al., 2016) are useful in providing a potential theoretical mechanism for this functional transition as it is known that fibrotic tissues are electrically inert. This theory is corroborated by the post mortem histological specimens from participants in the Cuculich (2017) study. In all cases, these histologies demonstrated high levels of microscopic fibrosis in the target volumes, which would result in beneficial macroscopic electrophysiological changes.

1.5 Risks of cardiac irradiation

Because the heart is primarily comprised of endothelial and connective tissue with a low proliferation rate, it was considered a largely radio-resistant organ until the 1960s. However, a case report from Cohn et. al., (1967), the first to suggest a link between irradiation and atherosclerosis in humans, led others such as Stewart & Fajardo (1978) to begin the exploration of causation. However, they found no causation and instead suggested “careful long-term cohort or case control study... will be necessary.” The first piece of convincing evidence was published in 1989 from such a ‘careful’ study of 40 children treated with mediastinal radiotherapy for Hodgkin’s Lymphoma (Joensuu, 1989). Although only a single arm observational study, two children developed MI before they reached 30 years old (between 1- and 4-years post irradiation) which, set against an extremely low baseline event rate, led the authors to a conclusion of likely radiation-based cause.

As breast cancer and Hodgkin’s Lymphoma patients began to live longer through the 1980s due to improvements in the quality of their treatment, there was a continued interest in the potential mechanisms of causation for cardiac radiation toxicity, and whilst the review by Corn et. al. (1990) acknowledged there had been improvements in thoracic radiation delivery methods, their work evidenced animal model links between irradiation and changes in the cardiac microvascular environment and cholesterol feeding.

The second observable risk from cardiac irradiation is that of acute pericarditis. The Stanford group (Carmel & Kaplan, 1976) studied 377 patients treated for Hodgkin’s Lymphoma with mantle (mediastinal lymph node irradiation) fields and noted a

statistically significant elevation in the rate of pericarditis in those patients that did not receive subcarinal radiation shielding compared with those that did (20% vs. 7%, respectively). Further, when stratified by dose to the whole pericardium, rates of pericarditis increased from 7% for <6Gy to 50% for >30Gy although perhaps interestingly for this cohort, there was only one patient that was reported to have died of MI 5 years post irradiation.

Retrospective epidemiological studies designed to examine the dose-response relationship in long-term surviving breast cancer patients that received much more modest radiation doses than those receiving mantle treatments have also indicated an increase in relative risk for cardiac events. The large Danish retrospective series studying 35,000 women over 20 years following irradiation for breast cancer (Møller et. al., 2008) suggest a 30% relative risk elevation of cardiac event for left-sided breast cancer patients compared with right-sided breast cancer patients which provides a signal for an association. However, these studies were not able to adequately examine the difference in magnitude of radiation dose or dose position between groups.

More recently, an international group led by Carlson et. al. (2021) and the WECARE Collaborative Group published a population-based retrospective study of over 1500 women under 55 years treated with left- or right-sided radiation therapy for breast cancer between 1985 and 2008 examining long-term cardiac events. This work found, in this younger population, almost a doubling of absolute risk of cumulative cardiac events in the left-breast radiotherapy group compared with the right-breast radiotherapy group (10.5% compared with 5.8%, respectively).

Darby et. al., 2013 examined retrospectively, but in more detail, the position and magnitude of the radiation with respect to the heart using historical records and reported a 7% increase in the risk of a major coronary event per Gray of mean absorbed dose (figure 1.1).

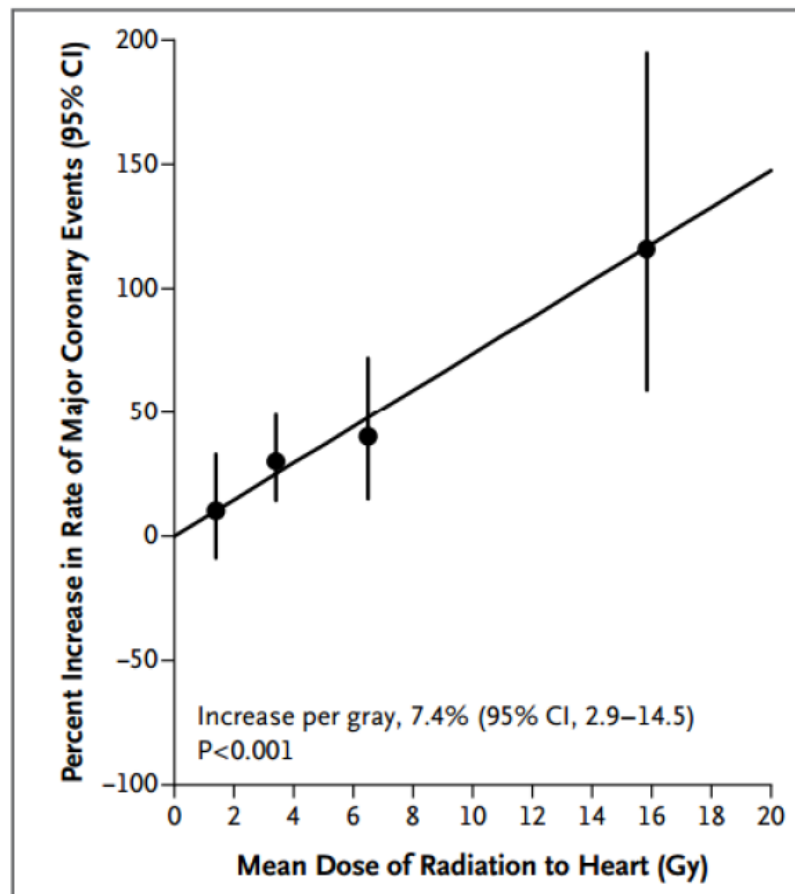


Figure 1.1 Reported cardiac risk as a function of mean heart dose (Darby et. al., 2013, reproduced with permission)

This linear model, however, has large uncertainties indicated and is very sensitive to the accuracy of the 16 Gy data point which arises largely from patients receiving irradiation to the inframammary lymph node chain that lies in very close proximity to

the heart. These features of the data mean that it could be argued that the proposed linear dose response is not in fact linear below mean cardiac doses of 8 Gray.

More recently, the RTOG0617 randomised controlled trial comparing standard- vs. high-dose chemoradiotherapy for non-small cell lung cancer (NSCLC) suggested that the volume of heart receiving at least 5 Gy and 30 Gy were predictive of overall survival (Bradley et. al., 2015).

Johnson-Hart (2018) has also recently retrospectively examined the importance of minimising dose to the heart when treating thoracic tumours. Their study follows 780 NSCLC and oesophageal cancer patients, overall survival was lower when the treatment was delivered closer to the patient midline than planned. Hazard ratios are reported to be 1.09 for NSCLC and 1.16 for oesophageal patients, both reaching the authors' set levels for statistical significance. These data are rather blunt and exploratory but again provide a signal that subtle increases in dose to the heart over heavily fractionated regimes may have detrimental effects on non-cancer specific survival for irradiated patients.

These data are somewhat corroborated by more contemporary studies aimed at finding dosimetric predictive factors for death. Speirs et. al., 2017 via multivariate analysis discovered the predictive effects of heart volumes receiving at least 50 Gy negatively affecting overall survival. Stam et. al. (2017a) noted the apparent correlation of cardiac 2 Gy volume for overall survival. The same group went further to examine the relative sensitivities of anatomic subsections of the heart. Stam et. al. (2017b) used retrospective anatomic mapping for a group of patients that received

SABR for lung early-stage lung cancer and found that although volume-based dose metrics were not associated with death, doses to the superior vena cava (SVC) and left atrium (LA) were found to correlate with a negative overall survival.

McWilliam et. al. (2017) used a novel method of examining 1100 patients treated with thoracic radiotherapy and grouping patients by survival. By using modern anatomical dose deformation methods, aggregate dose maps were created for each group. The study found that patients in the 'died' group had increased doses to the base of heart that were statistically significant. Although the authors used statistical methods to correct for obvious confounders such as increased stage of disease, the data is retrospective and so should be treated with some caution. It does, however, serve as another hypothesis-generating signal for association between increased cardiac dose and poorer overall survival.

Qian et. al. (2017) also examined the importance of the position of the dose in the heart for higher doses per fraction, demonstrating that sino-atrial (SA) node toxicity was – whilst uncommon – was associated with those patients receiving the highest SA node doses, developing within 6 months of irradiation and requiring pacemaker-correction.

It is possible that dose received by the base of the heart is a predictor of patient outcome in terms of late cardiac morbidity and overall survival. This sub-section of the heart contains the AV node, valves, the SVC, and LA. There are also indications that the SA node and conduction bundle in the intra-ventricular septum along with the LAD

coronary artery on the myocardial surface might also be predictive for cardiac morbidity and/or mortality.

In addition to the potential for toxicity arising from collateral dose to cardiac sub-structures, there is the additional potential for toxicity in the form of radiation-induced lymphocytopenia (or lymphopenia). It is well-established that the threshold lethal dose for lymphocytes is relatively low with LD₅₀ of 2 Gy and LD₉₀ of 3 Gy reported (Venkatesulu et. al., 2018). The high degree of sensitivity of lymphocytes circulating through radiation fields in patients undergoing multi-modality therapy (with chemotherapy or immunotherapy), is such that it can be detrimental to patient outcomes in patients with oesophageal cancers (Wang et. al., 2021). Multi-modality therapy for the treatment of solid tumours proximate to the spleen or vascular structures is usually accompanied by regular biomarker monitoring in the form of lymphocyte count throughout and beyond therapy.

It is acknowledged that cardiac SABR patients are highly unlikely to be receiving concurrent chemo- or immunotherapy which reduces the risk of additional lymphocyte death, however, given the prescription dose of 25 Gy to periphery of the PTV (typical margin 5 mm) in the treatment of cardiac SABR, even in the presence of the highest dose gradients with photon therapy using the highest sophistication image guidance and motion management, the volume of the cardiac chambers (and therefore the blood pool) subject to doses greater than these threshold doses is significant. As such, the examination of dose modelling throughout the cardiac chambers and major vessels is likely to be valuable in validating any potential link between dose and lymphocyte toxicity.

Although to date, authors have largely used retrospective methods to establish correlations between heart dose and overall survival, a mechanistic cause of death has not been established. Furthermore, most authors have examined overall survival including all deaths rather than cardiac-specific death. However, these hypothesis-generating studies have led to the first combination study by Banfill et. al. (2019) who are retrospectively data mining heart sub-structure dose data whilst prospectively collecting biomarkers in patients undergoing curative-intent radiotherapy for lung cancer. The outcome of this study could start to define some dose limits for cardiac structures in the future.

From these data presented, it is clear that there is a rapidly widening interest in the link between cardiac dose and cardiac toxicity based on historical clinical data. Current trials will likely improve the quality of the evidence for causal links between these aspects, but despite currently available data being of low quality, it is prudent to assume that dose to normal cardiac structures should be minimised wherever possible via plan optimisation.

Retrospective analysis of patient outcomes following radiotherapy in the treatment of breast cancer patients allowed for relatively long follow-up and large patient numbers and, as such, it was hypothesis generating which developed the field of research into cardiac toxicity. However, it is acknowledged that its direct relevance to cardiac SABR toxicity is limited, the reasons being two-fold:

- the data is older (Møller et. al. (2008), Darby et. al. (2013) and Carlson et. al. (2021) whose study included patients treated between 1985 and 2008)

which increases the level of uncertainty and complexity of associating cardiac doses with toxicity due to the accuracy of modelled dose to cardiac structures; and

- the total dose delivered to cardiac structures is likely to be significantly lower than that delivered in single fraction SABR, hence is radiobiologically dissimilar);

This compares with the evidence from lung cancer patients where:

- the data is more contemporaneous (Johnson-Hart (2018), Speirs et. al (2017), Stam et. al. (2017a, 2017b), McWilliam et. al. (2017), Qian et. al. (2017), Banfill et. al. (2019)) meaning improved dose modelling accuracy for cardiac structures and the advent of prospective studies; and
 - the total dose delivered to cardiac structures was higher due to the proximity of the clinical target volume to the cardiac structures and due to the higher prescription doses employed in the treatment of lung cancer.
- These both improve the radiobiological relevance for cardiac SABR toxicity.

In summary, although there is demonstrable increasing interest amongst the radiotherapy community in determining associations between delivered cardiac radiation doses and negative cardiac outcomes for early-stage primary lung cancer or breast cancer patients who have a relatively good prognosis, the risk of radiation-

based toxicity in patients with drug-refractory cardiac arrhythmia is viewed quite differently. Cuculich et. al. (2017) acknowledge the very high underlying risk of death and low likelihood of survival free from subsequent episodes of VT for patients with end-stage cardiac disease, especially for those patients with recurrence of VT following catheter ablation. In this sub-group, which is the most common group currently treated with cardiac radioablation, the risk of death is estimated to be between four and six times the risk of patients that do not have recurrent VT following catheter ablation.

As such, the risk-balance for patients with significant life-limiting drug-refractory cardiac arrhythmia is currently deemed sufficient to ethically warrant the treatment of such patients with cardiac radioablation within clinical trial and beyond. Despite this, it is advantageous to use the cardiac toxicity data we have to-date to optimise the measurement of modelled cardiac doses in order to improve the likelihood of establishing association or, indeed, causal links between cardiac radiation dose and toxicity for this cohort.

1.6 The value of quality assurance in radiotherapy

1.6.1 The clinical importance of radiotherapy accuracy

There is a long-held understanding in the radiotherapy community that delivered radiotherapy dose should be within plus/minus 5% of the intended dose (Brahme 1984) to achieve the desired clinical results, at least in the treatment of malignant disease. Mijnheer et. al. (1987) proposed a similar objective of maintaining a combined uncertainty of 3.5% (1 s.d.) as a result of examining dose-effect curves for normal tissues following photon irradiation. These are relatively small magnitudes in terms of whole end-to-end uncertainty budgets when considering the number of interlinked critical dose-determining elements in modern radiotherapy process and the data transmission and interpretation between them, figure 1.2.

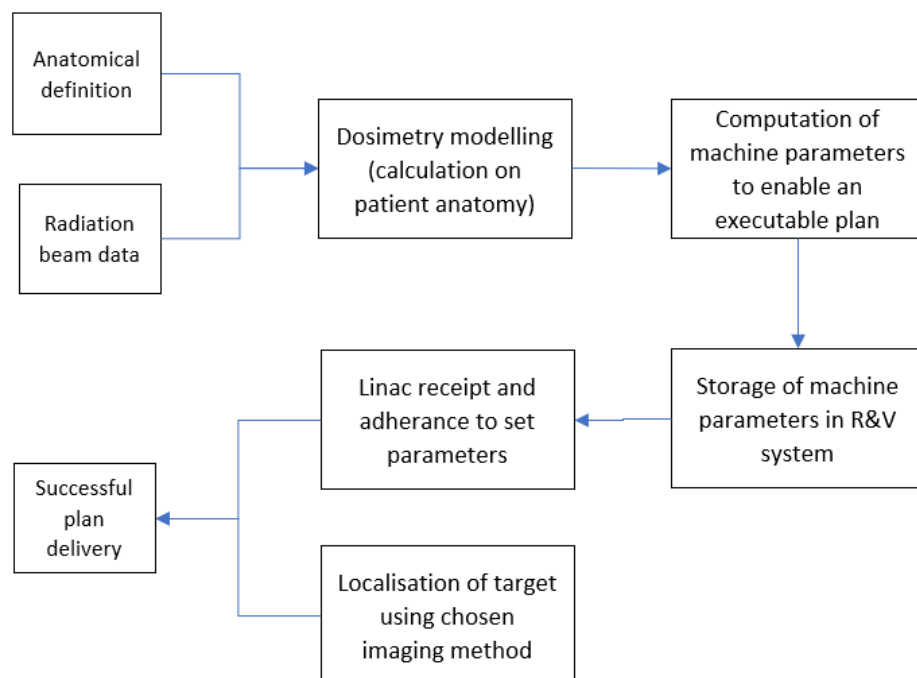


Figure 1.2 Schematic diagram indicating the major elements in the chain in order to accurately deliver a radiotherapy plan

In the era of conformal radiotherapy without image-guidance the number of steps and the complexity of each step was limited which, in turn, limited the indications for radiotherapy due to the reduced dose conformity and the large set up and internal margins required. With the advent of modulated image-guided radiotherapy came the benefits of inverse treatment planning, and when coupled with sophisticated 3D dose calculation algorithms, high-fidelity image-guidance systems and motion management at treatment delivery, all increased treatment delivery complexity and reliance on each element of the chain. However, with this complexity of delivery came increased potential to deliver dose distributions more accurately and with higher dose gradients that, in turn, revealed new frontiers which included SABR.

1.6.2 Quality assurance of radiotherapy delivery accuracy

In acknowledgment of the challenges and importance of maintaining a small uncertainty budget in radiotherapy, dosimetric uncertainty has been the subject of scrutiny from the radiotherapy community since the late 1960s (Shalek 1977).

The first available evidence of measurement of the dose difference between intended dose and delivered dose, termed 'dosimetric audit' (Clark et. al. 2018) was in a postal audit established and managed by the IAEA in 1966 (Izewska and Andreo, 2000) who established a postal dosimetry service for Co-60 radiation beams; this was followed by the MD Anderson / IROC group programme of on-site dosimetry audits established in 1969 (Ibbott, 2010) whose approach was replicated by the European group (EORTC) in 1988, originally for accreditation of radiotherapy within clinical trials.

These early studies were able to determine that the levels of dose uncertainty were concordant with the levels recommended by Brahme and Mijnheer and, as a result, an EORTC workshop in the late 1990s formally recommended that “site visits to all participating institutions [in clinical trials] to carry out dosimetric measurements using the treatment machines” (Johannson, Hanson & Hariot, 1988, p201) along with specific tolerances on the beam output as well as clinical dose distributions in an end-to-end fashion.

Centralised dosimetric audit has grown since the 1990s and is now provided by many institutions around the world: for Europe, EQUAL [the ESTRO (European Society for Radiotherapy and Oncology) Quality Assurance Network for radiotherapy]; for the UK, RTTQA [Radiotherapy Clinical Trials: Quality Assurance Group] which grew out of IPEM inter-departmental audit groups; and for Australia/New Zealand, TROG (Trans-Tasman Radiation Oncology Group). These groups became well placed to provide independent assurance of delivered dose as they became formally associated with the appropriate national standards laboratories for radiation.

Dose modelling or delivery deficiencies are indeed identifiable through dosimetric audit and can have clinical consequences. Ohri et. al. (2013) reported that through meta-analysis that dosimetric deviation from protocol for both targets and organs at risk are a prognostic indicator for overall survival (OS). From the eight studies that met their inclusion criteria across a range of clinical indications, results indicated a significant hazard ratio of (HR) 1.74 (1.28-2.35) in terms of detrimental effects on OS associated with protocol deviation. Although authors rightly acknowledge the limitations of publication bias for potentially unpublished negative results and the

retrospective nature of the study does not prove causation, there is certainly significant association at a magnitude that is typically much greater than HRs found when modifying radiotherapy regimes in clinical trials. The implication then being that if adequate scientific and technical effort is applied to the quality of radiotherapy delivery to minimise protocol deviations, this is likely to be critical in determining accurate answers to primary trial questions by reducing confounding effects from variation in dose delivery accuracy and precision within or between institutions.

Centralised radiotherapy QA including full end-to-end dosimetric audit performed as close to the clinical scenario as possible provides a robust means of independently assessing whole system accuracy and performance and detecting important protocol deviations.

1.6.3 Dosimetric quality assurance measurement methods

1.6.3.1 Point dose measurement

The early examinations of dosimetric accuracy were in the era of conformal radiotherapy with the audits localising using light fields and/or lasers rather than on-treatment imaging. Dosimetric accuracy in this era had a fundamentally low reliance on the collimator / MLC position at the measurement point(s) and, as such, measurements were usually limited to a single dose point as a surrogate measure of dose accuracy throughout the target volume. Over the last two decades, semi-anatomical phantoms have been used for this purpose, examples include the START trial for breast cancer (Venables et. al., 2001, figure 1.3) and the MRC RT01 trial for

prostate cancer (Moore et. al., 2006) where dose was measured using an ionisation chamber in the phantom.



Figure 1.3, Semi-anatomical breast/chest wall phantom used in breast cancer clinical trial quality assurance (Eaton et. al., 2015, reproduced with author's permission)

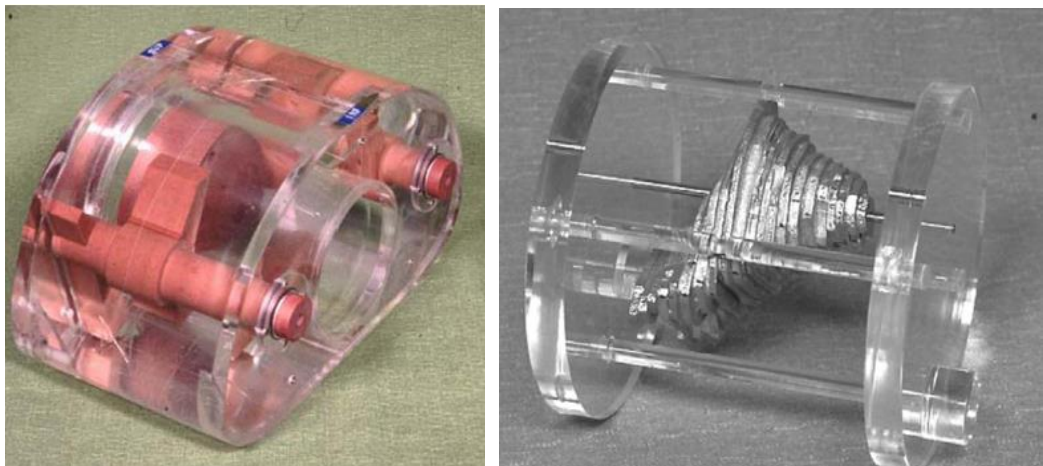


Figure 1.4, Anatomical pelvis phantom used for audit of conformal treatment plans in the (MRC) RT01 clinical trial (Moore et. al., 2006, reproduced with author's permission)

1.6.3.2 Two-dimensional ion chamber or diode arrays

In the era of intensity modulation, accurate dose deposition for highly complex dosimetric shapes relies much more heavily on accurate MLC leaf modelling accuracy, control of MLC position & speed (for dynamic MLC treatments), and control of gantry speed (for dynamic gantry VMAT treatments). Thwaites (2013) found that despite delivery techniques increasing in complexity for intensity modulated radiotherapy, which should have theoretically worsened overall achievable uncertainty levels, in fact, uncertainties remained low in the UK with point dose deviations being $\pm 2.5\%$ (1 s.d.). Hussein et. al. (2012) corroborated this, finding overall cumulative uncertainties achieved being between 1.8% and 3.4% (1 s.d.). These levels of dosimetric accuracy are only possible, however, by “requiring careful consistent attention to quality assurance of every step contributing to final delivered dose to the patient” according to Clark (2015, p1).

More recent multi-centre audits of intensity modulation, including volumetric (VMAT) delivery, have moved away from dose determination at a point given the lack of generalisability of the accuracy to a point for the accuracy of a complex 3D modulated dose distribution and have instead used more sophisticated methods of evaluating doses throughout the treatment volume.

Despite this general move away from point-based measurement, it is worth noting that Gardner et. al. (2012) sought to perform in vivo quality assurance explicitly for cardiac SABR using Accuray CyberKnife. That group implanted multiple thermoluminescent dosimeters (TLDs) and metal oxide semiconductor field effect transistors (MOSFETs) into cardiac tissue of live porcine models. Despite the difficulties

associated with these dosimeters, the authors found delivered dose differences of 5% and 6% compared with calculated doses for the epicardium and the coronary sinus, respectively. This is a good outcome given the associated uncertainties, however, of course these results only provide a series of very low-resolution point dose measurements and would certainly not be ethical or practical in a human cardiac SABR patient population.

To improve the utility of dosimetric quality assurance for modulated distributions, devices that allowed for assessment of a dose plane (two-dimensional assessment) were employed. This methodology was used for two, large, intensity modulated radiotherapy audits (Eaton et. al., 2017, Clark et. al., 2014) with results encouragingly revealing similar dosimetric accuracy to those results found by Thwaites (2013) and Hussein et. al. (2012) with mean differences to calculated dose remarkably close to zero with variation of approximately 2% (1 s.d.).

Unfortunately, the interpretation of both studies for end-to-end dose assessment in clinically meaningful planes were limited because they both employed non-anthropomorphic two-dimensional multi detector phantoms, namely the PTW Octavius and Sun Nuclear Arc Check. These devices effectively measure photon fluence accuracy as a surrogate of dose accuracy. Furthermore, end-to-end system accuracy could not be tested as the anatomical localisation methodology did not reflect the patient scenario due to both devices being non-anthropomorphic in nature.

1.6.3.3 Electronic Portal Imager Dosimetry

Electronic portal imager dosimetry (EPID) is an example of a higher resolution two-dimensional device, but in all applications the application and interpretation is similarly limited to 2D detector arrays they neither are able to provide direct measurement of absorbed dose in an anatomically relevant position or plane and patient-like localisation methods are not employed.

When combined with the patient for use in IVD, it also remains limited in its error specificity because photon fluence has traversed the patient before collection. Modern panel-based IVD systems allow for back projection of photon fluence and secondary dose calculation inside the patient model using pre-treatment imaging or on-treatment imaging, however a dose difference detected when compared with planned dose is difficult to interpret because of the many potential causes of dose difference in that method.

With the use of EPID for IVD with the patient in situ (transmission EPID IVD), differences between planned vs measured dosimetry are dominated by differences in the patient position, or the internal anatomy of the patient, compared with planned. Without the patient in situ (non-transmission EPID IVD), significant errors can still arise from the calibration of the panel due to dependencies on dose-rate, collection frame rate, beam energy, and source/detector geometric coincidence, etc.

Whether the patient is present or not in this method, the EPID IVD method is also unable to provide a direct measurement of absorbed dose at a critical target or organ at risk, instead integrated dose can be calculated in the plane of the panel or

reconstructed dose can be calculated using back projected signal intensity at the panel. Because the panel is also inherently linked both geometrically and temporally (by data collection triggered by the MV pulse) this aspect limits its independence and universality.

At the time of publication of MacDougall et. al. (2017), there was an absence of commercially available fully automated EPID IVD methods. Since that time, some groups have implemented EPID IVD for SABR patients. Esposito et. al. (2021) claim to be the first group to have used this technique in a 3D fashion for abdominal and pelvic SABR; however, they acknowledge the additional uncertainties associated with the detector in terms of frame capture rate, voxel size, calibration curve & dose 3D reconstruction that are all inherent flaws of this method of indirect dose measurement.

The high number of uncertainties associated with EPID IVD mean that even with the use of statistical process control (SPC), the number of investigations in this clinical setting were rather high even employing a generous gamma index (3%/3mm) tolerance of >85% over the region of PTV or 3.5% mean dose change in the PTV (from International Commission on Radiological Units Report 83). The group found that most of the large differences in measured doses were due to residual patient set-up error, immobilisation differences, patient motion and EPID algorithm failure, with 13% remained unresolved thus illustrating the difficulties of error-source identification and interpretation when using an EPID IVD method. A further challenge of EPID IVD is the limitation only to c-arm based linacs, meaning that it is not a device that can be used universally for all systems.

1.6.3.4 Radiochromic Film

The value of radiographic (silver-halide) film has long been recognised for the commissioning of dosimetric parameters of intracranial stereotactic radiotherapy, geometric end-to-end targeting testing, and the determination of clinical distributions (AAPM Report 54 Task Group 42, 1995). This was further demonstrated in its use for the determination of IMRT distributions in the 1990s and 2000s (Low et. al., 1998, Olch, 2002). Despite its practical challenges and limitations in the usable dose range and over-response at depth, its inherent extremely high spatial resolution, lack of angular dependence and ability to integrate dose irrespective of dose rate meant that it quickly became a tool of interest in the assessment of high dose gradients in radiotherapy.

Radiochromic film, however, is a dosimetric medium that relies on polymerisation of radiation-sensitive diacetylene molecules within an active layer between polyester layers. On irradiation, the molecules transform in to a polydiacetylene polymer which is blue in colour with the degree of polymerisation being linked to the magnitude of absorbed dose received by the medium. Because of the mechanism of conversion, this film is advantageous over radiographic film as whilst it maintains very high spatial resolution (more than 1000 line pairs per millimetre are achievable but more commonly 3-6 pixels per millimetre are considered sufficient for radiotherapeutic applications), it obviates the requirements of chemical processing and the handling difficulties around light ambient sensitivity.

Early iterations of radiochromic film such as HS-810 or MD-55, however, had low sensitivity to radiation meaning that doses higher than those intended per clinical

fraction would be required in order to achieve an appreciable film blackening (Soares & Devic, 2009). Modern radiochromic films such as EBT-3 are much more sensitive in the clinical fractional dose range whilst having the additional advantages of having near tissue-equivalence with effective atomic number of approximately 7.5 (Niroomand-Rad et. al., 2020), very low dependence on temperature, ambient light exposure and radiation energy spectra (Rink et. al., 2007). These additional conveniences have made radiochromic film became more desirable as a dosimeter to measure highly modulated distributions such as those employed in stereotactic radiotherapy (Wilcox and Daskalov 2007).

Irrespective of the radiochromic film type chosen, in order to exploit the benefits as a dosimeter, however, there are several technical steps to take in terms of the configuration and corrections for the optical scanner and the determination of an accurate and reproducible relationship between pixel value / film optical density (OD) and absorbed dose which is known as the dose calibration curve.

Most empirical studies have used EBT-2 film given its longer history and these results indicate that in terms of absolute accuracy over a range of dose magnitudes, some authors report accuracy better than 2% (1 s.d.) between 0.2 and 100 Gy, others measuring 1.5% (1 s.d.) up to 50 Gy (Devic, 2011). For the more symmetric EBT-3 film other authors have concluded that absolute dose determination due to curve fitting is better than 1.5% (1 s.d.) when appropriate colour channels are chosen for calibration based on dose magnitude ranges (Sorriaux et. al., 2013). Some authors show improvements in the absolute dose determination using three-channel (64-bit) correction which is less sensitive to non-dose-related changes in OD than single

channel correction (Palmer et. al., 2014, McCaw et. al., 2011), however it is possible to overcome some of the limitations of single-channel scanning using careful calibration and a 'one-scan' process.

The aforementioned properties make radiochromic film a highly advantageous medium for direct measurement of absorbed dose in two dimensions, especially in the presence of high dose gradients (Devic et. al., 2016) in an anatomical plane of interest as corroborated by the most contemporary recommendations from the AAPM Task Group (Niroomand-Rad et. al., 2020). The medium is also very transportable and universal and so make it an attractive option for centralised radiotherapy dosimetric QA when combined with transportable phantoms for the direct measurement of dose between all types of radiotherapy delivery system.

1.6.4 Dosimetric quality assurance for SABR

There have been several dosimetric audits for SABR in recent years (Clark et. al., 2017) and the common thread running through them is the universal use of high-resolution dosimetric measurement accompanied by online imaging-based localisation (IGRT). These themes reflect both the increasing reliance on imaging-to-treatment system coincidence, the increased clinical importance of positional accuracy in the delivered dose for SABR where much higher dose gradients of 10-15% per millimetre are achievable, compared with a more typical 5% per millimetre typically seen in conventionally fractionated radiotherapy.

Such audits include for specific clinical trials such as PACIFIC by MDA/IROC and by The UK SABR Consortium/RTTQA for the NHS SABR Commissioning through Evaluation programme in England (Lee et. al., 2015, Distefano et. al., 2015). The latter audit employed both a point dose measurement using alanine and radiochromic film to determine SABR dose accuracy in anatomical planes of interest in anthropomorphic phantoms. Results revealed comparable results to those seen historically, namely 1.7% (1 s.d.) for point doses, with the mean distance-to-agreement (DTA) between the intended prescription isodose and measured dose being 1.3mm (1 s.d. 2.2mm).

The importance of quality assurance for new treatment modalities or techniques is recognised by bodies such as ESTRO (Clark et. al., 2018) in improving standardisation of practice. Furthermore, the importance of dosimetry, and specifically the effect of optimisation, demonstrated by clinical audit is both recognised by the European Commission Guidelines (European Society of Radiology, 2011) and in the UK in terms of setting, maintaining and improving standards (Clark et. al., 2015). However, the typical time lag between technology-driven or clinically driven-change in radiotherapy practice compared with appropriate technical evaluation is recognised by Torras et. al (2017) who state:

“...the development and implementation of quality control measures have not kept pace with the remarkable technological advances achieved in recent years” p409

This is certainly true in the recent limited use of SABR for cardiac indications as, despite there being unmistakably positive evidence in its early clinical application (section 1.4), there is no evidence seen in the published literature that examines the end-to-end accuracy of cardiac SABR dosimetry; nor is there evidence of quality assurance programmes or guidelines in existence to measure and/or set acceptable or optimal dosimetry for therapeutic cardiac SABR. This situation remains despite some authors having already demonstrated the utility of anthropomorphic 3D printed spine and lung models for substitution into commercially available thoracic phantoms (Tino et. al., 2022). Furthermore, although it is acknowledged that there is a commercially available phantom which allows for dose measurement in a single pre-set plane of the heart (CIRS Dynamic Cardiac phantom <https://www.cirsinc.com/products/radiation-therapy/dynamic-cardiac-phantom><https://www.cirsinc.com/products/radiation-therapy/dynamic-cardiac-phantom/>, last accessed 4 July 2020), there is no evidence of its use to determine dosimetric accuracy for cardiac SABR in the literature. There are many potential reasons for this, but it is likely that this is due to a combination of the relatively recent release of the phantom, the commercial phantom cost, the inability to configure the measurement plane and the lack of multi-centre cardiac SABR clinical trials that require or indeed recommend dosimetric audit as a pre-requisite quality assurance measure.

Despite the lack of evidence available, dosimetric validation is instructive in this setting due of the following reasons:

- the unusual pathological conduction pathway shape and location
circumscribing the myocardium resulting from cardiac aetiology means that

target shapes for cardiac SABR are at the higher end of the complexity spectrum (compared with oligometastatic nodal, lung, liver, metastases for example). This target complexity could increase the levels of dose modulation to produce the complex dose distributions required clinically;

- the technique is very novel and so the long terms effects of delivering large ablative doses to the myocardium are unknown. In order to be able to make meaningful prospective or indeed retrospective analyses of patient outcomes compared with planned dosimetric indices, it is critical to validate the 3D dose modelling such that any calculated doses in the TPS are reliable in order to correlate delivered dose with clinical outcomes;
- the clinical evidence for the technique demands a very high single fraction dose (peripheral dose of approximately 25 Gy with a dose maximum dose of approximately 35 Gy). This is at the very high end of fractional doses used for extracranial SABR, second only to single fraction lung SABR which is also in its infancy in the UK. When coupled with the significantly lower proximate OAR dose tolerances also increases the demand on dose modulation meaning that new class solutions are likely to be required for institutions that are to move from delivering SABR for metastatic indications to delivering cardiac SABR;
- the radiotherapy localisation methods used for cardiac SABR are novel. These are likely to include localising on the soft tissues of the myocardium itself, implanted fiducial markers or ICD electrode tips. To adequately quantify the end-to-end radiotherapy targeting error, the imaging and localisation methods should mirror the clinical situation as closely as possible such that the end-to-end accuracy is as meaningful as possible.

In terms of reflecting the typical clinical situation, there are no clinically available solutions to motion management for cardiac motion such as cardiac triggering or gating. Furthermore, normal cardiac motion arises due to underlying complex conduction pathways (that characterise sinus rhythm) which act to polarise and de-polarise the different sub-structures of the heart in an ordered, systematic manner to maintain efficient blood flow through the cardiovascular system. The motion that results is highly non-rigid due to its high-frequency, relatively small-amplitude torsional forces that act to squeeze blood from atria to ventricles or from the ventricles to the large vessels (Bardinet et. al., 1996).

The primary end point of this research is to evaluate dosimetric delivery accuracy of modelled (calculated) cardiac SABR dose distributions, therefore it is beyond the scope of this research to characterise and simulate the inherent complexities of physiological cardiac motion. Furthermore, there exist physiological differences from patient to patient which include additional complexity of disruption to normal cardiac function as a result of scar tissue formation in the myocardium as a result of prior ablative therapy or due to prior myocardial infarction that can affect myocardial tissue motility. This is in addition to practical constraints of producing a phantom that allows for accurate rigid co-registration with the calculation frame of reference (discussed in sections 2.3.1, 4.1 and 5).

Cardiac motion is characteristically very different to that arising from physiological respiration, which is characterised as being lower frequency, typically higher amplitude motion that is more able to be accurately modelled

by largely independent 1-D rigid motions (Wang, Riederer & Ehman, 1995).

Commercial clinical linear accelerator manufacturers have developed motion management solutions which attempt to at least partially mitigate for the effects of respiratory motion, as such in this research, simulation of simple respiratory motion is designed to reflect the clinical situation for currently available motion management techniques.

1.7 Summary and Research Aims

There is a significant body of evidence detailing the efficacy of using radiation in an ablative fashion to treat both malignant conditions and functional indications intracranially, and that body is expanding rapidly into the extracranial arena with the very recent inclusion of cardiac arrhythmic indications such as VT in the phase I/II setting.

Clinical use of SABR exploits the beneficial elements of modern imaging techniques, sophisticated dose calculation and dose delivery methods to treat patients with both primary and metastatic cancer indications using high fractional doses of radiation. Despite recent increase in clinical research for cardiac radioablation, and despite the historically strong theme of quality assurance that is embedded in radiotherapy, there remains a scarcity of systematic examination of the end-to-end deliverable accuracy of SABR doses to cardiac tissues (Lydiard et. al., 2021). This lag between first clinical treatment and established audit in the exploration of novel radiotherapy indications is

not atypical. For example, although the first primary lung cancer SABR treatments were delivered in 1995 (Blomgren et. al., 1995), it took a further 11 years to identify the need for “scrutiny of site qualifications and quality assurance” [of the technique] (Timmerman et. al., 2006).

The cautionary translationally lessons from the field of interventional catheter ablation indicating that anatomical localisation accuracy needed and full target coverage of arrhythmogenic sources are key predictors of procedural success. In addition, historical radiotherapy data points to potential late cardiac radiation sequelae such as fibrosis and myocardial infarction in addition to more contemporary evidence suggesting increases in non-cancer mortality associated with dose being delivered closer to the heart than planned.

When considering these aspects together in the context of cardiac SABR which aims to deliver a very high dose per fraction to highly complex dosimetric shapes and very proximate organs at risk, it is arguable that there is an urgent need to accelerate implementation of meaningful, robust, universal, quality assurance for cardiac SABR to provide confidence in the technique as it expands, avoiding the significant time lags seen in the past.

This work aims to bridge the current research gap by providing equipment and a technique that can independently verify the dosimetric accuracy of cardiac SABR delivery. This involves producing a robust, vendor-neutral, technique-neutral, quality assurance device that offers a systematic method of examining end-to-end dose delivery accuracy for cardiac SABR. The novel device should be anthropomorphic in

nature, dynamically controllable to simulate physiological respiratory motion, and allow for radiation dose assessment in multiple 2D planes using clinically appropriate methods of imaging and motion compensation (including tracking and gating).

Not only will this bring about local benefit of giving individual radiotherapy providers confidence of their end-to-end dose delivery accuracy to accompany clinical roll-out of this new indication, but it will also provide more wide-reaching advantages of facilitating centralised quality assurance services to measure comparative cardiac SABR accuracy between institutions which then provides an opportunity to establish (and subsequently examine adherence to) minimum quality standards for cardiac SABR. This is useful in reducing confounding variation in clinical trials, but also in decision-making for clinical commissioners as the technique becomes more widely available.

Chapter 2: Methods

2.1 Phantom design & fabrication

2.1.1 Phantom requirements and material selection

In order to produce a device that meets intention of purpose in terms of being a vendor-neutral, technique-neutral device able to systematically examine end-to-end dose delivery accuracy throughout the heart, it should fulfil a number of essential requirements, it should:

- mimic typical cardiac anatomy shape and size;
- allow for dose measurement in multiple positions within the cardiac anatomy that, based on current published evidence, are likely to be dosimetrically most critical for both targets and organs at risk;
- provide sufficient image quality to allow cardiac component identification for treatment planning and localisation for treatment delivery;
- include the wires and electrodes from ICDs and pacemakers in typical positions;
- have sufficient rigidity that the definition of the geometric origin remains consistent from pre-treatment imaging through to treatment delivery;
- be a reasonable analogue of anatomic tissue in terms of MV radiation characteristics of cardiac anatomy;
- be configured to be moved under computer control for simulation of physiological respiratory motion.

In terms of the materials for the composition of the phantom, these would exhibit the following ideal characteristics, they should:

- have identical radiation properties to their anatomical counterparts for photon beams of MV energies. Given the domination of the Compton scatter interaction with free or loosely bound electrons at MV energies, ideally one would select analogues with electron densities as similar as possible to their anatomical counterparts;
- have sufficiently different radiation properties in order to produce adequate contrast at photon beams of kV energies such that the cardiac analogue elements of the phantom are distinguishable on pre-treatment CT imaging and linac on-board cone-beam CT (CBCT) for localisation used for the majority of cardiac SABR.

Given the domination of the photoelectric effect interaction in the kV imaging range ideally materials would be selected that exhibit sufficiently different effective atomic numbers meaning sufficiently different mass energy absorption coefficients in order to demonstrate contrast on a kV tomographic imaging. Although there is the possibility to enhance contrast by using dual energy CT (DECT), this technology is not yet universally available and so it should be optimised for single energy CT (SECT) and CBCT.

In order to actuate motion, a phantom that fulfils this requirement is the CIRS Dynamic Thorax phantom (<https://www.cirsinc.com/products/radiation-therapy/dynamic-thorax-motion-phantom><https://www.cirsinc.com/products/radiation-therapy/dynamic-thorax-motion-phantom/>, last accessed 4 July 2022). It was recognised that this phantom has been available for purchase for a number of years and could be adequately adapted to replace a central anterior mediastinum homogeneous section with a cardiac insert. The final outer shape of the insert would have to be prismoidal in shape in order to allow for motion actuated from the caudal end of the phantom. Various options for the cardiac insert were then discussed and considered with colleagues in the Clinical Physics department at Barts Health NHS Trust in terms of fabrication of a device that could satisfy all the essential requirements of the phantom and materials that are listed above.

A considered option was for a fully 3D printed phantom using printed materials that could provide analogues of the cardiac soft tissues and the blood pool. On exploration of the print materials available, ideal characteristics were not found to be available. All 3D print materials were higher in physical density than their anatomical analogues and so two materials were shortlisted based on their physical density as close as possible to their anatomical counterparts, namely:

Vero White (CA models, <https://www.camodels.co.uk/media/1269/connex-vero-white-plus.pdf>, last accessed 7 September 2021) is a hard material with a polymerised density $1.17\text{-}1.18\text{ gcm}^{-3}$.

Agilus30 Black (Stratasys materials (<https://www.sys-uk.com/wp-content/uploads/2020/06/agilus30-material-data-sheet.pdf>, last accessed 7 September 2021) is a rubber-like material with a polymerised density 1.14-1.15gcm⁻³.

Radiation-specific material quantities such as relative electron densities or effective atomic numbers of these materials were not specified from the manufacturer and so it was necessary to examine these in more detail before making any decisions on materials, especially given the potential for diminished kV imaging contrast given the similarity in physical density. It was also possible to modify the materials by using proportional mixing of the two in order to change the rigidity level and so it was necessary to optimise the various key aspects of kV image contrast, electron density and rigidity for the 3D print materials.

To determine this optimal solution, a test sample was produced in a checkerboard arrangement that contained a range of mixes of Agilus Black with Vero White. Contrast strips of pure Vero White separated the mixes in order to test image contrast and electron density. The test sample was CT scanned in a water bath on a Siemens Somatom CT scanner at 120kV, 450mAs, 3 mm slice thickness. Results are available in section 3.1.1.

Barts Health has a long history of producing tissue mimicking and water-equivalent materials both for commercial sale and for in-house applications and so an alternative that explored the use of these materials was considered. Although the use of tissue mimicking materials would provide a more accurate analogue of the blood-pool, it was clear that the morphological complexity for the cardiac elements required a more

sophisticated solution such as 3D modelling and printing. This led to discussions of a hybrid water-equivalent/3D print model to fulfil the brief.

In order to aid material selection decisions and the viability of a hybrid model, a small test print was produced which consisted of a 3D printed cuboid in Vero White with an open cylindrical well into which water-equivalent material could be poured into it before allowing it to cure. This was CT scanned to determine the kV image contrast level, the relative electron densities, and the degree of any leaking of one material into another (figure 3.2).

Because swift re-design as part of an iterative design process was important, it was acknowledged that it would be advantageous to avoid the complication of adding water-equivalent material to 3D print material if it were possible without compromising phantom imaging contrast.

2.1.2 3D computer modelling

An overview of the 3D modelling process using commercial software 'Mimics' and '3-matic' by Materialise™ (Leuven, Belgium, <https://www.materialise.com/en>, last accessed 15 July 2022) that was followed is illustrated in figure 2.1 with all modelling steps being undertaken by the author.

A patient scan with contrast-enhanced cardiac CT was identified with the assistance of cardiac radiology colleagues, the patient data was fully anonymised and then imported into the Mimics software. IV contrast was necessary to allow for accurate delineation

of the blood pool from the cardiac elements, which was necessary subsequently as these separate elements would be produced using different materials.

Auto-segmentation tools were used, followed by with significant manual corrections in order to delineate (mask) the major cardiac structures. Results can be seen in table 3.3 and figure 3.3.

Ideally the phantom would allow for dosimetric interrogation in all planes, however, given the physical constraints of the phantom and time constraints it was necessary to optimise phantom measurement planes to provide the most meaningful interrogation of dosimetrically important aspects of the dose distribution.

Evidence demonstrates that that ventricular tachycardia (VT) is currently the most common indication for cardiac SABR (section 1.4). The electrical targets for this indication can appear throughout the left ventricle (LV) including the apex (anterior-inferior aspect) which, in many instances, can directly border the stomach, a critical organ at risk with a relatively low dose tolerance in a single fraction compared with the peripheral prescription dose of 25Gy. As such, it was imperative to allow for dose measurement in this plane.

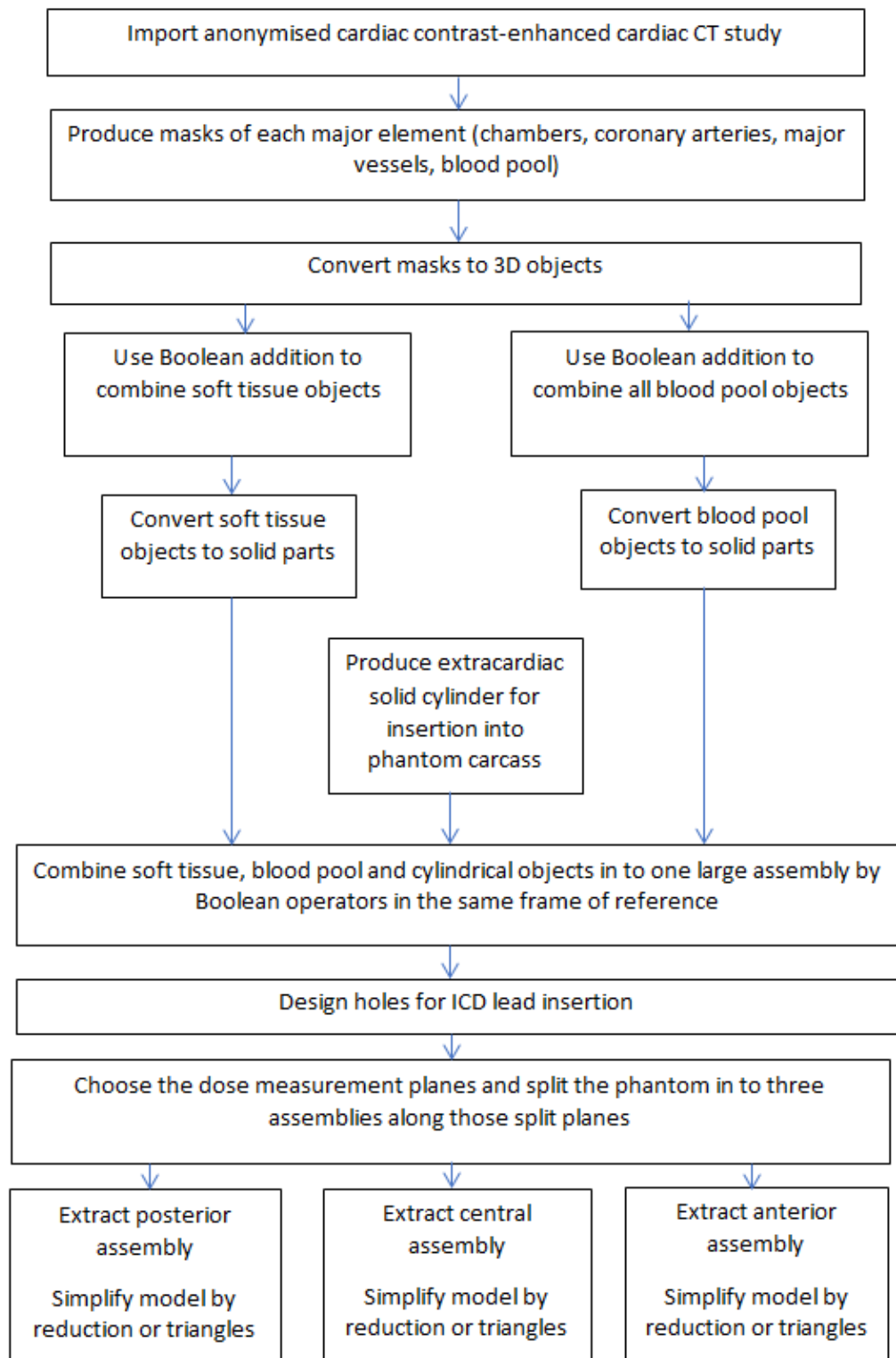


Figure 2.1 3D computer modelling process flowchart to summarise the multi-step process in the production of the cardiac modular insert

Further additional cardiac arrhythmia indications such as atrial fibrillation (AF) and hypertrophic obstructive cardiac myopathy (HOCM) may become clinical priorities in the future. These pathologies originate from targets in the left atrium and inter-ventricular septum and respectively and so were considered as candidate regions for target dosimetric measurement.

In terms of cardiac organs at risk, some cardiac elements have already been identified as potential prognostic markers in section 1.5. These are the sino-atrial node, the atria-ventricular node and more broadly the base (superior aspect) of the heart. By consideration of these anatomical features, two planes were identified for optimal dose measurement. These planes are shown in section 3.1.3.

The three cardiac sections were then surrounded by further solid 3D object using the 3-Matic software to remove any non-anatomical and perturbing air gaps. An outer frame added for each modular part such that the resulting frame around each module encased the cardiac soft tissue, blood pool and extracardiac elements. All three rigid frames when assembled formed a rigid prismoid (cylinder) that could be moved en bloc under computer control.

For the phantom to be versatile across localisation methods, the implantation of ICD electrodes at anatomically appropriate locations was necessary. Typically, electrodes from these devices reside in the LV apex, the LA and the RA with the leads connecting to the ICD / pacemaker following the vasculature however, following anatomical vasculature in the phantom would be both unnecessarily challenging in terms of the design complexity but more importantly detrimental in terms of potential dose

perturbance as the metal leads would traverse the pre-defined measurement planes. Instead, oblique 4 mm diameter cylindrical paths were designed entering deep in to the appropriate phantom myocardium sections from the superior end of the phantom such as they did not obstruct the moving parts nor were they close to the dosimetric planes.

The insert components were scaled to a ratio of 0.75 in all dimensions in order to fit in the downscaled CIRS Dynamic thorax phantom ensuring the cardiac components remained anatomically representative of the size and position of the heart within the mediastinum with respect to the position of the vertebral column, lungs and external surface.

It was necessary to consider a reproducible means of assembly, disassembly, and reassembly of phantom modules without the introduction of unnecessary air gaps or high-density materials that may perturb dose measurement. It was also necessary to be able to identify the film measurement plane origins in the treatment planning system frame of reference for comparison with the planned dosimetry at uncertainty level commensurate with this technique (< 1 mm). To satisfy these specifications, it was specified to the Clinical Physics department to add 3D printed dowels and holes to the four corners of each module in addition to a 1mm deep and 1 mm wide crosshair intrusion into each open plane. This was completed in SolidWorks 2022 (Dassault Systèmes).

The final 3D design of the modular phantom can be seen in figure 3.7.

2.1.3 3D Print prototyping to final phantom production and assembly

3D printed prototypes were printed using a Objet260 Connex3 printer (StrataSys, MN USA) at numerous points in the iterative design process. These were printed to determine the quality of the print compared with specification, paying special attention to the choice of materials. Additionally, the selection of an appropriate material for the extracardiac components for the assembly were also tested including Agilus Black and water-equivalent tissue mimicking material.

Once satisfied with the quality of the print prototypes in terms of the lack of air gaps between materials, material contrast on kV CT imaging and morphological accuracy, the final modular objects were sent to print using the same printer. The modules were finished which included the extraction of 3D print support materials. Three ICD leads were then inserted in to the deep cylindrical holes and glued in place to retain their geometric position.

Colleagues in Clinical Physics then removed a cylindrical prism of existing water equivalent material from the CIRS Dynamic thorax phantom of the same outer dimensions as the 3D printed cardiac phantom insert assembly and re-sited the motion controller from being coaxial with a lung section insert to being coaxial with the cardiac assembly. Finally, the inferior end of the cardiac insert was attached to the existing motion actuator.

Results for the prototypes and the final print appear in section 3.1.3.

2.2 Radiochromic Film Characterisation Methodology

2.2.1 Introduction

Radiochromic film, described in section 1.6.3.4, when combined with an optical scanning method and appropriate calibration is a high-resolution water-equivalent integrating dosimeter that has the ability to measure dose in a two-dimensional fashion directly in the plane of interest. These characteristics make this dosimeter attractive in this application where measurement of dose in multiple dose planes of interest are required. However, because the degree of darkening of the film (optical density) is non-linear with dose and the process of determining the optical density requires an optical scanner, the achievement of accurate and reproducible dosimetric results is dependent on accurate calibration and minimisation (or quantification of) a number of artefacts which may introduce uncertainty. This requires a significant amount of preparation. A recent AAPM report provides recommendations for the use of film dosimetry in TG report 235 (Niroomand-Rad et. al., 2020). According to these recommendations, the dose calibration curve should be pertinent to the batch of film produced and consideration should be given to the dose range for use as this will determine the 16-bit colour channel used for production of the curve and read out of the clinical film as each colour channel examined has an optimal range of sensitivity of optical density as a function of absorbed dose.

The recommendations also encourage determination and minimisation of other sources of uncertainty such as the geometric uncertainty across the scanner bed, correction for Newton-rings (for film versions prior to EBT-3), time-darkening profile and orientation for the effects of light polarisation).

The standard radiochromic film type used at Barts Health is EBT-3 and the scanner type is an Epson Perfection 750 Pro (A4 size scanner) which uses white light LEDs on a moving mechanism with respect to a static film on a glass plate. The scanner offers scanning up to A4 size (210 x 297 mm) at up to 600 dpi in each direction and can be used in both reflection and transmission modes. The software used for scan acquisition was the Epson Scan (v 3.9.3.0EN) and the software used for dose calibration to absorbed dose was the film module within SNC Patient v 8.2 (Sun Nuclear Inc.).

Although there was some experience with the use of EBT film as a solution for the measurement of small volume stereotactic radiotherapy dose distributions for CyberKnife plans, this was only possible for doses up to 10 Gy. Cardiac SABR had additional requirements, namely: the measurement of doses up to 35 Gy using multiple VMAT arcs where the dose cannot be scaled; and the examination of geometrically larger dose volumes including measuring dose to the edge of the film. As such, significantly more characterisation was required to minimise uncertainties in order to ensure that results were reliable.

2.2.2 Scanner configuration

In reflective mode, the incident layer of the film provides a constant reflection of the white light and as the optical density of the film increases with higher dose, there is a higher proportion of reflected signal emanating from the front surface of the film that is non dose dependent. This effect ultimately limits the practical dynamic range of the scanner to 2.5 Gy (red channel) and 8 Gy (green channel) (Niroomand-Rad et. al., 2020)

in reflective mode which is insufficient for the measurement of cardiac SABR dose distributions.

In transmission mode, where the light source and detector are on opposite sides of the film, this reflected-light limitation is removed and therefore the usable dose ranges are significantly increased and beyond the required 35 Gy maximum used for cardiac SABR, notwithstanding the remaining contention over the use of EBT-3 for higher doses (see section 2.2.3).

Reducing variations in the frequency spectrum of the light source and the detection system is also critical to minimising uncertainty. The source in this case is a broad-spectrum white light LED source and to reduce light variation the same scanner with the same warm up procedure was used for all film scanning.

The orientation of the film is critical to the optical density and so the orientation of the film for scanning is consistent throughout due to the alignment direction of the polymers in the film. As a result, a consistent orientation was used throughout the study which is detailed in figure 2.2.

To reduce the potential for additional uncertainty using different batches of film, the same batch of EBT-3 film was used for the entirety of this work (batch lot 03022103, Ashland Inc.).

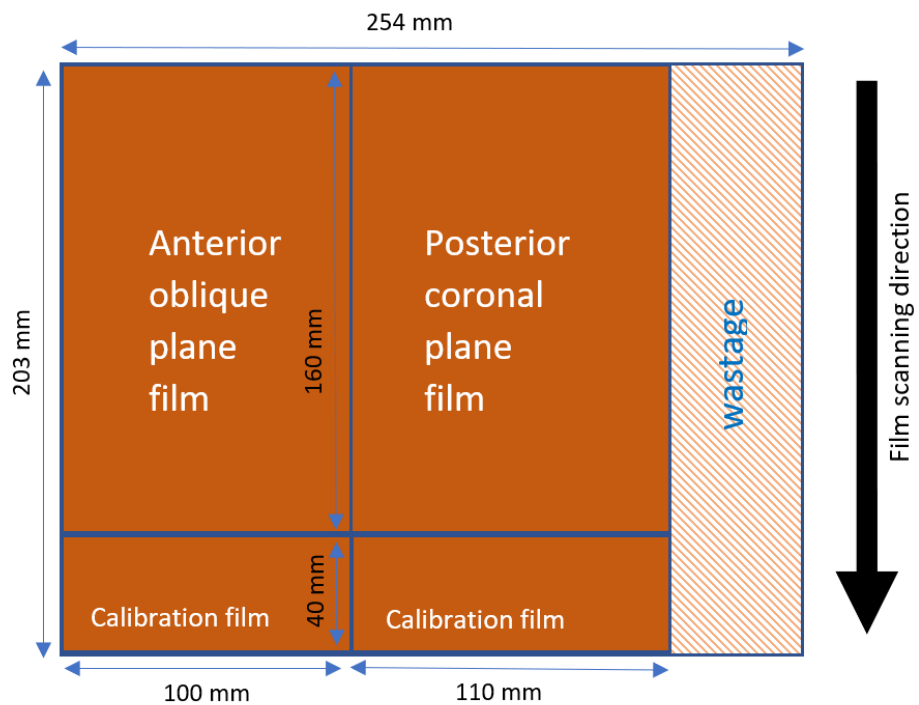


Figure 2.2 Film cutting protocol with respect to film scanning direction. Posterior coronal plane is referred to as the AB plane and the anterior oblique plane film is the BC plane in the results section

2.2.3 Radiochromic film and colour channel selection for dose calibrations

Due to the inherent colour dye present in radiochromic film, the transmissibility of each part of the white light spectrum incident on the film is variable. TG-235 indicates typical pixel values as a function of absorbed dose (figure 2.3).

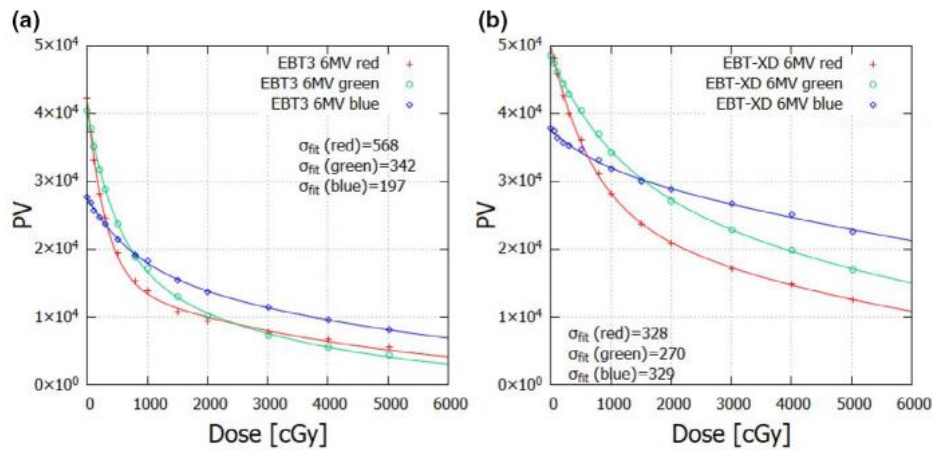


Figure 2.3 Published typical pixel value (PV) to absorbed dose calibration curves, Niroomand-Rad et. al., 2020 (reproduced with author's permission)

By examination of the published calibration curves (figure 2.3) it is evident that the green channel has the highest gradient over the dose range of interest 5-35 Gy. The gradient of the function (first derivative) determines the dosimeter's ability to differentiate differences in dose. A zero first derivative indicates saturation i.e., an inability to differentiate between doses as the optical density is invariant with changes in dose. The larger the first derivative of the function indicates a higher sensitivity of the dosimeter to a change in dose, therefore the green channel is selected for use in this study.

It was noted that the film manufacturer recommends the use of green channel and EBT-XD (extended dose range) for the measurement of doses up to 60 Gy, however its necessity was investigated as part of the film characterisation. The calibration curve from published data for green channel using EBT-XD was plotted, the polynomial fit found, and first derivative calculated. This was then directly compared with batch calibration data for green channel using EBT-3 pertinent to the Barts 6FFF CyberKnife

beam in order to characterise the relative sensitivities of EBT-3 and EBT-XD film over the dose range of interest for this study (see section 3.2.1 and figures 3.13, 3.14).

For each beam quality used, an 8- or 9-point calibration curve was produced for a known dose range of 0 Gy to 35 Gy using a consistent protocol for film cutting and scan orientation. All films used for the batch calibration process were maintained in a dark envelope for a minimum of 24 hours before being optically scanned for dose calibration. This is to remove the high initial temporal optical density dependence that occurs post-exposure which reduces over time which would ultimately propagate through to a large uncertainty in dose determination based on the time to scanning. By increasing the time between exposure and scanning, the dose uncertainty is reduced markedly.

Each calibration was verified for accuracy by re-importing the scanned calibration image (.tif) files using the calibration file of interest and comparing the measured dose with the expected dose in terms of absolute dose deviation from the model curve. Determination of the standard deviation of absolute dose difference across the calibrated dose range was used to inform an estimate of dosimetric uncertainty from the batch calibration process itself.

An estimation of this uncertainty was important as the radiochromic film was acting as the single absolute dosimeter in this work.

Calibration films irradiated to a known dose in the same session as irradiated phantom planned dose films are used in a 'one-scan' method with monitor units (MU) required

for the known-dose calibration films being determined from single field calculation from the treatment planning system and standard departmental beam data from linear accelerator commissioning. The calibration film doses would be used as a calibration check and to scale the clinical phantom film doses if necessary due to post-exposure differential film darkening.

2.2.4 Geometric distortion artefacts

Lateral geometric distortion artefact arises from differences in the light scatter conditions in the axis perpendicular to the direction of scanner motion and is documented to be scanner dependent. TG-235 (Niroumand et. al., 2020) describes this effect as being dependent on the magnitude of optical density for the film and the lateral position with respect to the centre of the scanner. For EBT-3 film scanned with the Epson 10000X (A3) film scanner, this effect has been found to be highly dose-dependent and significantly higher for EBT-3 compared with EBT-XD with dose discrepancies at 50mm from centre of the scanner measured at 9.1% and 11.3% for 10 Gy and 30 Gy respectively (Grams et. al., 2015).

Due to the reported potential significance of this artefact for EBT-3 film and scanner dependency, it was necessary to measure this effect for the equipment prior to use in this study. The Eclipse treatment planning system (v15.6) using the commissioned AAA calculation algorithm was used to create a treatment plan that would minimise the dose gradient perpendicular to the beam central axis. This plan used a flattened 6MV

beam measured at 100 cm SSD, 20cm depth in water equivalent material for a large (30cm x 30cm), figure 2.4.

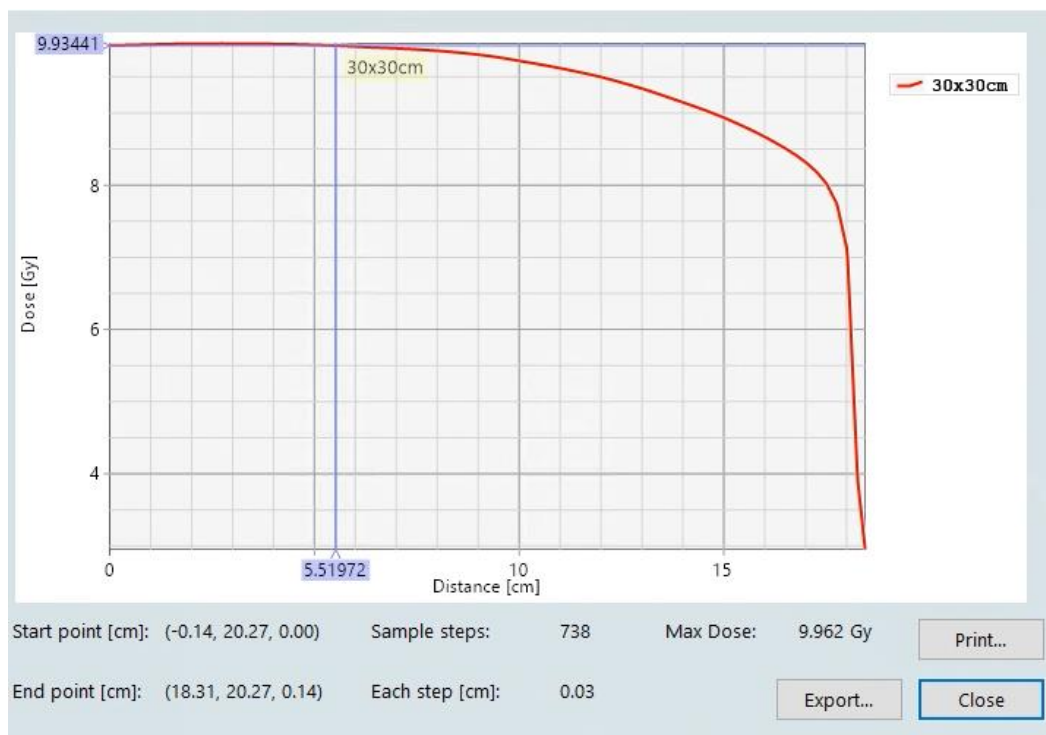


Figure 2.4 Planned dose for lateral artefact testing indicating the method for producing a homogenous dose profile in the plane of interest

Using this method, the planned dose deviation in water was <0.3% within ± 55 mm of the central axis which reflected the maximum width of the film used in this work. The planned dose flatness was sufficient to detect any significant lateral distortions evidenced in the literature that would be to the detriment of the outcomes of this study.

Two EBT-3 films cut to the maximum width of the cardiac phantom film planes, namely 110 mm width x 160 mm in length, were aligned to the central axis of the treatment field at 20cm deep in water equivalent material at 100 cm SSD in full scatter conditions. Each film was then exposed to a dose of 10 Gy and 30 Gy, respectively.

In order to minimise the potential high-magnitude artefact arising from a variable distance between the light source and the film, reported to be of the order 1.2% per mm of distance (Niroomand et. al., 2020), the homogeneity films were scanned using a transparent Perspex sheet of 2 mm thickness was produced to the size of the scanner glass and laid over the film. The Perspex sheet reduced the variable distance from 3 mm to 0 mm. The resulting film was scanned to characterise the geometric artefacts for this measurement dose range and film size and position on the scanner.

2.2.5 Film post-processing

Each film irradiated in the cardiac SABR phantom as part of this study was stored in a dark envelope for a minimum of 24 hours (the elapsed time for production of the batch dose calibration curve) then scanned and converted to dose using the appropriate dose calibration curve. It was then co-registered with the pertinent planned dose plane origin from the treatment planning system using the origin position marked on the films.

A 'one-scan' protocol was employed meaning that calibration films of known doses were scanned concurrently with the phantom film. These were used to identify any artefactual absolute dose discrepancy as a result of differences in time between irradiation and scanning. This is known as the differential blackening correction and exists because of practicalities in scanning films in normal weekday hours.

Linac output was measured in each delivery session using a calibrated field instrument and this variation was also accounted for by correcting the phantom film dose

distribution to that delivered for 1cGy/MU in order to allow direct comparison with the TPS. The integrated factor used to scale every pixel in the phantom films was the product of the blackening correction and the linac daily output factor.

Because the one-scan film process meant that calibration film data were present on each film scanned data, the film file was then edited (cropped) to remove any phantom film-edge artefact, alignment marks and calibration film dose data.

These post-processing methods employed meant that all significant measurable artefacts were considered, leaving a file that contains only dose information that is pertinent to the targets and organs at risk assuming 1 cGy/MU under standard reference conditions with minimised artefacts and aligned to the reference plane origin for direct comparison with TPS calculated data.

2.2.6 Radiochromic Film Summary and Calibration

Although radiochromic film facilitates processor-free high resolution two-dimensional direct dose measurement in planes of interest in an anthropomorphic phantom, it is acknowledged that there are several challenges of using this radiation dosimeter.

These challenges arise from the inherent difficulty in manufacturing of an artefact-free film combined with the inherent uncertainties in using another device to interrogate the optical density of the irradiated film, combined with the inherent uncertainties in converting optical density to reliable radiation dose via calibration. In order to use radiochromic film in a meaningful way to assess radiation dose, the sources of uncertainty – which have the potential to confound results and diminish the scientific

validity – must be minimised / mitigated as far as possible and characterised wherever possible. The following aspects have been addressed:

- The film, use of:

- a single batch (lot) of film;
- independent batch dose calibrations for each beam quality;
- a consistent film cutting protocol to maintain a known film orientation.

- The read-out system, use of:

- the same scanner in transmission mode using the same colour channel;
- consistent film orientation and positioning on the scanner glass;
- a Perspex plate to minimise the distance between film and light source;
- the central scanner region to minimise lateral geometric distortion;
- a consistent scanning protocol in terms of a minimum time since irradiation, that is reflective of the exposure-to-scan time used for batch calibration;
- calibration films scanned concurrently with the phantom films.

- Post-processing, use of:

- a 'one-scan' protocol to check and correct phantom film dose magnitudes for film blackening and daily linac output variations;
- a consistent post-processing method to systematically remove film-edge artefacts and artefacts from calibration films;

- a consistent technique to extract the reference dose planes from the TPS and use of the same determination of the frame of reference origin.

Although most recommendations are followed, where experimental characterisation found tolerable levels of uncertainty for the proposed use of EBT-3 film with single (green) channel dosimetry (sections 3.2.1, 3.2.2), these aspects were reasonably employed for this study.

With the above mitigations in place, the dominant sources of uncertainty arising from batch calibration, geometric distortion and film reproducibility sources are evaluated in sections 3.2.1 to 3.2.3. Each are characterised in terms of their independent magnitude and then used to formulate a combined overall uncertainty in section 3.2.4.

With overall uncertainty measured or estimated and taking in to account the number of mitigating actions above to minimise these uncertainties, it would be unnecessary (and impractical) to repeat each treatment plan measurement multiple times. Instead, the treatment plan verification results are set in context of the overall measurement uncertainty. This is validated by repeating only one treatment plan measurement in an end-to-end fashion to illustrate that overall measurement uncertainty has been adequately estimated and so justifying single measurements as an appropriate approach in this study. This is discussed in detail in sections 4.3 and 4.4.

2.3 Treatment planning

2.3.1 Imaging for treatment planning

The modular cardiac insert was fitted with cut EBT-3 film from the calibrated batch in the two dosimetric planes of measurement and then reassembled in the thorax phantom. The cardiac insert was then attached to the motion actuator. The whole phantom was positioned centrally within the bore of a Siemens Somatom Confidence CT scanner, aligned to external marks.

The field of view was optimised to contain the phantom in the axial plane and the scan length was extended to cover the length of the phantom in the craniocaudal direction. The slice thickness was set to 1 mm with a tube rotation time of 0.5 s, pitch of 1.2. This resulted in the reconstructed image resolution being approximately 0.8 mm in the axial plane and exactly 1.0 mm in the craniocaudal direction.

The tube voltage was maintained at 120kV to ensure that the correct conversion of Hounsfield Units (HU) to relative electron density was performed in both treatment planning systems.

For static treatment plans image acquisition, the phantom was scanned without motion applied to the cardiac insert. This technique was also used for the measurement of CyberKnife respiratory-tracked treatments to reflect clinical practice as patients would be scanned in respiratory expiration breath-hold for this technique. The tube exposure current and time were increased compared with the SABR thorax clinical CT protocol. In the patient cohort, patient-specific exposure modulation is used (*Care Dose* in Siemens terminology), however for the phantom this was increased to

110 mAs per rotation to account for the reduced contrast in the phantom without introducing any detriment to dose calculation accuracy.

For the Varian gated treatment image acquisition, the phantom motion was configured using the CIRS Motion Control v1.1.2 software accompanying the CIRS dynamic thorax phantom product. A periodic pattern was selected such that a systematic comparison across treatment delivery techniques was possible. To most closely reflect the largest element of motion, namely the craniocaudal respiratory motion (Wang, Riederer & Ehman, 1995) a model was selected that acknowledged that patients spend relatively more time at the end of the expiratory phase than the inspiratory phase in tidal breathing (Wang, Riederer & Ehman 1995), figure 2.5.

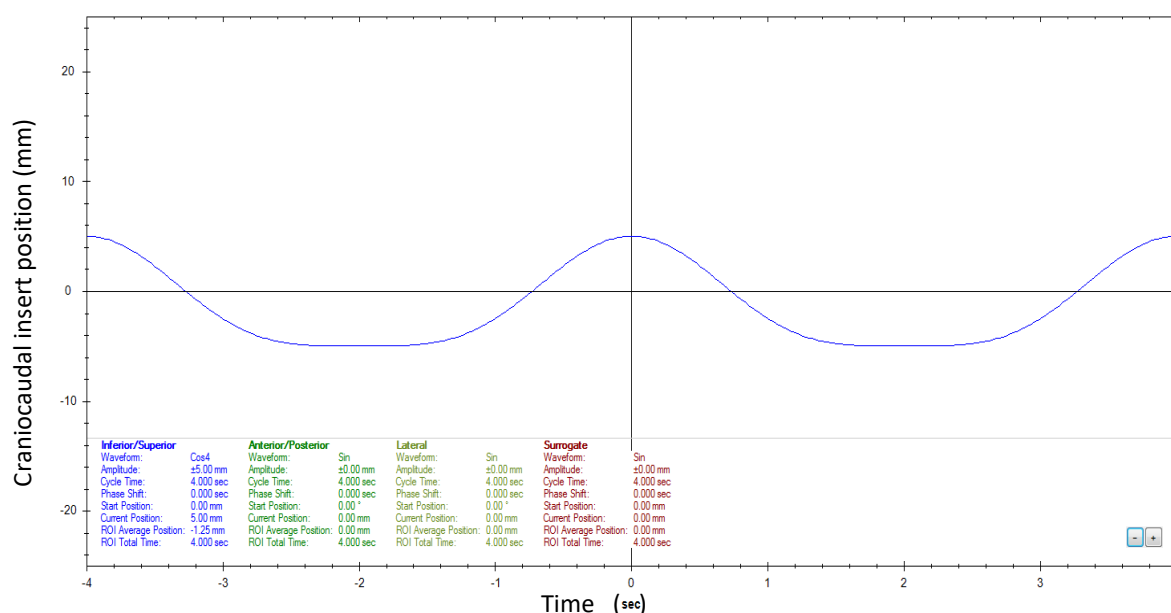


Figure 2.5 Waveform used for respiratory motion modelling, reflecting a longer period spent in end respiratory expire than in inspire phase

The amplitude of the modelled respiratory motion selected was 10 mm (peak-to-trough) in the craniocaudal direction based on the findings of Sceheter, Resar & McVeigh (2006) and Wang, Riederer & Ehman (1995). Although the two studies found slight differences in their cohorts, 10 mm is close to the mean of the craniocaudal respiratory motions found in the groups. Furthermore, larger respiratory motion should be reduced by motion management techniques such as abdominal compression or active breathing control, in line with the current UK guidelines (UK SABR Consortium Guidelines v 6.1, 2019). This magnitude was hence reflective of the clinical setting but also deemed significantly large enough to visualise any geometric delivery errors arising from inadequate primary localisation or delivery using the dynamic delivery techniques.

The breathing time period was chosen as 4 seconds (equating to a rate of 15 breaths per minute) as a relevant analogue of patient motion. The surrogate (external chest) motion was chosen to match the target motion, namely a peak to trough amplitude of 10 mm with a time period of 4 seconds. There was no applied offset between the phases of the motions meaning that as the phantom 'chest' would rise (corresponding to lung inflation under inspiration), the target would move towards the caudal end of the phantom (corresponding to heart motion under inspiration).

The detector block for RGSC (Varian medical systems) was placed on the surrogate motion platform and the phantom motion was initiated. The phantom was then prepared for CT scanning under the 4DCT retrospective data acquisition protocol.

Additional high frequency, low amplitude cardiac motion was specifically not included as it was out of scope for this study given the current sparsity of cardiac data in this area and the current inability of linear accelerators to account for cardiac motion.

The CT scanner used the detected time period of motion from the surrogate RGSC motion to automatically set couch pitch to ensure adequate data acquisition. The 4DCT data is segmented in to ten phases of motion, based on the amplitude of the motion. Both the 3D and 4D CT scans were then both exported to the Varian Eclipse treatment planning system.

2.3.2 Contouring of targets and organs at risk for treatment planning

Using the 3DCT and the initial segmentation used for the 3D computer modelling as a guide, the main cardiac elements namely its four chambers, major vessels, coronary arteries, ICD electrode tips, spinal canal, lungs, etc. were delineated on the CT imaging study (figure 2.6). Image manipulation was used in the Varian Contouring software to rotate the imaging planes away from the standard anatomical planes (axial, coronal, sagittal) into cardiac planes to optimise the visualisation of the separate chambers of the heart as would be performed in the clinical cardiac SABR delineation to optimise the accuracy of the structures. Where relevant, a margin was added to the organs at risk to form a PRV.

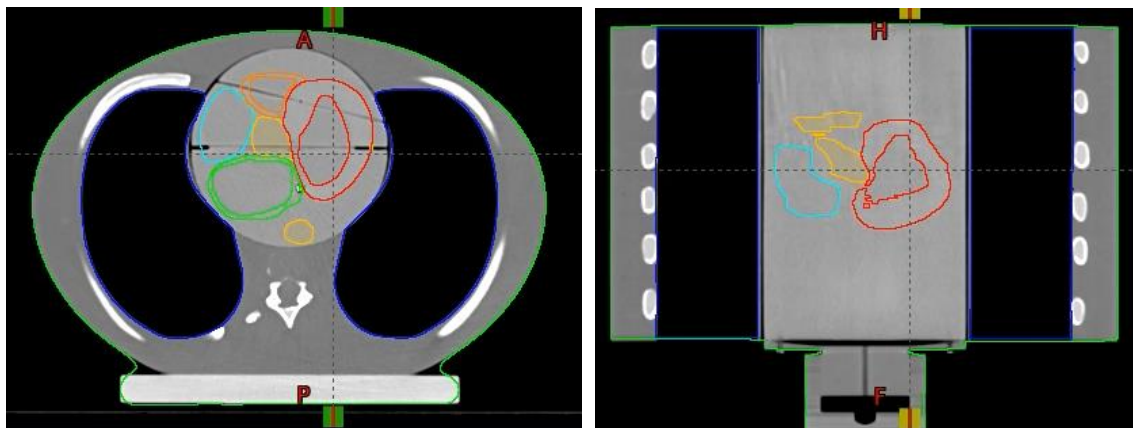


Figure 2.6 CT-based contouring of normal tissues on phantom cardiac insert, A axial cross-section; B coronal. Red left ventricle, green left atrium, dark orange right ventricle, light orange aorta, cyan right atrium

Four clinically relevant targets were then added to the study, namely three that mimic ventricular tachycardia (VT) arrhythmogenic sources (GTV 1 - 3) and one that mimics an obstructive myocardial target as a result of hypertrophic obstructive cardiac myopathy (GTV 4). The VT target shapes were based on anonymised clinical patient VT targets kindly supplied by two UK radiotherapy departments familiar with clinical cardiac SABR. HOCM target shapes and positions were based on advice from cardiology colleagues at Barts Health NHS Trust.

Given cardiac motion was not incorporated into this study, all GTVs were then grown by a universal isotropic 5 mm margin to PTVs, consistent with current UK clinical protocol and that used in the seminal clinical trial (Cuculich et. al., 2017). It was intentional to not add an additional margin to form an respiratory ITV in order to investigate whether that was needed to account for dosimetric blur for the dynamic delivery techniques, compared with their static counterparts.

Example VT and HOCM targets are illustrated in figure 2.7.

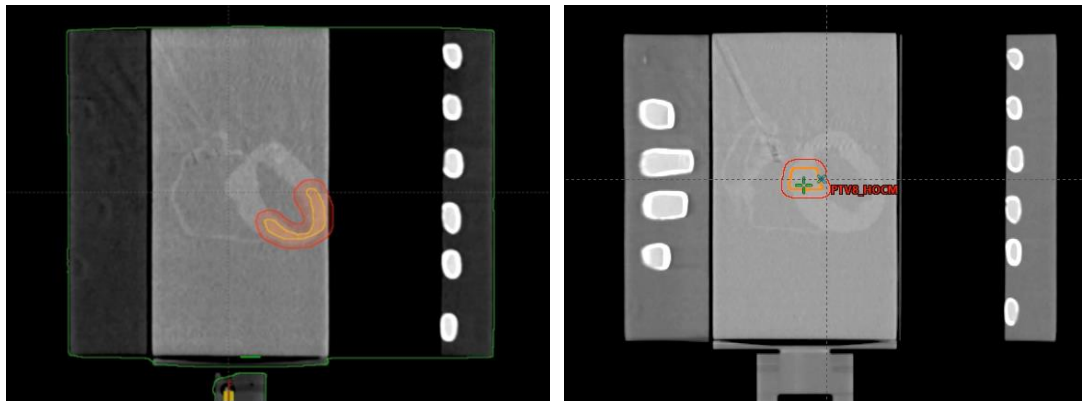


Figure 2.7 Example targets used in this work, coronal or oblique-coronal sections left: GTV 1 and PTV 1 (VT); right: GTV 4 and PTV 4 (HOCM)

All PTVs were visually inspected to ensure that each traversed at least one of the phantom measurement planes. All contouring of targets, organs at risk and PRV/PTV margins was completed in the Varian Eclipse TPS to ensure consistency of contour between the two treatment planning systems. Once contouring was completed, the 3D CT and structures were exported to the CyberKnife Precision TPS for treatment planning.

2.3.3 Treatment planning objectives and evaluation metrics

For this research to be to be relevant and meaningful in the clinical setting, it was imperative that treatment plans reflected the prescription dose and high levels of dosimetric complexity of this technique; namely ensuring high levels of prescription dose conformity and minimising intermediate dose spillage while respecting dose limits.

Although this clinical technique is in its relative infancy, there does exist clinical consensus produced by clinical oncologists in the UK in terms of prescription dose,

maximum dose and organ at risk dose tolerance. Of course, this is an evolving landscape and so, as the evidence builds, we might expect these data to change but the dosimetric parameters employed in this study were consistently throughout this study.

The prescription dose used in the UK for these indications is 25 Gy in a single fraction. This dose should be prescribed as the conforming dose to the PTV surface and should cover at least 95% of the PTV (i.e., $PTV_{25\text{ Gy}} \geq 95\%$). The maximum point dose within that volume is set pragmatically at 35 Gy, meaning a minimum effective prescription isodose of 71.4 %.

Prescription dose spillage is defined as the ratio of the volume of the patient receiving prescription dose : the volume of the PTV receiving prescription dose (Lee et. al., 2019). The ideal value is unity, however in practice the achievable values are complexity- and volume-dependent. Planning objectives for this metric based on published data are listed in the results table.

Modified gradient index is the ratio of the volume of patient receiving half of prescription dose : the volume of the PTV receiving prescription dose (Lee et. al., 2019). The objective for treatment planning is as low as possible, but achievable values are complexity- and volume-dependent. Planning objectives for this metric based on published data are listed in the results table.

Some additional structures were employed to aid in treatment planning to minimise the dose to specific elements of the heart (namely heart minus PTV and left ventricle

minus PTV), these were used as 'optimal' structures for the purposes of treatment planning.

The cardiac organ at risk doses used for this research originate from consolidation of those tolerance dose values kindly provided by Newcastle, Middlesbrough and Sheffield radiotherapy physics departments who all currently have clinical cardiac SABR programmes in place (figure 2.8). Non-cardiac organ at risk tolerances were taken from the UK Royal College of Radiology COVID consensus position (Favre-Finn et. al., 2020).

Cardiac SABR Constraints^Σ (where an OAR is not listed below, refer to general constrains above):

	Tolerance type	Threshold Volume (cc)	Tolerance Dose (Gy)	
			ONE FRACTION	
			Optimal	Mandatory
Heart minus PTV	S	0.035 14	22 16	- -
LV myocardium minus PTV	S	mean	0.027 x (LV volume minus PTV)	
Right ventricle	S	median	11	-
Great vessels	S	0.035 10	- -	37 31
Coronary Arteries	S	0.010	15	18.6
Valves	S	0.010	16	-
Pacing wire tips	n/a	0.010	6	12
ICD can	S	0.010	-	0.5
Oesophagus	S	0.035 5	- -	15.4 11.9
Stomach	S	0.035 5	- -	22 17.4
Duodenum	S	0.035 5 10	- - -	12.4 11.2 9
Small bowel	S	0.035 5	- -	15.4 11.9
Large bowel	S	0.035 20	- -	18.4 14.3

Figure 2.8 Organ (and device) at risk dose tolerances used in this study

Where necessary to meet a mandatory organ at risk constraint, the target dose coverage was compromised to meet that constraint. Where a constraint is optimal, dose was minimised to the organ at risk as much as possible but without reducing target prescription dose coverage to less than 95%. The lower doses to the superficial

elements of the cardiac phantom were minimised as far as possible as reflective of clinical practice.

2.3.4 Accuray CyberKnife treatment planning

The 3D CT data and the structures were imported in to Accuray Precision (v13.3) for treatment planning with the CyberKnife VSI treatment delivery system.

Although some learning from cancer indications treatment planning class solutions can be applied to cardiac SABR, there are differences due to the much higher dose per fraction and additional cardiac-specific organs at risk and their proximity to the target.

Planning structures were used to control beam entry such that beams did not intersect the phantom external surface within 2 cm of the cranial and caudal ends of the phantom. This was to mitigate against large changes in radiological path length in the presence of dynamic treatment between treatment planning and delivered dose. One or two circular collimators were used to produce an acceptable plan.

Where necessary, optimisation target structures were produced from the PTVs. These structures were used in the optimisation process to remove potential conflict for the objective function. All plans were inverse planned using the VOLO optimiser with the PTV (or optimisation PTV) minimum objective having the highest weighting (objective function penalty) value. PRV maxima or optimisation structures outlined in section 2.3.2 were used to control the doses to organs at risk, usually with a weighting less than or equal to the PTV.

Finally, four ‘shells’ were used to control prescription dose and intermediate dose levels in order to improve prescription dose conformity, modified gradient index and some lower doses as far as practicable without having a detrimental impact on the prescription dose coverage, specific organ at risk doses or fractional treatment time.

For both the static and dynamic scenarios, the ‘Synchrony’ respiratory modelling option was selected in the treatment planning system which reflects clinical practice as this can be subsequently disabled if it is found that no motion management is required.

Each plan was normalised to maintain a balance of PTV prescription dose coverage, specified dose maximum, organ at risk dose tolerances and treatment time. Where it was not possible to achieve $PTV_{25\text{ Gy}} \geq 95\%$ due to proximate organs at risk, the PTV was compromised by the minimum possible amount in order to achieve the dose tolerance to the organ at risk. All plans were checked for adherence to the OAR dose tolerances. The RayTracing dose calculation algorithm was used as the final dose calculation for all plans with a calculation resolution set to the native resolution of the CT imaging, approximately 0.8 mm x 0.8mm x 1.0 mm in the left-right, anterior-posterior, cranio-caudal directions (respectively).

For localisation, the distal end of each ICD electrode was identified using all three imaging planes of the CT, windowed suitably minimising photon starvation artefact and therefore minimising positional uncertainty. This reflects the clinical localisation method for CyberKnife delivery as only 2D kV stereoscopic imaging is available for CyberKnife at the present time and is used for the clinical and pre-clinical treatment with cardiac SABR (Gardner et. al., 2012, Bonomo et. al., 2015, Loo et. al., 2015).

Following the clinical workflow for SABR treatment with fiducial tracking, an additional set up (QA) plan was created using the spine tracking localisation method. This is to account for any rotations of the phantom compared with the reference plan geometry that would not necessarily be detected using localisation of the ICD electrodes alone using stereoscopic imaging.

Once finalised, the plans were made deliverable in and the 3D DICOM dose object was exported to SNC Patient (Sun Nuclear Corporation) for subsequent analysis.

2.3.5 Varian VMAT treatment planning

For the static Varian treatment plans, the same static 3D imaging of the phantom was used as the reference CT accompanied by similar treatment planning techniques for optimisation structures as per CyberKnife treatment planning to mitigate against optimisation objective conflicts.

A previous class solution existed for delivering up to 8 Gy per fraction using VMAT which employed one or two 360-degree VMAT arcs with a Millennium 120 MLC. The collimator was set to a non-cardinal angle to minimise (blur) the effects of inter-leaf leakage and a complementary collimator angle selected if a second arc was employed.

Given the minimal experience at this institution for VMAT plan production for a dose magnitude and complexity for this indication, a range of class solutions were initially investigated for this indication including multiple non-coplanar partial arc VMAT approach (using non-zero couch angles) to reduce the modified gradient index.

However, the dosimetrically small advantage of this was not found to be beneficial

enough to outweigh the challenges arising from couch collision and limited imaging abilities arising from non-zero couch angles. Ultimately, a 4 x 360-degree coplanar arc VMAT class solution was arrived at for all treatment plans which closely reflects the UK clinical experience for delivery of cardiac SABR to date (Lee et. al., 2021).

Although the UK and US experience is dominated by employment of flattening-filer-free (FFF) beam qualities because of the improved dose rate, some institutions still use a flattened beam. At the outset of this research, only the flattened beam at 6MV was fully commissioned for VMAT delivery in this institution and so this beam quality was used initially for the examination of static delivery plans. However, in the course of this work FFF was commissioned for use and so the work was repeated with this modality given the high utility in its reduction of treatment times, especially for gated treatments.

Each plan was optimised using the Varian Eclipse photon optimiser (v. 15.6.06) with appropriate weightings used in the optimiser for the target volumes, organs at risk and optimisation structures. The Normal Tissue Optimiser (NTO) was used in all plans to reduce dose further to the remainder of the patient.

Each plan was normalised in the same way as the CyberKnife plans and checked for adherence to the OAR dose tolerances. The AAA (v15.6.06) dose calculation algorithm was used for all plans using a 1 mm isotropic dose calculation grid.

For localisation, an additional imaging (QA) field was added to use as a 3D kV CBCT image. Once finalised the plan was made planning approved and the DICOM dose object was exported to SNC Patient for subsequent analysis.

For the planning and dynamic delivery of the VMAT plans, it was apparent that using a full ITV technique to account for the full range of respiratory motion would not be dosimetrically optimal as most of the treatment plans were already at OAR tolerance balance point and so this would be dosimetrically inferior. Furthermore, although it is apparent that most of the evidence in the literature from clinical treatment employs the full ITV technique (Cuculich et. al., 2017, Lee et. al., 2021), it was identified that it would be of higher benefit to investigate delivery accuracy using the Varian gating capability, which has the potential to significantly minimise treated volume. Finally, as experience grows in this novel field and this indication becomes further established, it is likely that the use of respiratory gating will increase (as is seen for the treatment of lung cancer), hence it was deemed a pertinent time to examine this.

In the gated scenario, the photon beam is only delivered during a proportion of the breathing pattern, this proportion being known as the 'duty cycle,' which ultimately determines the fractional treatment delivery time. The 6FFF beam quality was investigated because of its more practical maximum dose rate of 1400 MU/minute in this high dose setting. Static plans were planned with 6FFF and jaw tracking to act as a baseline for plan deliverability, before being re-planned for the 6FFF gated technique.

For gated delivery, it was imperative to use an appropriately temporally binned reference CT phase, firstly because the origins of the film planes are only determinable when fixed in time, otherwise the dose plane origins would have been blurred due to motion; secondly the choice of the reference breathing phase is fundamental otherwise there would likely be the introduction of a systematic offset due to the dose

calculation being performed on a non-representative phase compared with treatment delivery.

On examination of the acquired 4DCT data, it was apparent that the phantom position was most stable at the expiration part of the cycle, which was expected given the applied motion settings (figure 2.5). By examination of the imaged motion from the 4DCT study, a 4DCT reference phase was chosen near end expiration to minimise motion whilst maximising duty cycle. This was co-registered with the 3DCT scan in order to propagate the structures produced on the 3DCT image to the 4DCT phase for treatment planning. The optimisation process was then repeated for the gated plan and given that there was no change in the size or shape of any of the volumes, the difficulty of the optimisation problem on the gated CT image remained the same, hence it was expected that the final plan metrics remained very similar to the static planning cases despite a new optimisation. Final calculation of the dynamic gated plans reflected that of the static Varian plans.

For localisation, a QA field was added which would subsequently be allocated as a gated kV 3D CBCT image. Once finalised, the dynamic plans were set to allow gating in the plan properties and made planning approved in Eclipse. 3D DICOM dose objects were exported to SNC Patient for subsequent analysis.

2.4 Treatment delivery

For each plan delivered, EBT-3 film was cut to size and taped to the phantom in the appropriate planes with the plane origin from the phantom notches transferred to the film using a fine film pen. Only the cranial, caudal and 'patient' right plane origin locations were marked on to the film as the left of the phantom was very close to the target structures and so would likely introduce an uncorrectable dosimetric artefact on the film. The orientation of the film with respect to the phantom was also marked on the film.

The same Varian Truebeam and CyberKnife VSI linacs were used for all plan deliveries. In each plan delivery session, the daily linac output was measured using appropriately calibrated tertiary (field) ionisation chambers and electrometers. With the knowledge of the daily linac output, a fixed number of monitor units (corrected for daily output variation) were delivered to the calibration check films in order to deliver 15 Gy and 25 Gy using fixed fields of 3 cm diameter circle (CyberKnife) or a 3 cm square field (Truebeam) in solid water-equivalent material at known depths and SSD for each linac.

2.4.1 Accuray CyberKnife treatment delivery

The phantom with loaded film was then set on the couch and the central phantom external marks aligned with the room lasers with a small anterior-posterior offset such that the lasers intersected the spinal section of the phantom for the spinal alignment.

The alignment plan was loaded from the iDMS database and 2D kV stereoscopic imaging coupled with the 'Xsight spine' tracking method was used to detect and

correct any gross translations and rotations with a zero action-level from the planned phantom position. Once completed, the phantom was translated (in 3DOF) to the fiducial alignment position using known translations between the alignment plan and the treatment plan. The treatment plan was then loaded.

2.4.1.1 Static treatment delivery

For the static delivery plans, the phantom motion was disabled. 2D kV stereoscopic imaging was optimised for image quality to allow accurate identification of the electrodes. The automated fiducial matching algorithm accompanied by manual correction was used to localise using the ICD electrode tips. As per the clinical workflow, the on-treatment localisation accuracy metrics, namely 'rigid body error,' 'fiducial uncertainty', 'dxAB' and 'drAB'¹ were used to minimise the set-up uncertainty. In all plan deliveries, rigid body error and dxAB were both maintained at less than 0.5 mm. Although residual corrections would be applied to the linac robotic manipulator position, all corrections were < 0.5 mm and < 0.3 degrees. Where necessary to reduce detected set up uncertainty to < 0.5 mm, electrodes were de-selected. A minimum of 1 electrode was required for treatment delivery in line with clinical practice.

Once the set-up uncertainty levels were reached and visual assessment was satisfactory, the plan was delivered with subsequent on-treatment imaging disabled to

¹ Because the kV stereoscopic imaging planes are both from the anterior-lateral oblique directions, the craniocaudal position of the surrogate is detected independently on each image plane with respect to the reference position, xA and xB. The average position is used for treatment delivery but the difference between the positions (dxAB) is quoted. drAB is the equivalent metric for differentially detected rotation about the craniocaudal axis.

minimise delivery time. All treatment plans were delivered as intended with an approximate total treatment delivery time of 30 minutes.

2.4.1.2 Dynamic treatment delivery

For the dynamic delivery, the CIRS phantom motion management was set using identical parameters to those used for 4DCT acquisition, namely the respiratory waveform with a time period of 4 seconds, amplitude of 10 mm peak-trough for both the target and the surrogate. The Synchrony LEDs were taped to the phantom surrogate 'chest' platform and the LED detection camera was focussed on the LEDs.

On the treatment console the alignment of the phantom followed the process above for static delivery up to the point of disablement of the Synchrony system. For the dynamic delivery, this feature was enabled, and a respiratory model was built using the correlation of the position of the ICD electrodes from kV imaging to that of the external LED surrogate throughout its motion. The model was built ensuring full coverage of the motion amplitude, visually inspecting each image pair to ensure that the positional detection of the electrode was accurate. In addition to the set-up uncertainty metrics used in section 2.4.1.1, the additional metric of correlation error (that which quantifies the position of the model points versus the linear best fit model) was examined to ensure it was < 0.5 mm for all plan deliveries.

All treatment plans were delivered as intended with an approximate total treatment delivery time of 55 minutes.

2.4.2 Varian VMAT treatment delivery

The phantom with loaded film was set on the couch and the central phantom external marks aligned with the room lasers.

kV CBCT imaging is the typical method for patient localisation for cardiac SABR using the anatomy of the heart itself (with a potential additional check of the ICD electrodes/wires), as such the imaging for this research reflected this. For all Varian Truebeam imaging, 125 kV and exposure settings were increased to 405 mAs to improve the image contrast between the cardiac insert phantom elements. The field of view was sufficient to encompass the phantom outline in all planes.

2.4.2.1 Static treatment delivery

The phantom motion was disabled using the CIRS motion management software and the plan loaded from the Varian database. The 3D CBCT acquisition was overlaid for co-registration with the reference (3DCT) image and interpolated to the reference image resolution.

Gross manual translations followed by the Varian mutual information algorithm were used to correct the position of the phantom in 6 degrees of freedom. Manual correction was permitted as the final step if it was deemed that the outcome of the automatic registration could be improved. Finally, visual inspection was used reflective of the clinical workflow to assess the quality of the localisation using the myocardial border as the primary registration source followed by ICD electrode positions. 6DOF couch correction with a zero action-level was implemented.

A verification CBCT was then acquired in the couch-corrected position and the registration repeated. Where the residual error was < 0.5 mm in any direction or < 0.3 degrees about any axis, plan delivery was permitted otherwise an additional correction was made and CBCT imaging repeated. enough to be practical whilst maintaining adequate precision delivery. There were no instances where the number of CBCT scans were greater than three for any delivered plan.

All treatment plans were delivered as intended. The 6MV static delivery time was approximately 15 minutes, with the 6FFF static delivery time approximately 7 minutes.

2.4.2.2 Dynamic treatment delivery

For the dynamic imaging and delivery, the CIRS phantom motion management was set identically to the 4DCT image acquisition and the RGSC block was mounted on the phantom surrogate platform such that it was detectable by the Varian RGSC camera.

The Varian gating workflow was used to detect the motion of the phantom surrogate only with the gating window selected to acquire images in the intended reference phase near to end-expiration. The gating window used maintained target amplitude difference of ± 1 mm (30% duty cycle) or ± 2 mm (60% duty cycle). The same gating configuration setting was used throughout prospective gated CBCT imaging and gated delivery to ensure consistency.

The exposure parameters were equivalent to those used for the static phantom planned deliveries. Once the gated CBCT image was reconstructed it was overlaid for co-registration with the reference image (4DCT 50% phase, near end expiration). The

same process for co-registration and subsequent couch corrections was used as for the static setting. Following 6DOF couch correction, confirmatory CBCT imaging was acquired using the gated 4DCT imaging type with the same parameters excepting that the craniocaudal (direction of motion) tolerance for residual error was set at 1.0 mm rather than 0.5 mm to reflect the dynamic nature and the finite gating window employed. A maximum of 3 gated CBCT studies were used per plan.

Treatment delivery then commenced, maintaining the phantom motion and gated treatment delivery window identical to that used for gated image acquisition.

All plans were delivered as intended. The 6MV dynamic plan delivery time was approximately 60 minutes, and the 6FFF plans was between 13-25 minutes (duty-cycle dependent).

2.5 Dosimetric analysis methods

2.5.1 Measured dose

Following each plan delivery, the EBT-3 films were removed from the phantom and placed in a dark envelope for at least 24 hours along with the pertinent calibration films until scanning.

Each film (posterior coronal plane and anterior oblique plane) was placed on the Epson 750 Perfection scanner glass with the film centred laterally on the scanner plate. The two calibration check films were placed on the scanner simultaneously, minimising rotation with respect to the light source motion direction. The Perspex plate covered the phantom film and the calibration check films and was used to centralise the films in the lateral direction to minimise the laterality artefact.

Films were all scanned using the Epson scan software in Professional mode to a .tif format using 75dpi resolution (~0.3 mm pixel size) in transmission mode using 48-bit pixel depth with all colour corrections disabled.

The .tif file produced was then imported to the SNC Patient software by extracting the (16-bit) green single channel and then converting to dose using the absorbed dose calibration curve appropriate to the beam quality delivered. The resulting file type is a .film file which is essentially a text file read by the SNC Patient software.

The calibration films were then used to calculate the film blackening correction factor. Following this, the film was then post-processed to remove edge and calibration film artefacts and to apply the total dose scaling factor that incorporated the film blackening factor and the daily linac output factor (section 2.2.5).

2.5.2 Calculated dose

The 3D dicom dose file from each treatment planning system was imported to the SNC Patient software.

The AB planned dose plane is a direct coronal plane and so was extracted from the 3D dose data using knowledge of the 3D co-ordinate origin from the treatment planning system.

The BC planned dose plane required more sophisticated extraction from the 3D planned dose volume because it was non-cardinal in nature. Co-ordinates were found from the TPS that defined the BC dose plane and used in the SNC Patient software (dose plane extractor tool). The resulting extracted dose plane did not use the original co-ordinate convention and so the origin of the reference dose was identified by use of the known position of extremes of the dicom dose data edge in each dimension.

2.5.3 Dosimetric analyses

SNC Patient software was used to quantitatively compare planned and delivered doses in the same co-ordinate convention and using the same geometric origin by means of spatial co-registration.

For gamma tests to examine the goodness of dose gradients, a minimum threshold of 10% was applied to remove the very low doses from analyses, partly due to the reduced film dose reliability in the very low dose range, but also due to the reduced importance of the low doses in relation to OAR dose tolerance magnitude. This

threshold would be a maximum of 3.5 Gy in a single fraction but would be smaller where the target did not bisect the PTV.

The data above the minimum dose threshold was examined in absolute dose mode to calculate the percentage of points that meet $\gamma < 1$ using gamma indices of 5%/1mm and 3%/2mm in both local and global terms.

Follow gamma map analyses, because the software offered no facility to calculate mean distance-to-agreement, visual examination of the calculated vs measured isodose overlays and profile analyses in the craniocaudal and transverse directions were used to determine whether there was a geometric offset was present in the plane of the film. Where geometric deviations of at least 1 mm were observed, a spatial correction was applied to the in-plane planned dose and the improvement in the 5%/1mm gamma test pass rate was used to attempt to improve the 5%/1mm gamma index pass-rate to above 95%.

The same test for spatial offset was applied in the direction perpendicular to the plane of the film by comparing calculated dose planes parallel to the reference plane (in 1 mm increments) with the measured film dose planes and again attempting to improve from the initial 5%/1mm gamma pass rate.

The magnitude of all spatial corrections for each film measurement were plotted independently for the 3 principal directions in figures 3.21 – 3.23 and the median spatial correction required for each dimension was calculated in lieu of mean distance to agreement metric for each delivery type.

Given the lack of independent point dose measurement in this study, following spatial corrections described above, an examination of the magnitude of dose difference between the measured dose and calculated dose in the high dose region was performed. For this test, a minimum dose threshold was set at the prescription dose (where prescription dose was present on the film), otherwise the minimum threshold was set at 80% of the maximum planned dose to the film. For included dose points for each film, the mean difference between the measured film dose and the calculated dose as a percentage of the calculated dose was produced along with its standard deviation.

These dose gradient, geometric error and dose difference metrics were used to characterise the dose delivery accuracy for both systems and both techniques for all four treatment delivery types.

In an acknowledgment of the limitation of the 2D gamma test in a 3D dose environment, the TPS-calculated dose gradients perpendicular to the plane of measurement were also examined in order to establish the relative sensitivity of the 2D gamma test result to the out-of-plane dose gradient. This was calculated systematically by drawing a 1D profile between the geometric centre of the PTV and the dose plane in question, remaining in the same craniocaudal plane. The modulus of the mean 1D dose gradient within 5 mm of the reference plane of interest along the line connecting with the PTV geometric centre was calculated.

The maximum planned dose in the dose plane of interest was also recorded to establish whether the dose plane contains the target and to illustrate any association

between apparent dose difference and the magnitude of the dose in the plane of the film.

2.5.4 Measurement Reproducibility

Section 2.2.6 specified the steps undertaken to characterise and mitigate the dominant sources of uncertainty arising from using film as a dosimeter. In addition to this, further experimental measurements were undertaken to characterise the reproducibility of the dosimeter.

Firstly, 5 repeat exposures were performed of the EBT-3 calibration films using 25 Gy intended dose using the procedures detailed in section 2.2.3 and 2.2.5. All 5 independent calibration films were exposed throughout a time period of no longer than 20 minutes and were book-ended by measurement of the linac standard output using a calibrated field ionisation chamber. More than 24 hours later, the films were independently scanned, converted to dose and analysed according to the process set out in section 2.5.1 to determine the reproducibility of the calibration film process to account for film blackening and linac output variation. The results of the film dosimetric reproducibility measurements are outlined in section 3.2.3.

Secondly, repetition of a full end-to-end dosimetric evaluation (measurement and analysis) was completed a further three times for a single treatment plan, namely Truebeam PTV1 (static mode) in order to validate the estimate of uncertainty. The radiation plan delivery processes exactly followed that set out in section 2.4.2.1 and were delivered sequentially in the same delivery session. The analysis of each repeated

plan was performed identically and as set out in section 2.5. The same primary gamma test criterion, namely 5%/1mm (10% threshold), was applied to the reproducibility measurements. Dosimetric plan reproducibility results are presented both prior to, and after, a 1 mm spatial correction to allow for direct comparison with the main results (section 3.4, table 3.12).

Because any variation seen in this end-to-end measurement result would encapsulate both variability due to the dosimeter itself, the processing & analysis method, and treatment delivery accuracy; this should act to validate the overall measurement uncertainty estimate (as specified in section 3.2.4) and thus provide assurance of the reliability of any single end-to-end delivery result published throughout the remainder of this thesis.

Chapter 3: Results

3.1 Phantom design & fabrication

3.1.1 Material selection results

A photograph and CT scan of the first sample print of the shortlisted 3D print materials of Vero White and Agilus Black are shown in figure 3.1 printed in a checkerboard arrangement. Initial indications revealed that despite similarity in physical density, the contrast for kV CT imaging was likely to be sufficient for localisation if these materials were used for cardiac component analogues.

The relative electron densities from the CT scan are shown in table 3.1. Although it was recognised that the physical densities and relative electron densities were higher than the anatomic equivalents, any smaller difference in relative electron densities might have led to an inability to differentiate in terms of image contrast, especially using CBCT. The highest rigidity Agilus Black mix was chosen to proceed as there was no contrast difference detected across the range of rigidities tested.

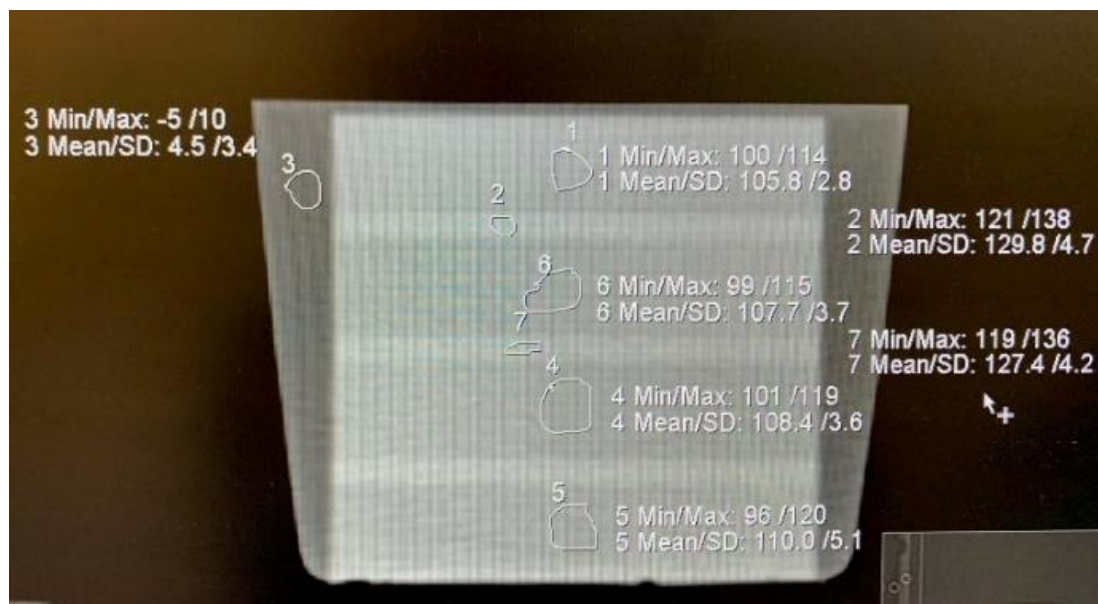
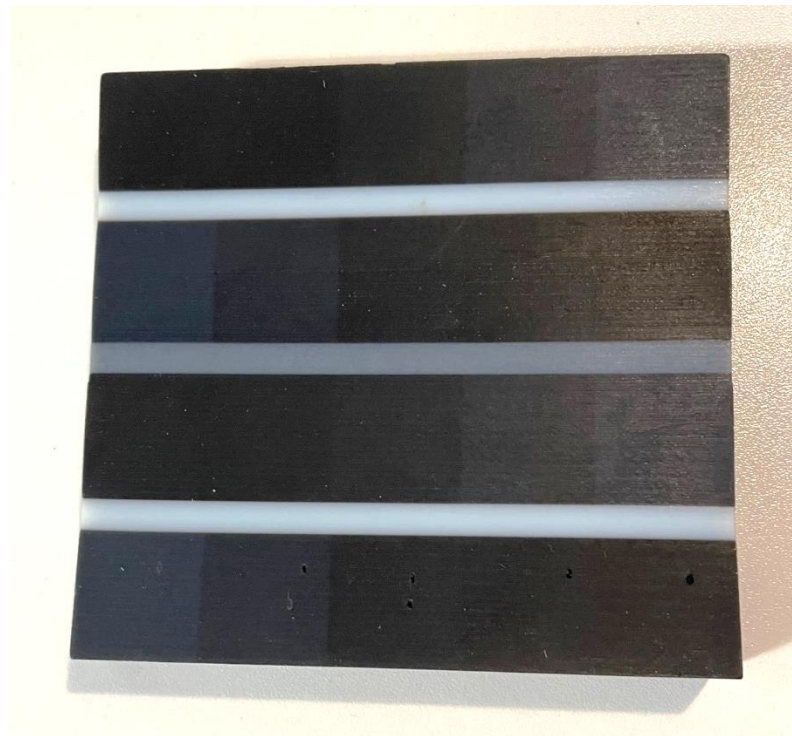


Figure 3.1 Top: Photograph of checkerboard sample; Bottom: corresponding CT scan in water. Result demonstrated no discernible contrast horizontally between different Agilus Black rigidities, but contrast was exhibited in the vertical direction between the Vero White and the Agilus Black sections of approximately 20 - 24 HU (1 s.d. of approximately 5 HU)

Anatomical feature	Relative electron density anatomical feature	Relative electron density 3D print materials	Mean physical density (gcm ⁻³) 3D print materials
Blood pool	~1.05	1.11 (Agilus Black)	1.145
Myocardium	~1.05	1.27 (Vero White)	1.175

Table 3.1 Relative electron densities of anatomical and analogue cardiac components based on CT scan conversion from Hounsfield Units

In examination of the hybrid material method, the first combined sample is illustrated in figure 3.2, and the corresponding CT-based relative electron densities in table 3.2.

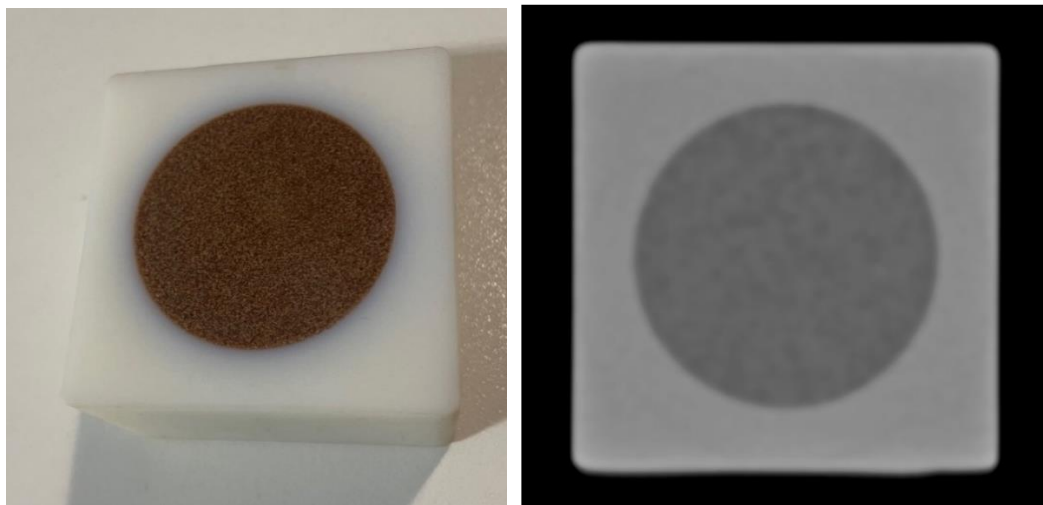


Figure 3.2 Left: Photograph of hybrid sample; Right: corresponding CT scan. Hounsfield unit testing demonstrated contrast between the Vero White and water equivalent material of approximately 130 HU with no bleeding of one material in to the other

Anatomical feature	Relative electron density anatomic component	Relative electron density 3D print/hybrid materials	Mean physical density (gcm ⁻³) 3D print/hybrid materials
Blood pool	~1.05	1.00 (Water equivalent)	1.00 (Water equivalent)
Myocardium	~1.05	1.27 (Vero White)	1.175 (Vero White)

Table 3.2 Relative electron densities for the hybrid phantom model

Contrast between the two elements was found to be amplified compared with the fully 3D printed sample and the integrity of the phantom was maintained with no bleeding of the water-equivalent material into the printed material. However, although use of a water-equivalent material would have been more accurate representation of the blood pool itself in terms of physical density and electron density, this would have introduced a more significant (27%) difference in relative electron density between the myocardium and the blood pool analogues (table 3.2).

Although this would have aided in image contrast definition for pre-treatment and treatment imaging it would have been less reflective of the anatomical situation in terms of the treatment beam radiation characteristics as blood and muscle tissue have much closer electron densities (both being between $3.4 \times 10^{23} \text{ cm}^{-3}$ and $3.5 \times 10^{23} \text{ cm}^{-3}$) (Shrimpton, 1981) compared with an electron density of water² of $3.3 \times 10^{23} \text{ cm}^{-3}$, i.e. both having a marginally elevated electron density relative to water of approximately 1.05.

² The molecular weight of water is 18amu and its density is 1 gcm^{-3} meaning that in 18 cm^3 of water there would be 6.023×10^{23} molecules of water. With 10 electrons per molecule (H_2O) then the number of electrons per cm^3 of water is $(6.023 \times 10^{23} / 18) \times 10 = 3.3 \times 10^{23} \text{ cm}^{-3}$.

Furthermore, the highly tortuous shape of the myocardium meant that it would have been difficult to achieve complete filling of the chamber cavities and vessel lumen without leaving air bubbles that would have been dosimetrically detrimental if they were close to the dose measurement planes.

Based on the results of material selection experiments, balancing the aspects of image contrast, relative electron densities, geometric fidelity, and reproducibility of a model able to achieve adequate 3D anatomical shape complexity, computer modelling and 3D printing using the most suitable materials available was selected for the method of production of the cardiac insert. This approach also removed the need for expensive and rare facilities to produce water-equivalent material on-site. As a result of these experiments, a hybrid model was rejected, and a model built exclusively using 3D printing was selected to proceed.

3.1.2 3D computer modelling

Using the methods set out in 2.1.2, the following anatomic features in table 3.3 were identified for the cardiac model.

Soft tissue element	Blood pool element
A Left atrium wall	J Left atrium chamber
B Right Atrium wall	<i>Right atrium chamber not visible</i>
C Left ventricle wall	K Left ventricle chamber
D Right ventricle wall	L Right ventricle chamber
E Aorta wall	M Aorta lumen
F Vena cava wall	N Vena cava lumen
G Pulmonary veins wall	<i>Pulmonary veins lumen not visible</i>
H Pulmonary arteries wall	O Pulmonary arteries lumen
I Left anterior descending coronary artery	

Table 3.3 Anatomical component masks produced from the anatomical CT data using Mimics Materialise 3D modelling software. The allocated letter pertains to the position on the diagram in figure 3.3, where visible

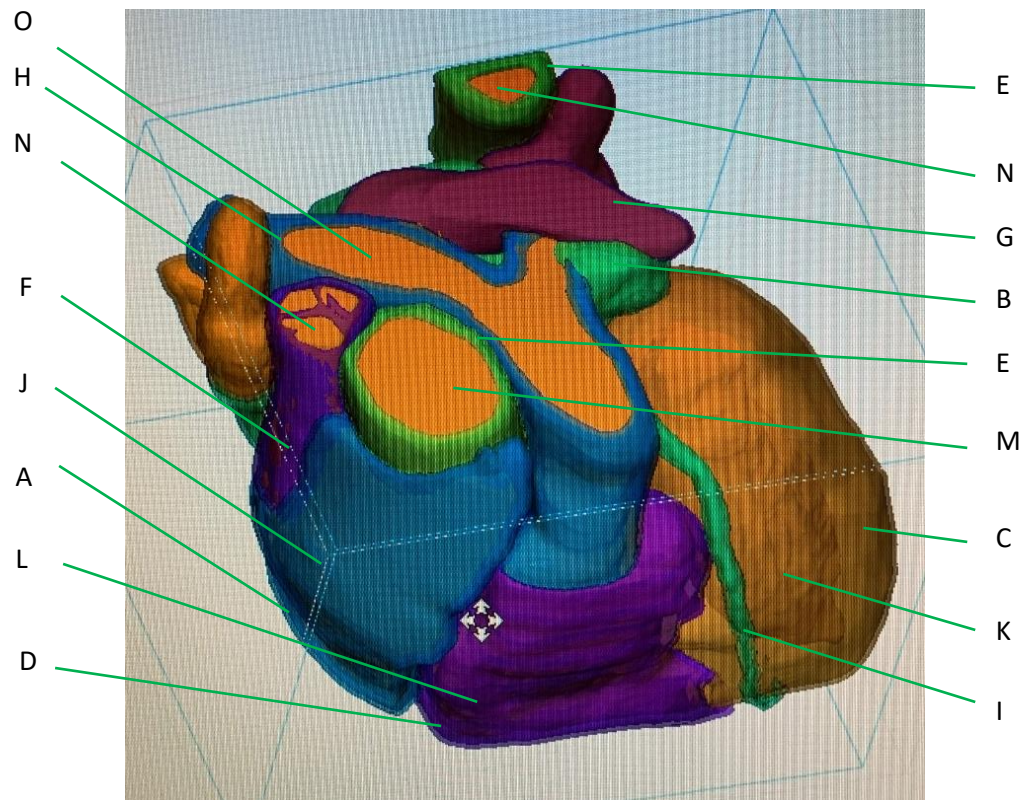


Figure 3.3 3D segmented model of anatomical heart on contrast-enhanced CT, superior-anterior-right oblique view. Labelled (where feature is visible) according to Table 3.3

The model was then used to identify pertinent dose measurement planes. The first plane bisects the posterior aspect of the right atrium through the pulmonary trunk bifurcation through to the left ventricular apex. This plane contains the base, the SA node, the AV node, and the posterior aspect of the left ventricle (figure 3.4).

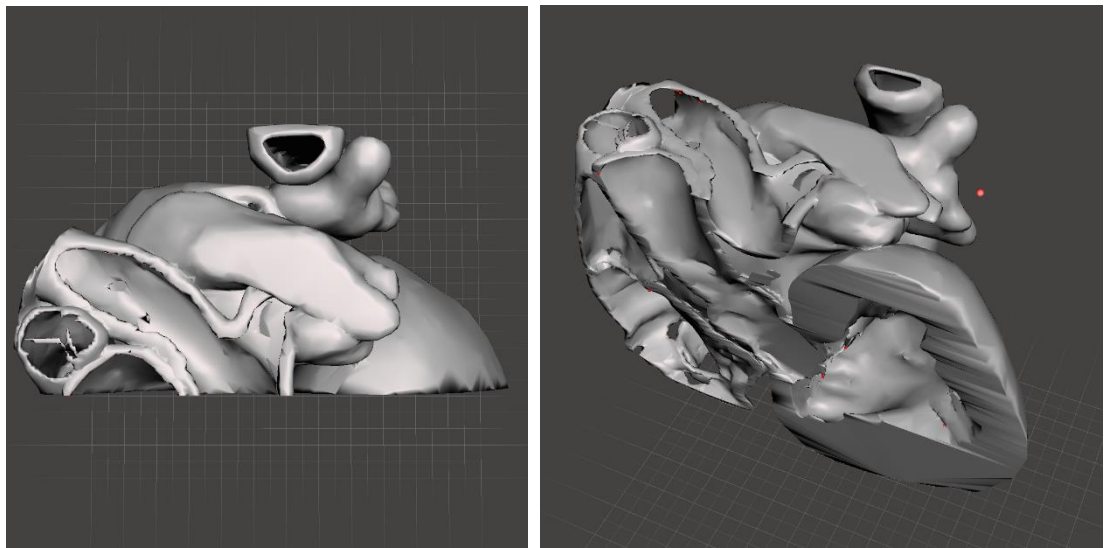


Figure 3.4 Posterior cardiac part (myocardium showing only). Left: superior view; Right: anterior-left-superior oblique view revealing dosimetric plane AB

The second plane is more anterior to the previous that depicts the R ventricle, the anterior aspect of the LV, the interventricular septum, and the LAD coronary artery. This is effectively a three-chamber (oblique coronal) view that bisects the intra-ventricular septum which produces a central section appearing in figure 3.5.

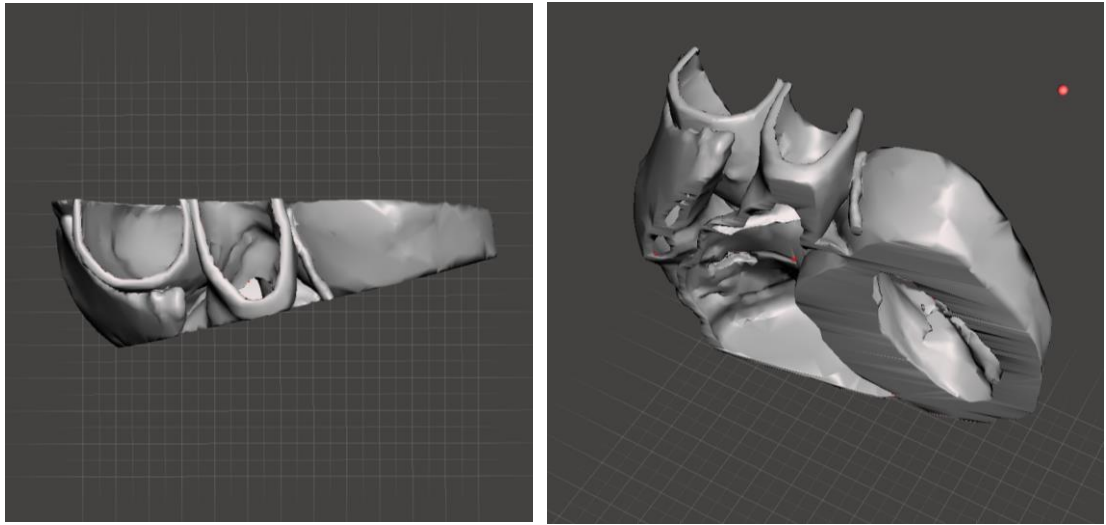


Figure 3.5 Central cardiac part (myocardium part only shown). Left: superior view; Right: anterior-left-superior view revealing dosimetric plane BC

The remaining anterior section completes the 3D model (figure 3.6).

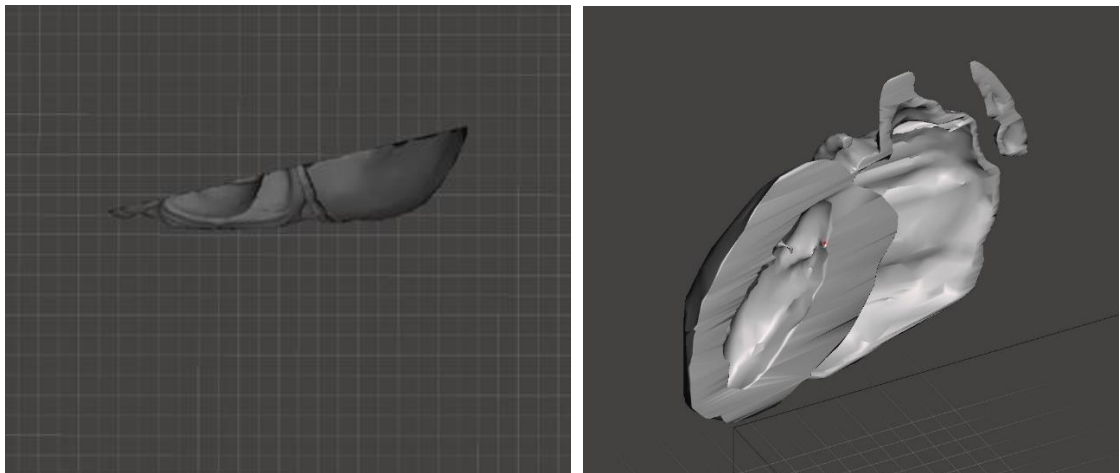


Figure 3.6 Anterior cardiac part (myocardium part shown only). Left: superior view; Right: anterior-left-superior view revealing dosimetric plane BC

The combination of the cardiac with the extracardiac components arranged as 3 distinct modules within a cylindrical insert and completed with holes for the ICD electrodes and fittings for modular assembly is seen in figure 3.7.

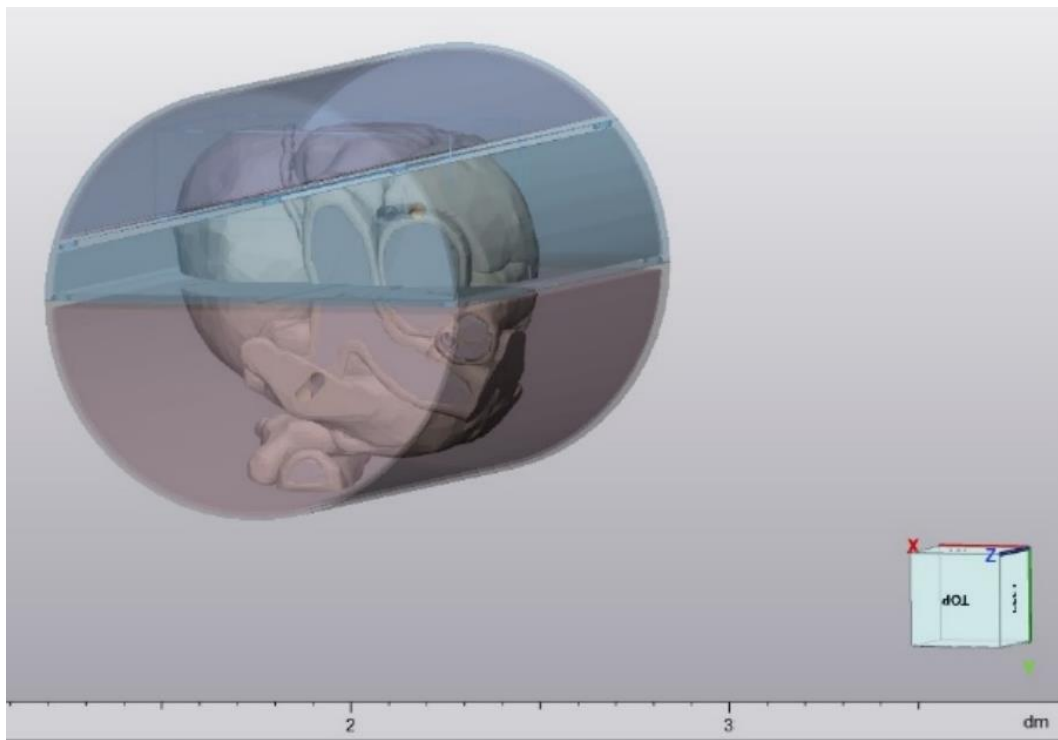
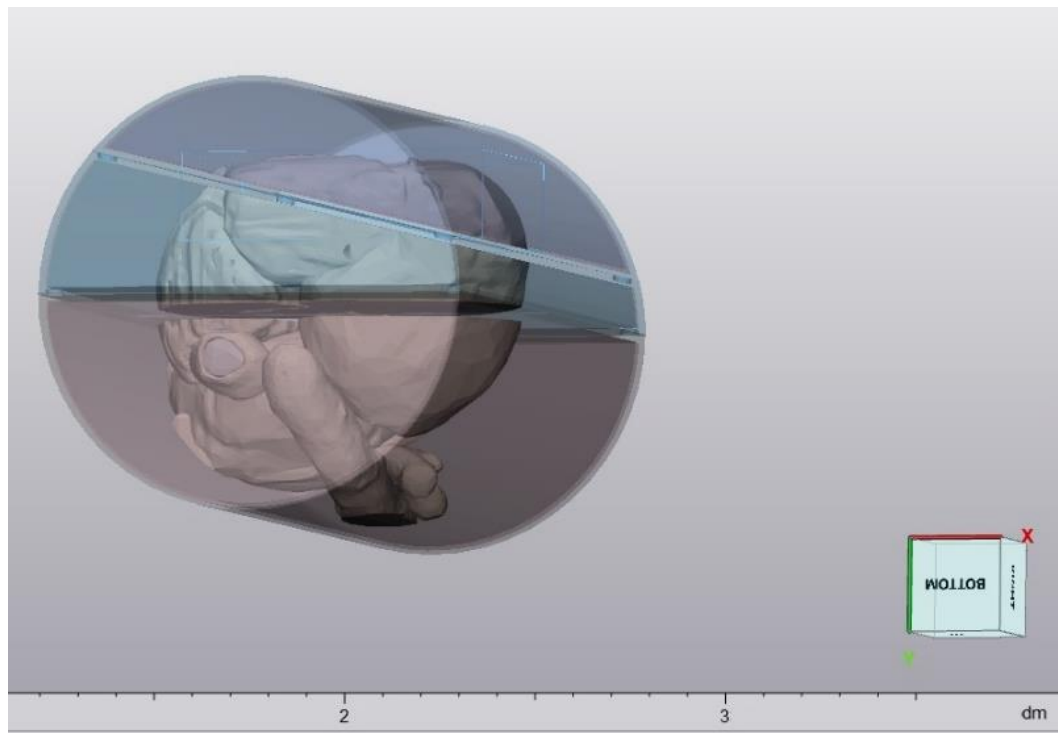


Figure 3.7 The final 3-part modular cardiac insert design indicating the split planes and the holes for ICD electrode positioning. Top: inferio-left lateral view; Bottom: superio-right lateral view

3.1.3 Prototyping to final phantom production and assembly

The first prototype print from the 3D computer modelling employing the selected materials (3.1.1) is illustrated in figure 3.8.

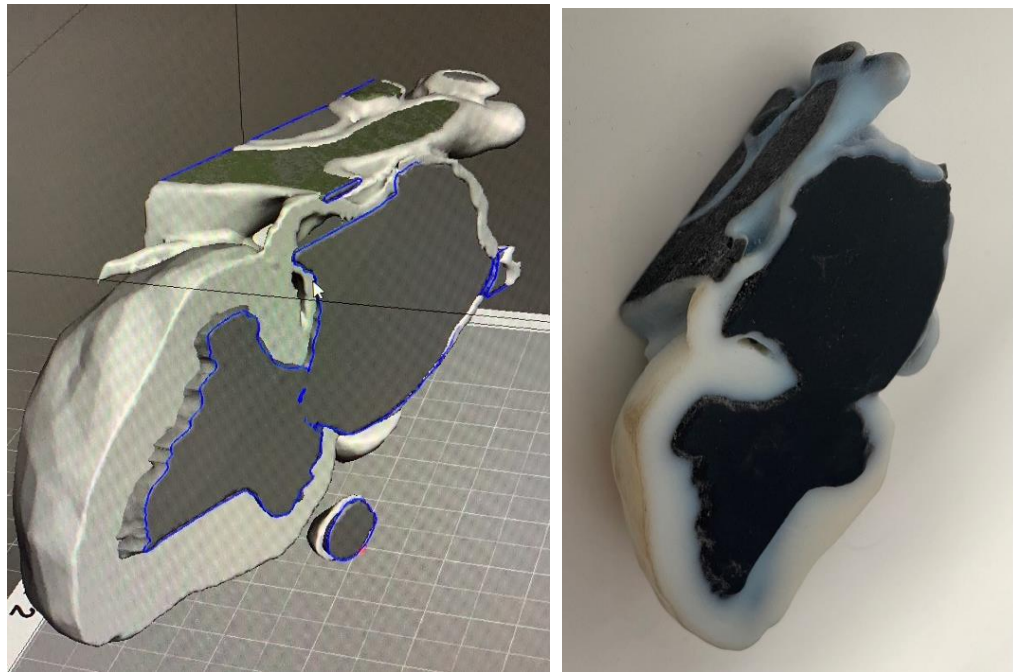


Figure 3.8 First anthropomorphic prototype. Left: 3D computer model section cut in the plane through the left ventricle and left atrium (grey) and blood pool (black); Right: a photo of the corresponding 3D printed part indicating accuracy of 3D print reproduction

This model was then CT scanned to ensure adequate imaging contrast for the anatomical model complexity (figure 3.9).

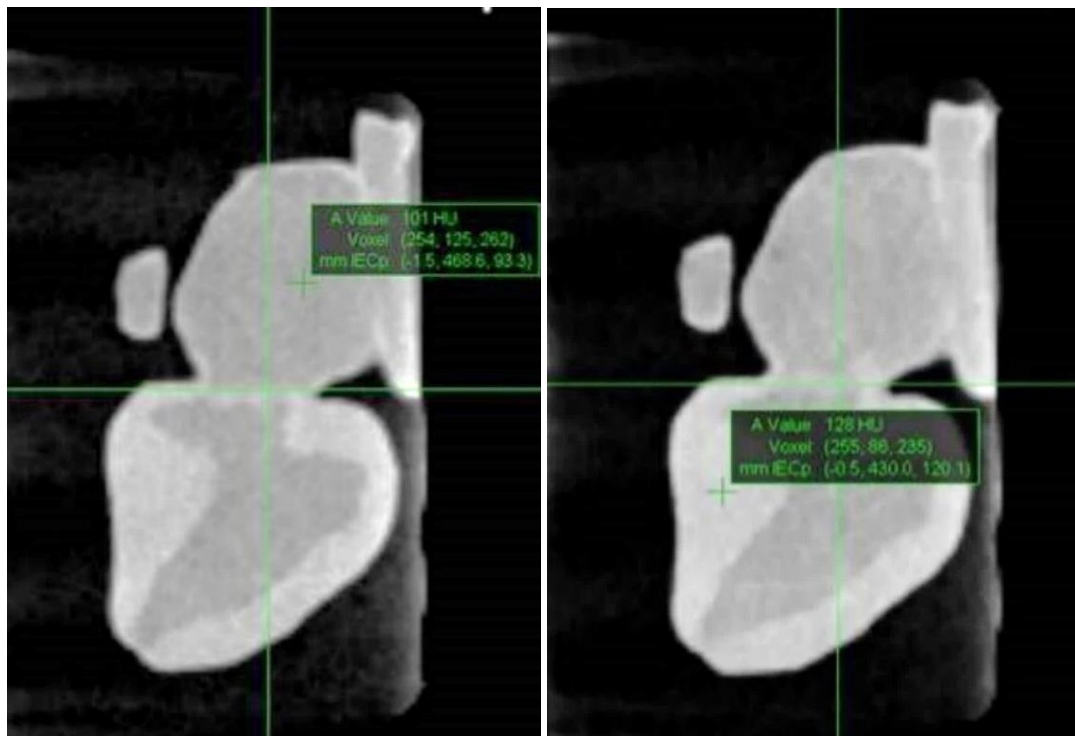


Figure 3.9 First anthropomorphic prototype CT result illustrating discernible contrast between the blood pool and myocardium elements of the structure (HU values indicated)

The 20 - 30 HU differences seen in the first sample prints (section 3.1.1) were maintained in the clinical model which was sufficient to visualise contrast even between the thin-walled structures (such as the vessel walls and the atria walls) and the blood pool.

The addition of the extracardiac 3D print material was required in Agilus Black in order to maintain contrast between it and the myocardium. This was prototyped in figure 3.10.



Figure 3.10 Prototype including of the addition of the extracardiac elements using Agilus Black 3D print material to surround the Vero White myocardial and vessel wall elements

Although it was recognised from table 3.1 that the Agilus Black would provide adequate image contrast and also a reasonable analogue of the relative electron difference between the myocardial elements and the surrounding pericardial fat (a difference of approximately 16%), the material demonstrated significant lack of rigidity and the undesirable introduction of air gaps (figure 3.10). Following this prototype production, it was clear that it would be necessary to frame the extracardiac component to ensure the geometric fidelity and remove any air gaps in the final model production.

The completed phantom insert in situ in the Dynamic thorax phantom appears in figure 3.11.

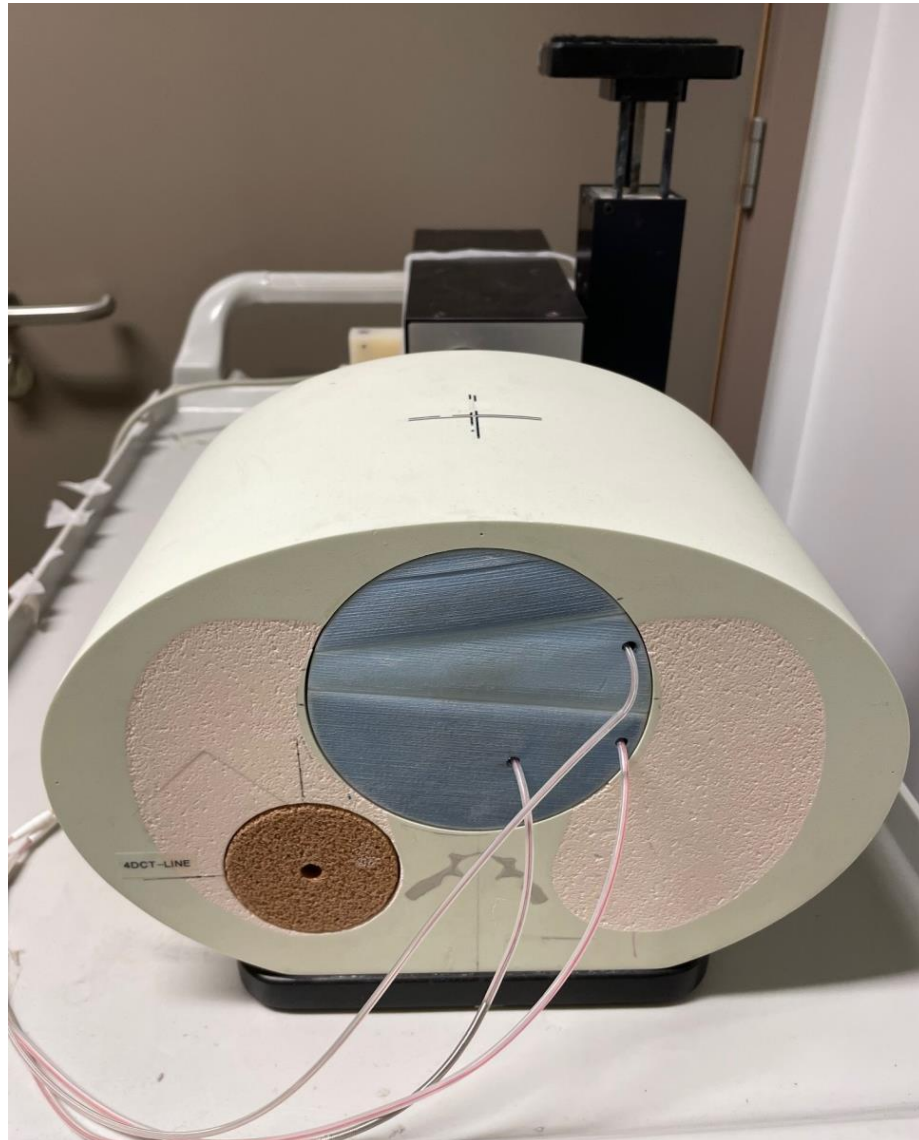


Figure 3.11 Photo of the insertion of the cardiac modular phantom inside the CIRS dynamic thorax phantom viewed from the superior aspect of the phantom. Note the goodness of fit both between modular components and between the insert and the thorax outer phantom

A CT scan of the whole phantom can be seen in figure 3.12.

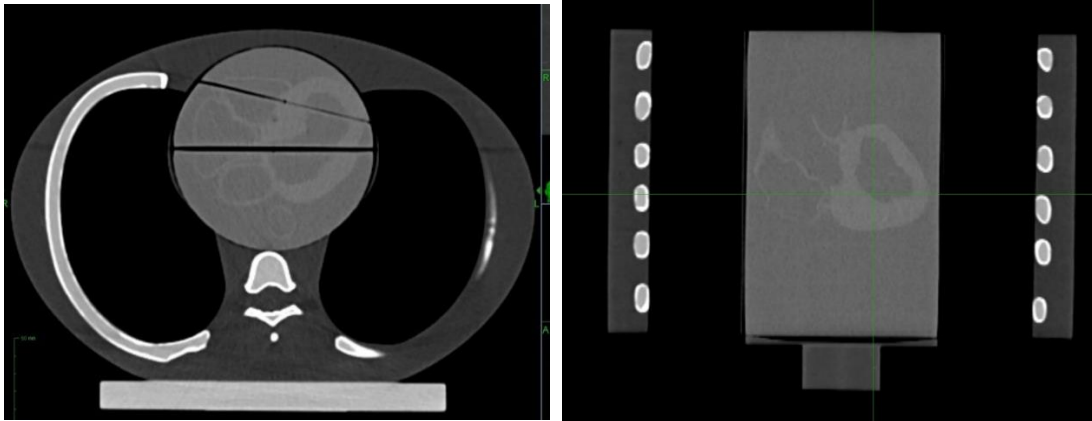


Figure 3.12 CT images of phantom: Left: axial cross-section indicating the AB and BC planes; Right: coronal view. Both planes indicate high quality of fit between the modules and with the thorax phantom. Also demonstrated is adequate image contrast between the cardiac and non-cardiac elements and the appropriate relative anatomical size and positioning with respect to the remainder of the thorax

3.2 Radiochromic Film Characterisation

3.2.1 Radiochromic film colour channel for batch dose calibrations

Batch dose calibration data for EBT-3 film performed for this study is illustrated in figure 3.13 and compared against published data for EBT-XD film. Although there is an offset in terms of pixel value per unit dose, the gradient of the curves (sensitivity) beyond 5-10 Gy are not dissimilar.

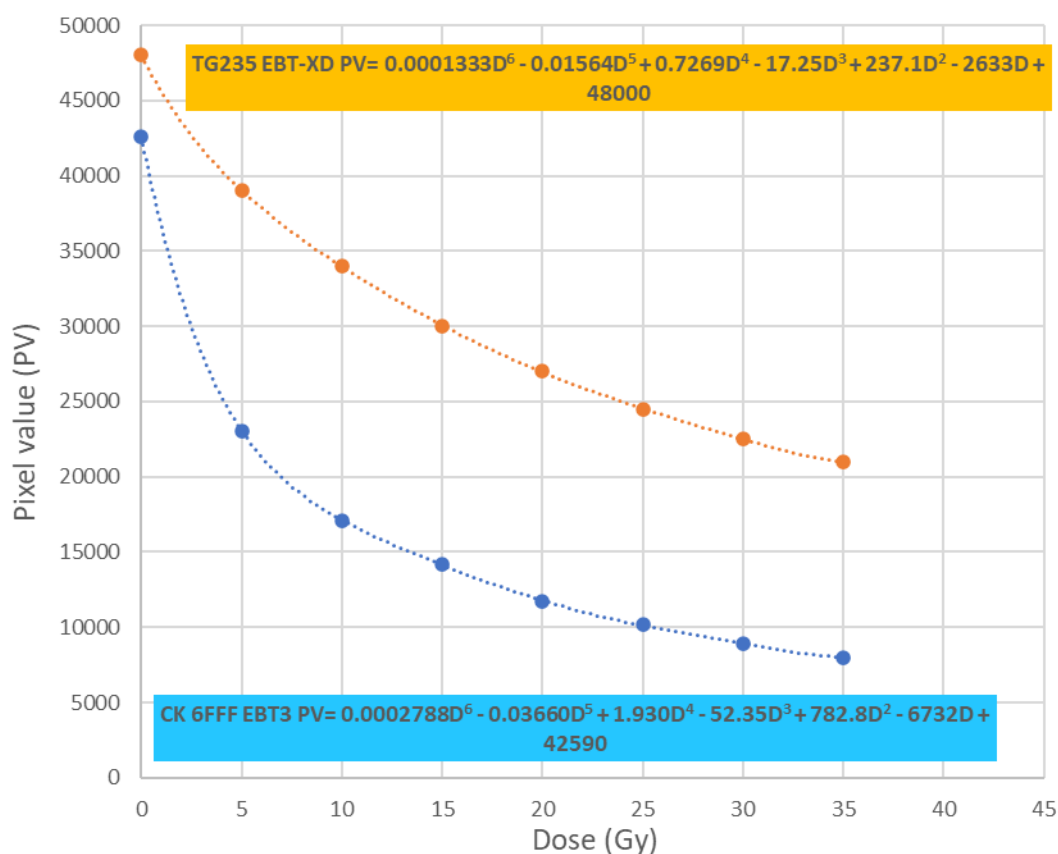


Figure 3.13 Differences in dose calibration relationships between radiochromic film types for the green channel. Points are calibration values, dotted line 6th order polynomial

To further examine the level of potential detriment to using EBT-3 for this study, the first derivative of the polynomial function was plotted for examination in figure 3.14.

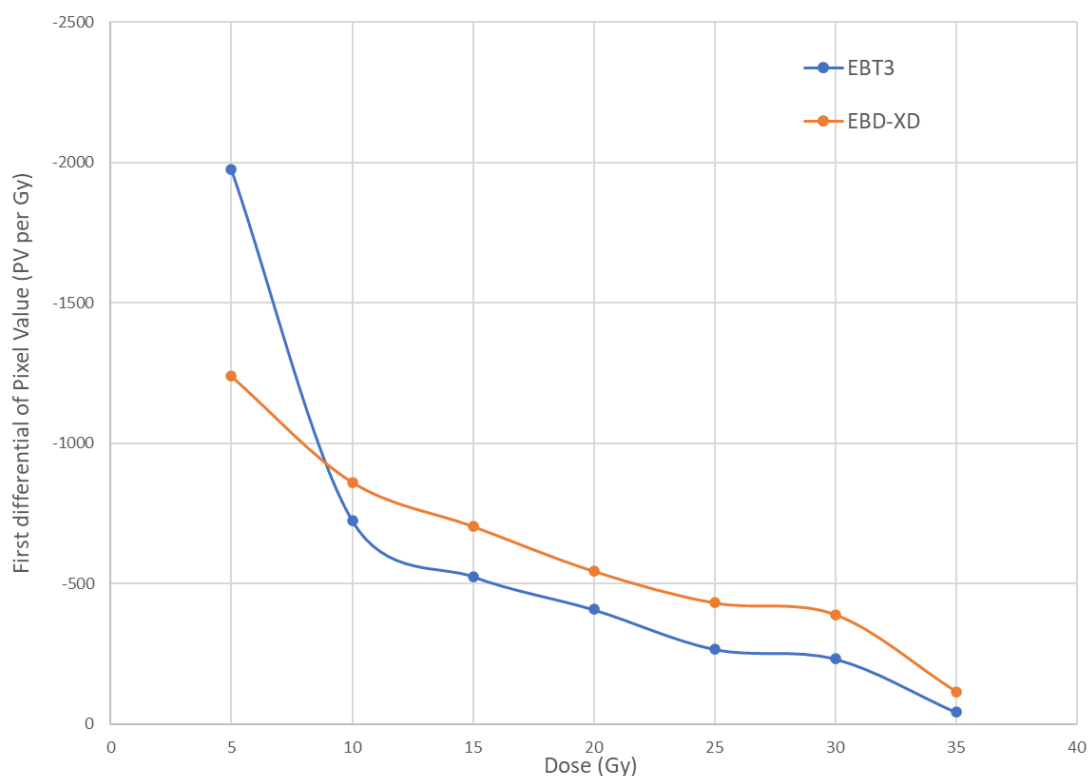


Figure 3.14 First derivative of dose relationship with pixel value indicating differences in film sensitivity between EBT-3 and EBT-XD radiochromic film as a function of absorbed dose, both for single (green) channel, polynomial trendline

Figure 3.14 illustrates only a relative minor reduction in sensitivity of the EBT-3 film compared with EBT-XD film for much of the dose range of interest for this study. There remain hundreds of pixel values per unit Gy of absorbed dose to at least the 30 Gy level which is sufficient in context of required precision of the order 1%. Film saturation (zero value of first derivative) is not demonstrated. Dose distributions in this study will be characterised by a 25 Gy circumferential prescription dose i.e., doses higher than this shall be within the PTV and so are of relatively lower importance

compared with the doses in the 10-25 Gy range that shall characterise target coverage and organ at risk doses.

The results for quantifying uncertainty estimation in the batch dose calibrations are detailed in table 3.4. These uncertainties were found by comparing each discrete point used in the calibration against the dose modelling for that pixel value according to the batch calibration exponential function. The standard deviation of the differences between modelled dose and delivered dose throughout the calibrated range was established to characterise the standard uncertainty in the batch calibration.

Calibration curve for modality	Mean dose difference (%)	Standard deviation dose difference (%)
CyberKnife 6FFF	0.4	1.8
Varian 6FFF	-0.3	1.2

Table 3.4 Batch film calibration uncertainty characterisation

3.2.2 Geometric distortion artefacts

Lateral film response was measured by exposing EBT-3 film to a known homogeneous dose in solid water. The film was scanned centrally on the glass plate with the Perspex sheet overlaid to minimise the degree of film curvature on the scanner glass. The mean dose was calculated at each lateral position and normalised to the mean dose over the central 10 mm. The result appears in figure 3.15.

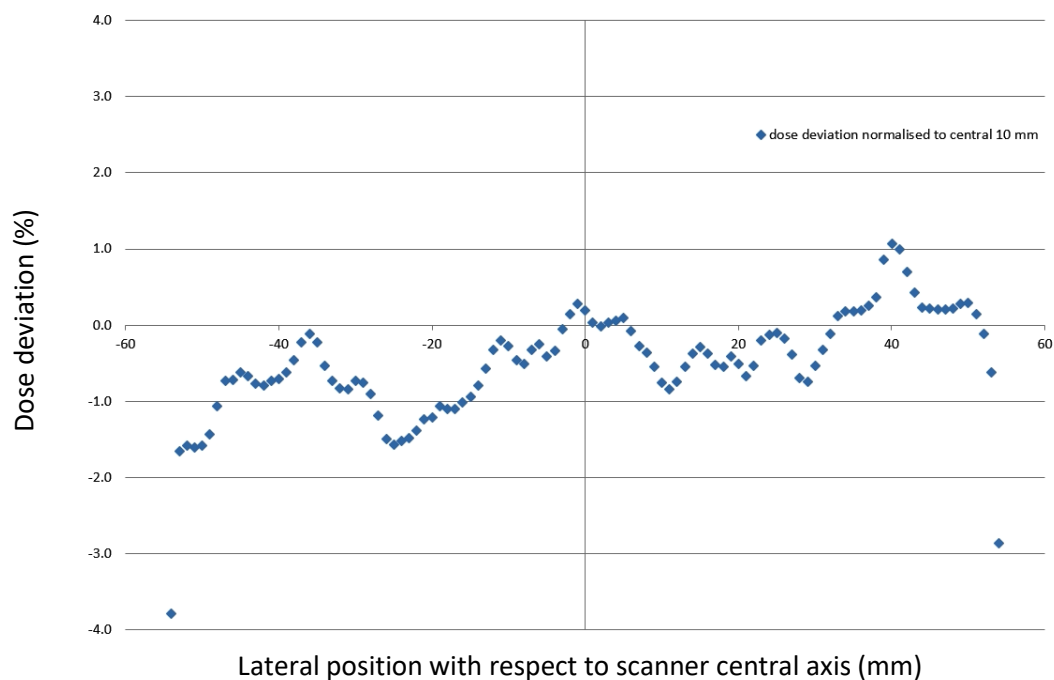


Figure 3.15 lateral film response to a homogeneous dose of radiation. Note the small magnitude systematic variation across the width of the scanner and edge of film effects

When the outermost 2 mm data points are excluded on each side due to edge of film effects, the mean dose deviation was -0.4% with an interquartile range -0.8% to 0%. This indicated that when edge of film data is removed the remaining artefacts from geometric effects were small in the context of the level of dose accuracy required in this study and an order of magnitude less than those demonstrated in the literature (Grams et. al., 2015) and so were deemed not to be detrimental to the study and interpretation of results.

Due to the potential of the Perspex as an additional object in the scanner causing a change in the light conditions, all batch calibrations and subsequent film measurements were performed with the Perspex plate in situ.

3.2.3 Film dosimetric reproducibility

The simple film reproducibility measurements are detailed in table 3.5. The five independent films were irradiated, scanned and analysed as per the procedures set out in section 2.2. The values quoted are the measured dose to the central axis of the 3 cm x 3 cm irradiated field.

Test film number	Dose	Difference to intended
	Gy	%
1	25.02	0.1
2	24.91	-0.4
3	25.10	0.4
4	25.06	0.2
5	25.02	0.1
median	25.02	0.1
upper limit	25.10	0.4
lower limit	24.91	-0.4

Table 3.5 Calibration film reproducibility measurements, compared with 25 Gy intended dose

Note that the median result is within 0.1% of the intended dose of 25 Gy, but more critically for the estimation of the uncertainty component, the variability around the median has full (and symmetric) range of only 0.8%.

The standard uncertainty could be calculated in a number of ways, however because the number of reproducibility results are small, one cannot assume that these data come from a normal distribution. In order to ensure that the uncertainty is encapsulated, it is therefore assumed that these data come from a rectangular distribution with a half range (a) of 0.4 %.

The standard uncertainty of a rectangular distribution is characterised by the following equation:

$$\text{standard uncertainty} = \frac{a}{\sqrt{3}}$$

Therefore, the estimated standard uncertainty for film dosimetric reproducibility, R, is assumed to be 0.23 %.

3.2.4 Overall estimate of measurement uncertainty

The other dominating uncertainties for this dosimeter are estimated to be due to the following:

- Laterality distortion artefact, L. From section 3.2.2, the laterality variability indicates a standard deviation of 0.70 % (k=1);
- Batch calibration curve fitting uncertainty, B. From section 3.2.1 (taking the CyberKnife data as the highest uncertainty) indicates a standard deviation of 1.80 % (k=1);
- Ionisation chamber uncertainty, C. Because the output of the linear accelerator was defined by ionisation chamber measurement and used in the integrated correction factor in order to perform the two-point film calibration to account for time-dependent blackening, this should be included. From the National Physical Laboratory ionisation chamber calibration certificate, the expanded uncertainty (k=2) is stated as approximately 1.3%, meaning that typical standard uncertainty from measurement of absorbed dose using a tertiary

ionisation chamber of between 1.4% and 2.1% (Castro et. al., 2008). Assuming achievable dosimetry of 2.1% and dividing through by a coverage factor (k) of 2 then the uncertainty in the ionisation chamber linac output, C, is of the order 1.05 %.

The above uncertainties are now all defined in the same unit of standard uncertainty and can be classified as source-independent of each other. As such, the combined standard uncertainty can be calculated as the quadratic sum of the elements defined, hence:

$$\text{combined uncertainty (\%)} = \sqrt{R^2 + L^2 + B^2 + C^2}$$

$$\text{combined uncertainty (\%)} = \sqrt{0.23\%^2 + 0.70\%^2 + 1.8\%^2 + 1.05\%^2}$$

$$\text{combined uncertainty} = 2.2 \%$$

Therefore, the standard uncertainty of the measured dose to any pixel in the radiochromic film is likely to be within $\pm 2.2\%$ of the true absorbed dose delivered to that position (k=1).

3.3 Treatment Planning results

The results of the treatment planning described in section 2.3 are detailed here.

3.3.1 Accuray CyberKnife

Summary planned dose statistics are detailed in table 3.6. A single set of planned data appears as the static and respiratory-tracked deliveries emanate from the same plan.

		Quality metric	Dose Constraint		PTV 1	PTV 2	PTV 3	PTV 4
			<i>Optimal</i>	<i>Mandatory</i>	VT apex	VT septum	VT lateral	HOCM
PTV		physical volume (cc)			22.0	31.9	16.0	16.6
		V25 Gy (cc)			20.9	30.4	14.7	15.4
		V25 Gy (%)	>95 %	-	95.0	95.3	91.9	92.8
		Max (D0.04cc)	-	< 35 Gy	33.3	34.5	35.0	34.0
Patient		V prescription dose (cc)			22.3	32.9	17.5	15.7
		V half prescription dose (cc)			77.6	107.7	56.4	49.7
		Modified Gradient Index	< 4.5	-	3.7	3.5	3.8	3.2
		Prescription Dose Spillage	< 1.20	-	1.07	1.08	1.19	1.02
Organs or devices at risk	Spinal Canal PRV	Max (D0.04cc)		< 14 Gy	1.1	3.1	2.3	1.5
		V10Gy	-	< 0.35 cc	0.0	0.0	0.0	0.0
		V8Gy		< 1.2 cc	0.0	0.0	0.0	0.0
	Heart minus PTV	Max (D0.04cc)	22 Gy	-	29.0	29.5	30.1	26.1
		V16 Gy	< 14 cc		13.7	11.1	13.3	15.2
	Left Ventricle Myocardium minus PTV	Mean	< [0.027x(volume of Left Ventricle-PTV in cc)] + 4.7 Gy. Tolerance in ()	-	5.8 (6.9)	5.7 (6.6)	7.0 (7.0)	5.6 (7.0)
	Right Ventricle	Median	< 11 Gy	-	3.9	9.2	2.7	7.1
	Coronary Arteries PRV	Max (D0.04cc)	< 15 Gy	< 18.6 Gy	12.6	0.5	18.6	7.3
	Pacing Wire Tips PRV	Max (D0.04cc)	< 6 Gy	< 12 Gy	1.9	5.0	8.1	9.8
	Great Vessels	Max (D0.5cc)		< 37 Gy	3.4	15.6	6.7	24.6
		V31Gy	-	<10 cc	0.0	0.0	0.0	0.0
	Rib	Max (D0.5cc)	< 33 Gy	-	19.5	13.5	7.9	5.3
		V28Gy	< 5 cc		0.0	0.0	0.0	0.0
	Skin Rind 5 mm	Max (D0.5cc)		< 27.5 Gy	6.0	6.4	6.5	4.9
		V25.5 Gy	-	< 10 cc	0.0	0.0	0.0	0.0
	Lungs minus GTV	V8Gy	< 37%	-	0.5	6.7	0.5	0.0
		V7.6 Gy	< 1000 cc		21.0	7.9	0.6	0.0
		V7Gy	< 1500 cc		23.9	9.7	0.8	0.0

Table 3.6 Planned dose statistics indicating that all treatment plans met at least the optimal dose constraints for the organs or devices at risk. Green indicates within optimal tolerance (if any) and orange indicates beyond optimal but within mandatory tolerance

All plans satisfied the OAR dose thresholds specified a priori. Where necessary in order to respect a mandatory dose tolerance, the target dose coverage was compromised to achieve this, however this compromise was minimal. The conformity indices and gradient indices were satisfactory, given the target complexities and competing objectives of delivery time and reducing OAR doses.

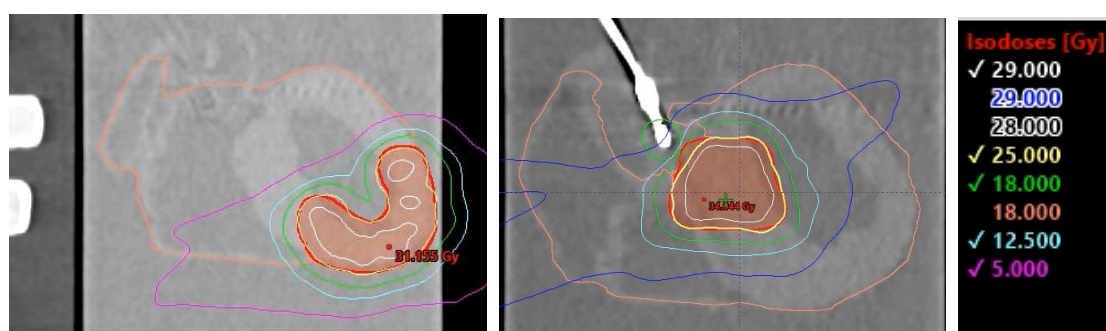


Figure 3.16 Example calculated dosimetry for left: PTV 1 (VT), right: PTV 4 (HOCM). Red semi-transparent structure indicates PTVs, pink structure indicates heart with PTV subtracted, isodoses listed

3.3.2 Varian VMAT

Summary Varian Truebeam VMAT planned dose statistics are detailed in table 3.7.

Only the 6FFF static plan details are shown as the equivalent dynamic plans bear almost identical results given identical contours were used along with identical optimisation and calculation parameters. The only difference being the phase of the motion used for the reference CT.

6X data is not displayed as investigation of this beam quality was discontinued to the treatment delivery stage due to exaggerated gated delivery times.

		Quality Metric	Dose Constraint		PTV 1	PTV 2	PTV 3	PTV 4
			Optimal	Mandatory	VT apex	VT septum	VT lateral	HOCM
PTV		physical volume (cc)			22.0	31.9	16.0	16.6
		V25 Gy (cc)			21.4	30.3	15.0	15.8
		V25 Gy (%)	>95 %	-	97.3	95.0	93.8	95.2
		Max (D0.04cc)	-	< 35 Gy	33.3	34.3	34.6	34.4
Patient		V prescription dose (cc)			24.6	32.5	17.5	16.5
		V half prescription dose (cc)			82.0	108.4	58.4	58.4
		Modified Gradient Index	< 4.5	-	3.8	3.6	3.9	3.7
		Prescription Dose Spillage	< 1.20	-	1.15	1.07	1.17	1.04
Organs or devices at risk	Spinal Canal PRV	Max (D0.04cc)	-	< 14 Gy	3.8	5.2	4.3	3.9
		V10Gy		< 0.35 cc	0.0	0.0	0.0	0.0
		V8Gy		< 1.2 cc	0.0	0.0	0.0	0.0
	Heart minus PTV	Max (D0.04cc)	22 Gy	-	29.4	28.4	29.0	26.0
		V16 Gy	< 14 cc		11.0	12.5	13.2	13.9
	Left Ventricle Myocardium minus PTV	Mean	< [0.027x(volume of Left Ventricle-PTV in cc)] + 4.7 Gy. Tolerance in ()	-	5.7 (6.9)	5.8 (6.6)	7 (7.0)	4.4 (7.0)
	Right Ventricle	Median	< 11 Gy	-	4.9	7.7	3.4	5.0
	Coronary Arteries PRV	Max (D0.04cc)	< 15 Gy	-	12.7	2.1	18.6	6.7
	Pacing Wire Tips PRV	Max (D0.04cc)	< 6 Gy	-	4.8	6.0	10.0	11.5
	Great Vessels	Max (D0.5cc)	-	< 37 Gy	6.4	13.7	7.6	26.3
		V31Gy		<10 cc	0.0	0.0	0.0	0.0
	Rib	Max (D0.5cc)	< 33 Gy	-	19.3	15.3	8.2	6.4
		V28Gy	< 5 cc		0.0	0.0	0.0	0.0
	Skin Rind 5 mm	Max (D0.5cc)	-	< 27.5 Gy	3.6	8.9	4.5	7.7
		V25.5 Gy		< 10 cc	0.0	0.0	0.0	0.0
	Lungs minus GTV	V8Gy	< 37%	-	0.9	0.3	0.7	0.0
		V7.6 Gy	< 1000 cc		35.5	13.0	30.0	0.0
		V7Gy	< 1500 cc		43.4	15.4	38.0	0.0

Table 3.7 Planned dose statistics for Varian Truebeam static plans indicating that all treatment plans met at least the optimal dose constraints for the organs or devices at risk. Green indicates within optimal tolerance (if any) and orange indicates beyond optimal but within mandatory tolerance

3.4 Treatment delivery results

All four static treatment plans and four dynamic treatment plans were successfully delivered using the Accuray CyberKnife and Varian Truebeam platforms within the conservative on-treatment tolerance limits specified in section 2.4. For each delivery both films were successfully analysed in line with the methods set out in section 2.5.

An example of a good pass for PTV 1 is illustrated in figure 3.17 and an example of an initial poor pass for PTV 4 is illustrated in figure 3.18. In figure 3.18, the data at the top shows the spatially uncorrected data and the data at the bottom shows the result following 1 mm spatial correction in two orthogonal directions. This indicates the high degree of 5%/1mm gamma test sensitivity to very small geometric errors.

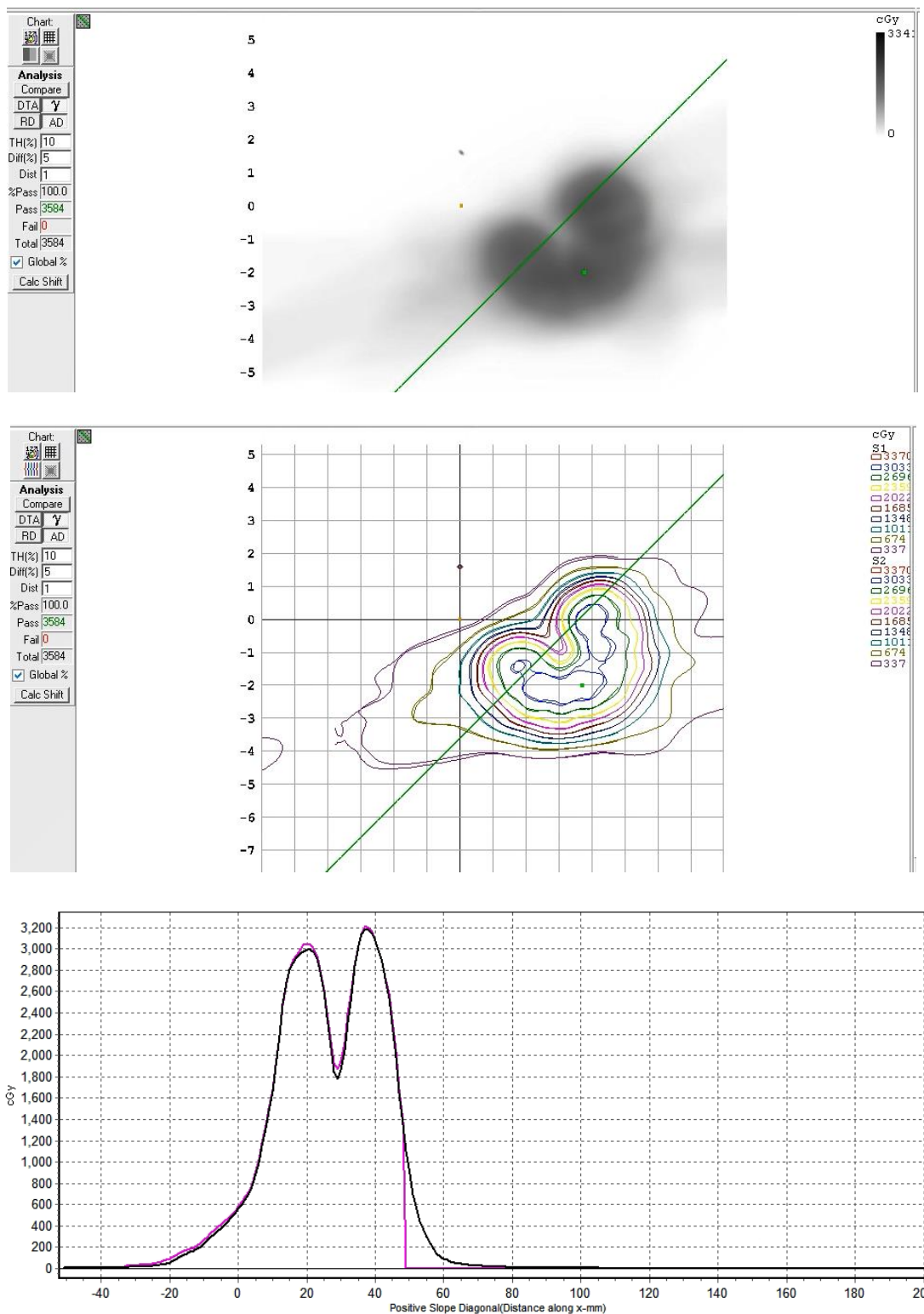


Figure 3.17 An example of a good pass (PTV1 BC plane CyberKnife dynamic). Top: gamma map overlay (5%/1mm global criterion applied); Middle: isodose overlay; Bottom: 1D profile overlay (black calculated dose, purple measured dose)

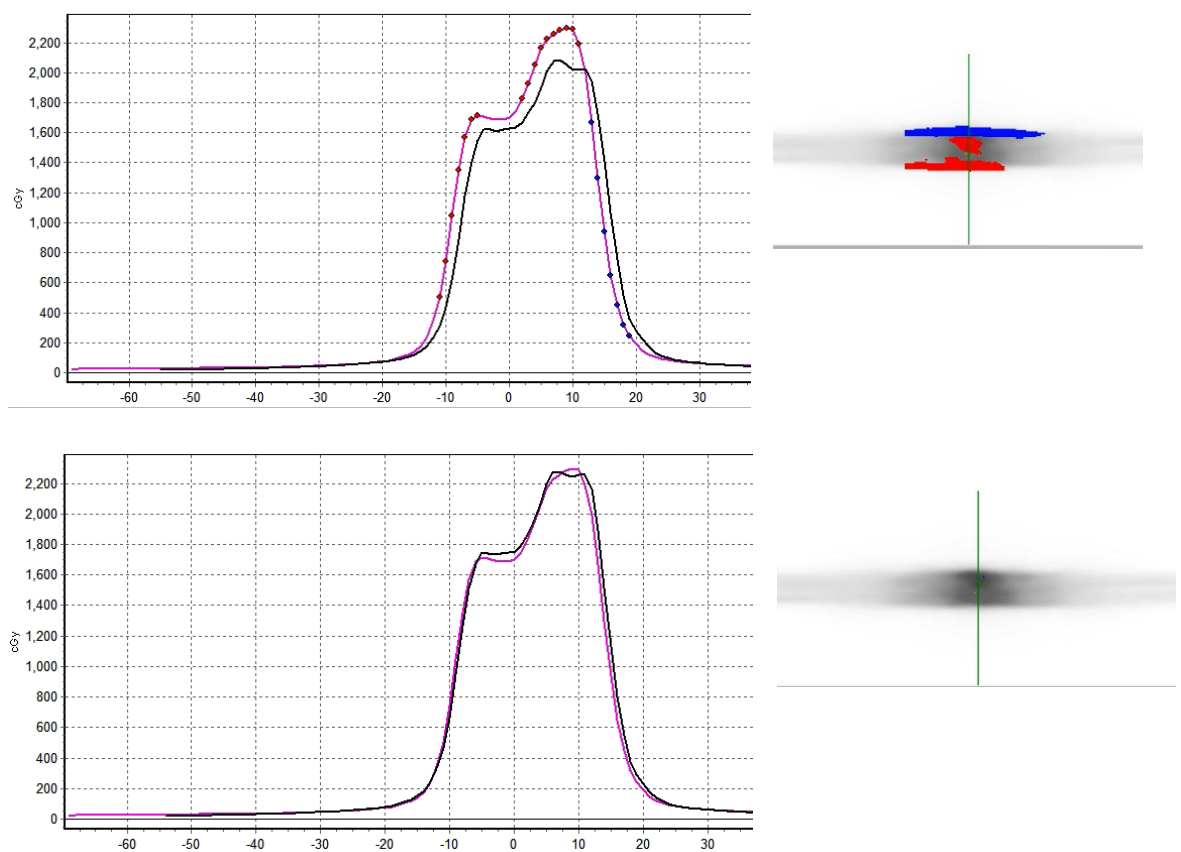


Figure 3.18 An example of a poor initial pass (PTV 4 AB plane Truebeam dynamic):

Craniocaudal profiles displayed. Top prior to spatial correction; bottom following spatial corrections of 1 mm in craniocaudal and out-of-plane directions. Black line is calculated dose, purple line is measured dose. Blue indicates measured dose lower than calculated, red indicates measured dose higher than calculated, gamma criterion 5%/1mm applied

Tables 3.8 – 3.11 provide full results of the delivery accuracies per technique including the spatial corrections in all three dimensions required to improve gamma test pass rates and mean planar dose differences in the high dose area following small spatial correction. The data also details the out-of-plane dose gradients and the maximum planned dose in the plane of interest to provide some context for the gamma test result. The following legend applies to all analysis metrics employed throughout this section to aid interpretation.

Gamma pass rate	Out-of-plane dose gradient	In-plane dose maximum	Corrections required
> 95%	<2.5%/mm	> 25 Gy	< 1 mm
85 - 95%	2.5-5%/mm	15-25 Gy	1 mm
< 85%	> 5%/mm	< 15 Gy	> 1 mm

Analysis metric // plane		PTV1 AB	PTV1 BC	PTV2 AB	PTV2 BC	PTV3 AB	PTV3 BC	PTV4 AB	PTV4 BC
Global Gamma pass rate	5%/1mm	87.6	80.9	98.2	88.6	90.0	74.0	96.9	92.4
	3%/2mm	94.0	96.5	99.5	99.9	96.4	76.8	99.4	97.8
Local Gamma pass rate	5%/1mm	57.1	53.6	80.3	65.5	54.2	47.6	56.5	65.9
	3%/2mm	83.9	88.9	95.7	95.5	85.4	68.3	86.1	89.6
Out-of-plane dose gradient (%/mm)		10.7	0.4	2.8	0.8	0.7	7.3	4.8	0.5
Maximum planned dose in-plane (Gy)		13.5	33	31.5	34	34.9	18.7	26	34
Geometric corrections required	transverse direction	0	1	0	1	0	1	0	1
	craniocaudal direction	-1	-1	0	0	-1	0	-1	0
	out-of-plane direction	0	0	0	0	-1	-1	0	0
Global Gamma pass rate	5%/1mm with corrections above	96.8	97.0	98.8	100	99.7	95.9	99.8	98.3
Mean dose difference, following spatial correction (%)		-3.0	2.0	-2.0	-1.3	1.7	-3.1	-1.2	3.9
SD dose difference (%)		3.7	1.9	2.0	1.8	2.5	3.7	1.6	1.4

Table 3.8 CyberKnife static summary data. Note that a maximum of 1 mm spatial correction is required in all directions

Analysis metric // plane		PTV1 AB	PTV1 BC	PTV2 AB	PTV2 BC	PTV3 AB	PTV3 BC	PTV4 AB	PTV4 BC
Global Gamma pass rate	5%/1mm	90.9	100.0	97.8	99.9	99.5	48.1	84.2	86.5
	3%/2mm	89.2	100.0	98.3	100.0	97.9	77.6	98.8	96.8
Local Gamma pass rate	5%/1mm	60.7	95.7	70.2	92.7	74.8	45.3	50.1	54.8
	3%/2mm	79.3	95.8	86.5	99.0	89.0	74.7	78.4	90.9
Out-of-plane dose gradient (%/mm)		10.7	0.4	2.8	0.8	0.7	7.3	4.8	0.5
Maximum planned dose in-plane (Gy)		13.5	33.0	31.5	34	35	18.7	26.0	34
Geometric corrections required	transverse direction	0	0	0	0	0	1	0	1
	craniocaudal direction	0	0	0	0	0	-1	-1	0
	out-of-plane direction	0	0	0	0	0	1	-1	0
5%/1mm global gamma test pass rate, following spatial correction		90.9	100.0	97.8	99.3	99.5	91.0	99.7	97.7
Mean dose difference, following spatial correction (%)		4.0	-1.5	-2.9	-1.5	1.5	-3.2	2.3	-2.9
SD dose difference (%)		4.6	1.8	2.6	1.8	1.8	2.7	2.3	2.2

Table 3.9 CyberKnife respiratory-tracked summary data. Note that a maximum of 1 mm spatial correction is required in all directions

Analysis metric // plane		PTV1 AB	PTV1 BC	PTV2 AB	PTV2 BC	PTV3 AB	PTV3 BC	PTV4 AB	PTV4 BC
Global Gamma pass rate	5%/1mm	96.4	84.9	87.8	86.4	99.2	50.6	71.8	82.4
	3%/2mm	98.7	96.6	95.9	93.9	99.7	81.4	93.5	91.2
Local Gamma pass rate	5%/1mm	69.9	63.2	56.7	62.3	86.9	50.2	59.5	52.5
	3%/2mm	83.5	93.9	56.8	87.5	99.2	80.4	91.4	79.9
Out-of-plane dose gradient (%/mm)		6.2	0.5	3.4	0.8	0.3	5.2	6.2	0.3
Maximum planned dose in-plane (Gy)		14.4	34	32.1	34.5	34.1	17.5	25.3	32.5
Geometric corrections required	transverse direction	0	1	0	-1	0	-1	0	-1
	craniocaudal direction	0	1	1	0	0	1	1	0
	out-of-plane direction	0	0	-1	0	0	-1	-1	0
5%/1mm global gamma test pass rate, following spatial correction		96.4	99.8	98.2	97.0	99.2	98.6	100	99.2
Mean dose difference, following spatial correction (%)		-2.3	-2.4	-3.3	-3.0	-2.6	-2.4	-0.9	-2.9
SD dose difference (%)		1.4	1.2	1.3	2.7	2.5	0.8	0.9	2.1

Table 3.10 Varian Truebeam static summary data. Note that a maximum of 1 mm spatial correction is required in all directions

Analysis metric // plane		PTV1 AB	PTV1 BC	PTV2 AB	PTV2 BC	PTV3 AB	PTV3 BC	PTV4 AB	PTV4 BC
Global Gamma pass rate	5%/1mm	88.8	96.1	88.0	80.0	85.1	84.6	63.0	84.6
	3%/2mm	99.7	97.3	96.7	96.5	99.6	95.2	88.5	94.5
Local Gamma pass rate	5%/1mm	67.6	95.2	48.1	57.2	92.6	45.7	39.8	72.0
	3%/2mm	93.4	96.7	89.6	89.0	98.9	71.6	81.9	94.2
Out-of-plane dose gradient (%/mm)		3.1	0.5	3.2	0.5	0.3	4.9	6.0	0.2
Maximum planned dose in-plane (Gy)		14.6	34.6	31.5	33.1	32.7	16.3	25.7	32.0
Geometric corrections required	transverse direction	0	0	0	-1	-1	-1	0	0
	craniocaudal direction	-1	1	1	1	1	1	1	1
	out-of-plane direction	0	0	1	0	1	0	1	0
5%/1mm global gamma test pass rate, following spatial correction		99.5	99.3	100	98.4	99.9	99.4	100.0	100.0
Mean dose difference, following spatial correction (%)		-1.8	-1.9	-1.1	-1.6	-2.3	-1.4	-2.5	-2.4
SD dose difference (%)		1.5	1.8	1.1	2.1	2.0	0.9	2.0	1.1

Table 3.11 Truebeam respiratory-gated summary results. Note that a maximum of 1 mm spatial correction is required in all directions

End-to-end repeatability results are illustrated in table 3.12, shown for PTV1 plan delivered on the Truebeam platform multiple times in static mode. Note the low levels of variability exhibited in 5%/1mm gamma pass rate results, namely an inter-quartile of 3.2% prior to spatial correction reducing to 2.0% post spatial correction. Note also the maximum spatial correction of 1 mm, which is reflective of the results throughout this study.

Analysis metric // plane		original AB	original BC	repeat 1 AB	repeat 1 BC	repeat 2 AB	repeat 2 BC	repeat 3 AB	repeat 3 BC	median AB	median BC
Global Gamma pass rate	5%/1mm	96.4	84.9	100	91.5	94.5	86	98.1	93.4	98.1	91.5
Geometric corrections required	transverse direction	0	1	0	1	0	1	1	1	0	1
	craniocaudal direction	0	1	0	0	1	0	-1	0	0	0
	out-of-plane direction	0	0	0	0	0	0	0	0	0	0
5%/1mm global gamma test pass rate, following spatial correction		96.4	99.8	100	99.8	99.2	97.4	99	100.0	99.2	99.8

Table 3.12 Truebeam PTV1 end-to-end reproducibility results. Note that a maximum of 1 mm spatial correction is required in all directions and the very small range of 5%/1mm gamma pass rate results between the repeated measurements after spatial correction is applied

The global 5%/1mm gamma test pass rates as illustrated in tables are displayed graphically to aid interpretation in figures 3.19 and 3.20.

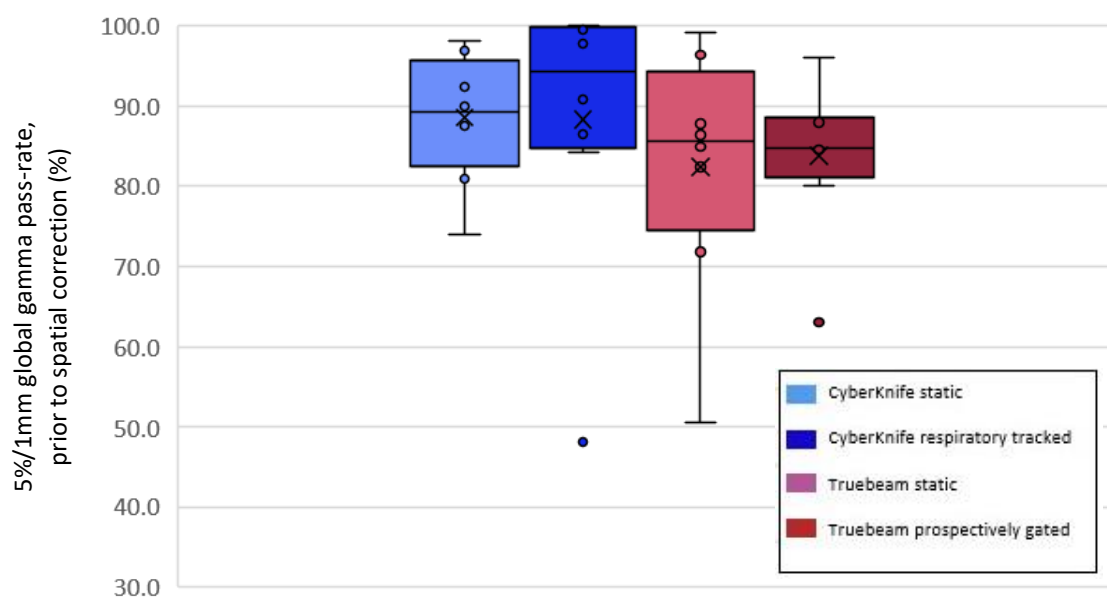


Figure 3.19 Box and whisker plot 5%/1mm gamma pass-rates prior to spatial correction. Note the low median pass rate (87.7%) and high variability for all delivery techniques

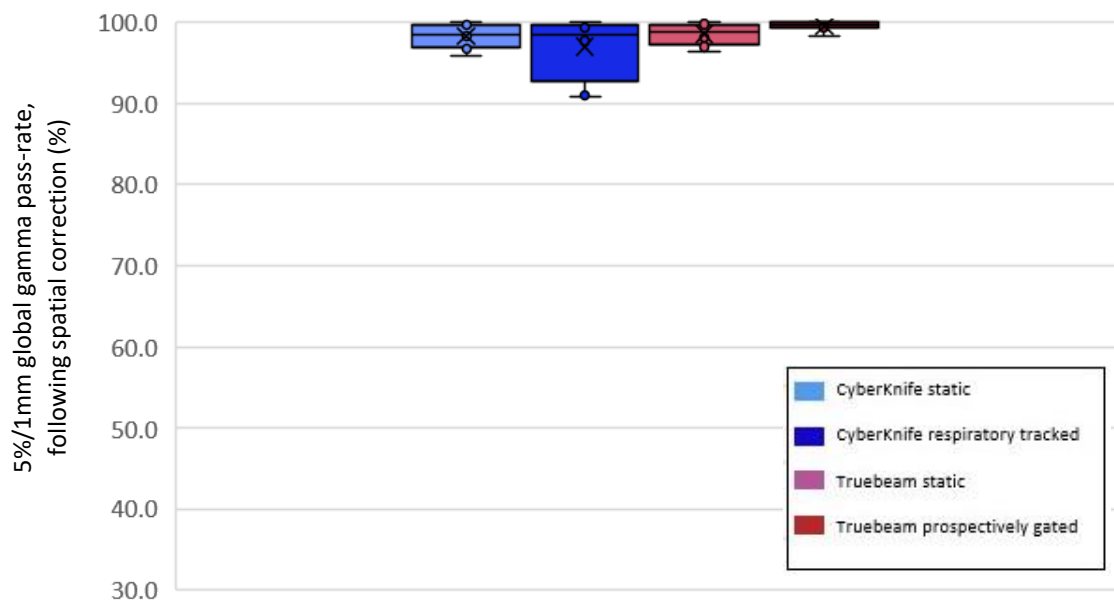


Figure 3.20 Box and whisker plot of 5%/1mm gamma pass-rates following applied spatial corrections. Note the resulting improvement in gamma pass rates (median 99.3%) and significant reduction in variability for each delivery technique

The spatial corrections required to achieve the high gamma pass rates in figure 3.20 are shown in the histograms figures 3.21 – 3.23. This was used to examine the spatial error distribution between techniques and to illuminate any outliers.

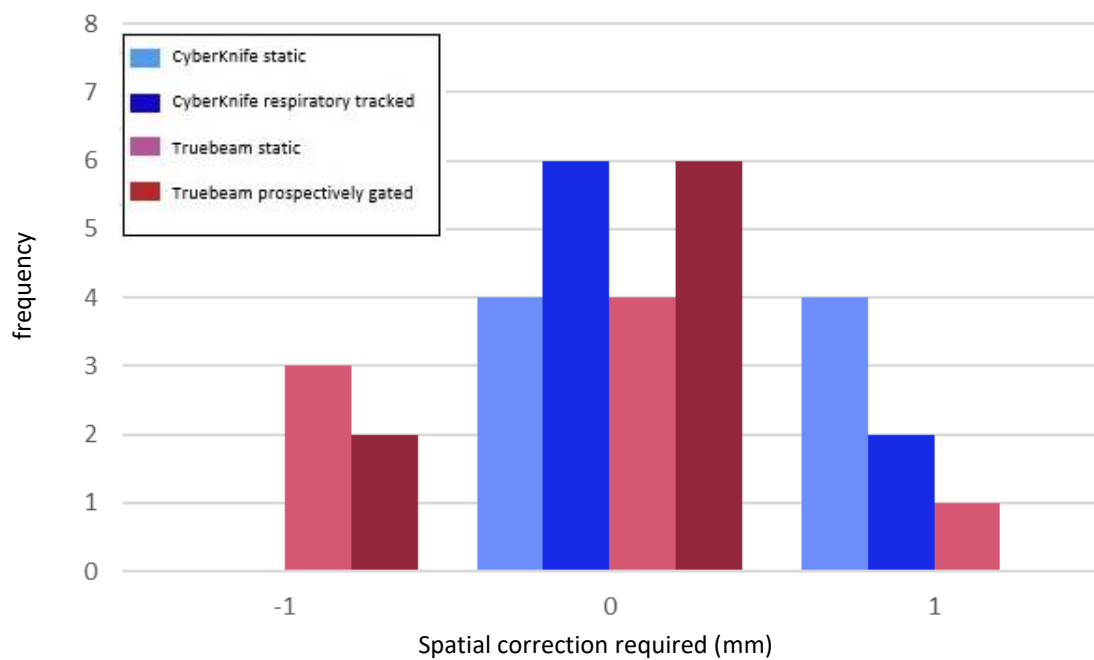


Figure 3.21 Histogram detailing corrections required in transverse direction. Note the maximum correction of 1 mm. Median for each group within 0.5 mm

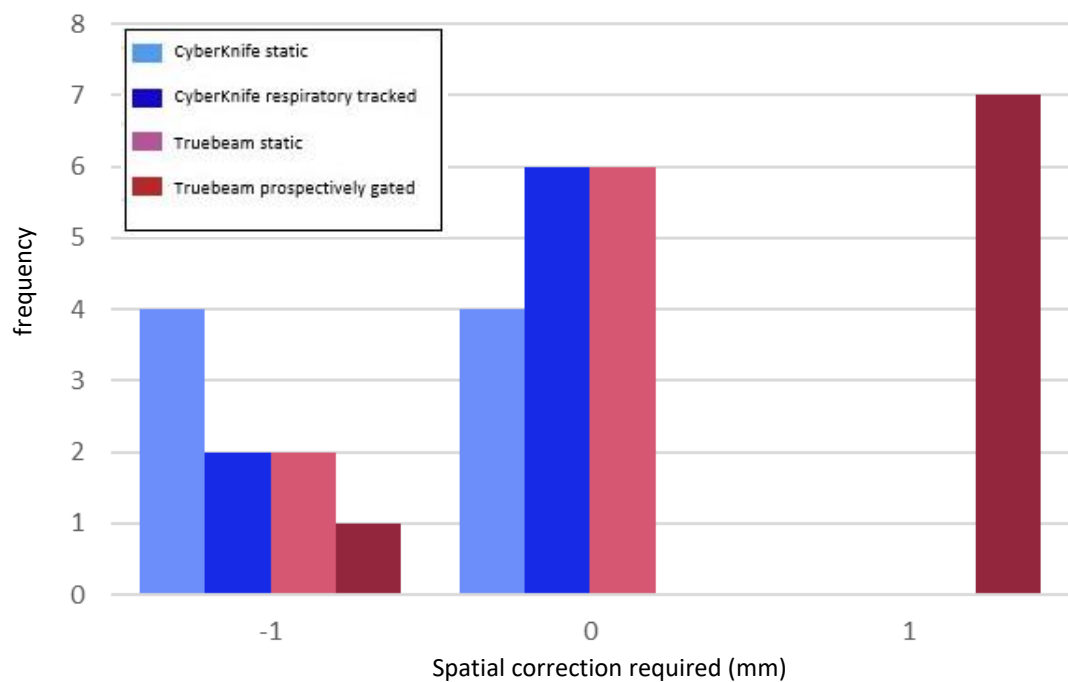


Figure 3.22 Histogram detailing corrections required in craniocaudal direction. Note the maximum correction of 1 mm. Median for each group within 0.5 mm, excepting Truebeam dynamic data which indicates skew towards the positive craniocaudal direction with a median correction required of +1 mm

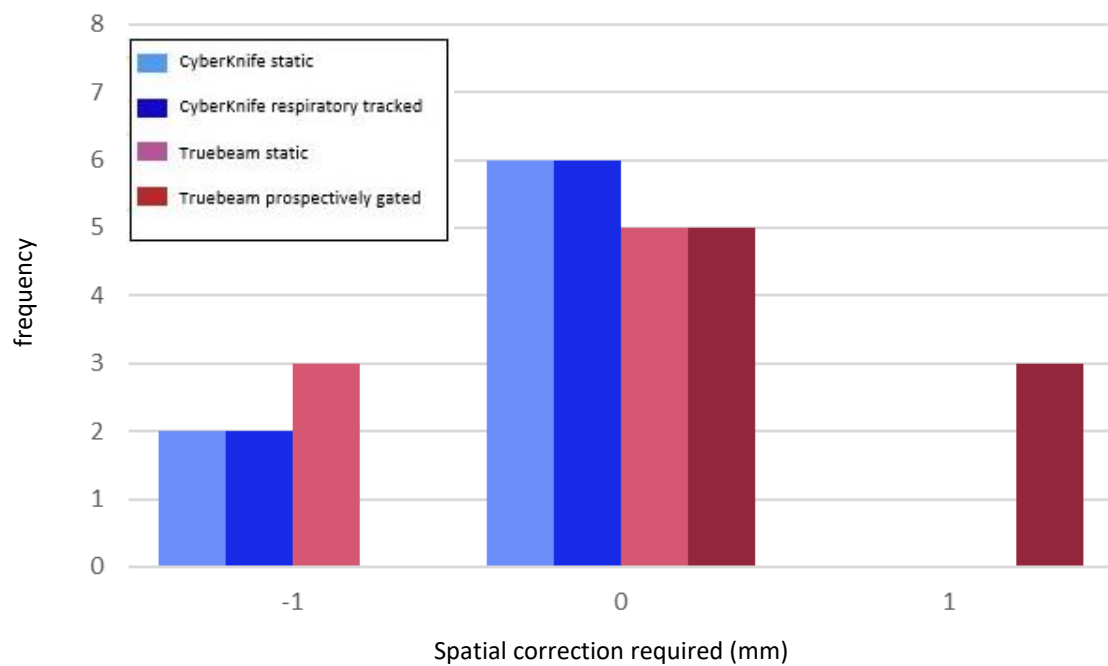


Figure 3.23. Histogram detailing corrections required in the out-of-plane direction. Note the closely grouped data in absolute terms. Median for each group within 0.5 mm

Mean dose differences in the high dose regions are displayed in figure 3.24.

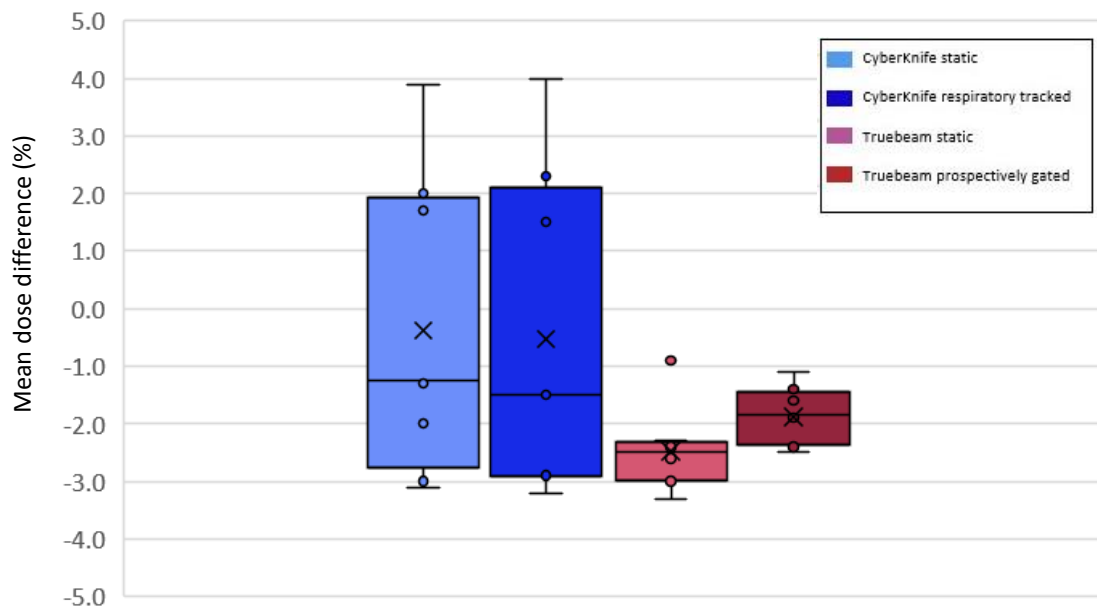


Figure 3.24 Mean dose differences between measured and calculated dose for doses above prescription dose (or above 80% of planar maximum dose) following small spatial corrections

Note that all median delivered doses are within 2.5% of calculated dose, but the Varian data is much more closely grouped.

The association of the improvement in 5%/1mm gamma pass rates as a result of spatial correction with out-of-plane gradients is illustrated in figure 3.25 indicating the sensitivity of 2D gamma analysis using this metric to small corrections.

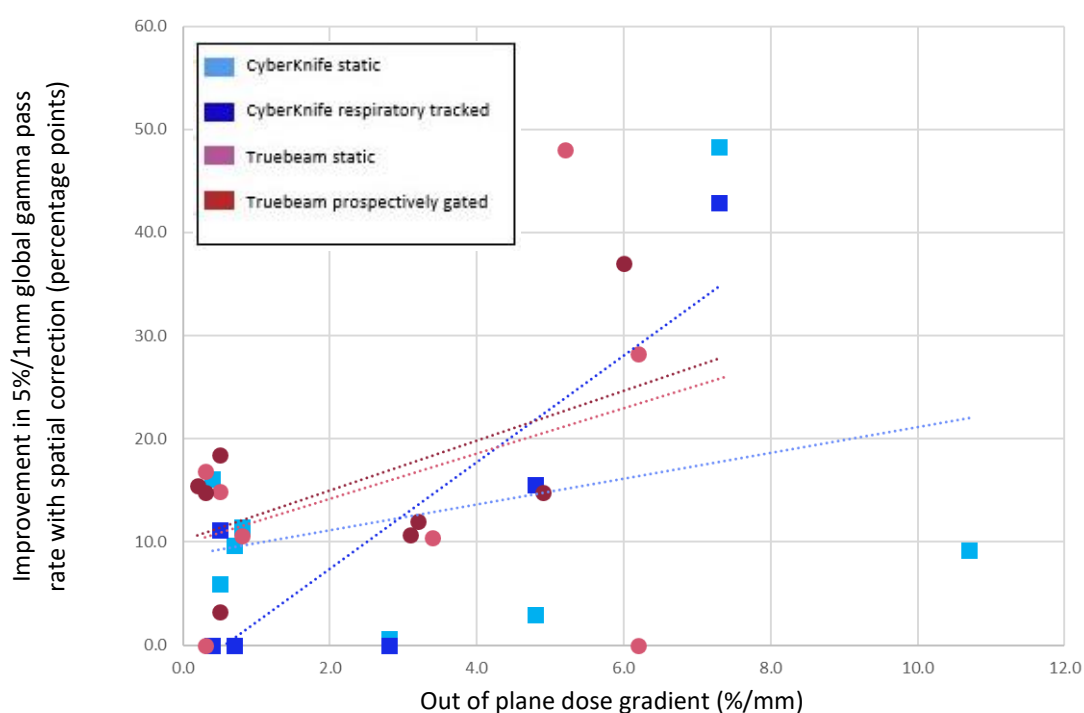


Figure 3.25 Improvement in 5%/1mm global gamma pass rate as a result of small spatial corrections as a function of out-of-plane dose gradient. Indicates a signal for sensitivity.

Linear trendlines

The two cases following spatial correction that failed to achieve >95% pass rate at 5%/1mm are investigated here. PTV1 AB for the CyberKnife static delivery is illustrated below. The global 5%/1mm pass rate was 90.9%.

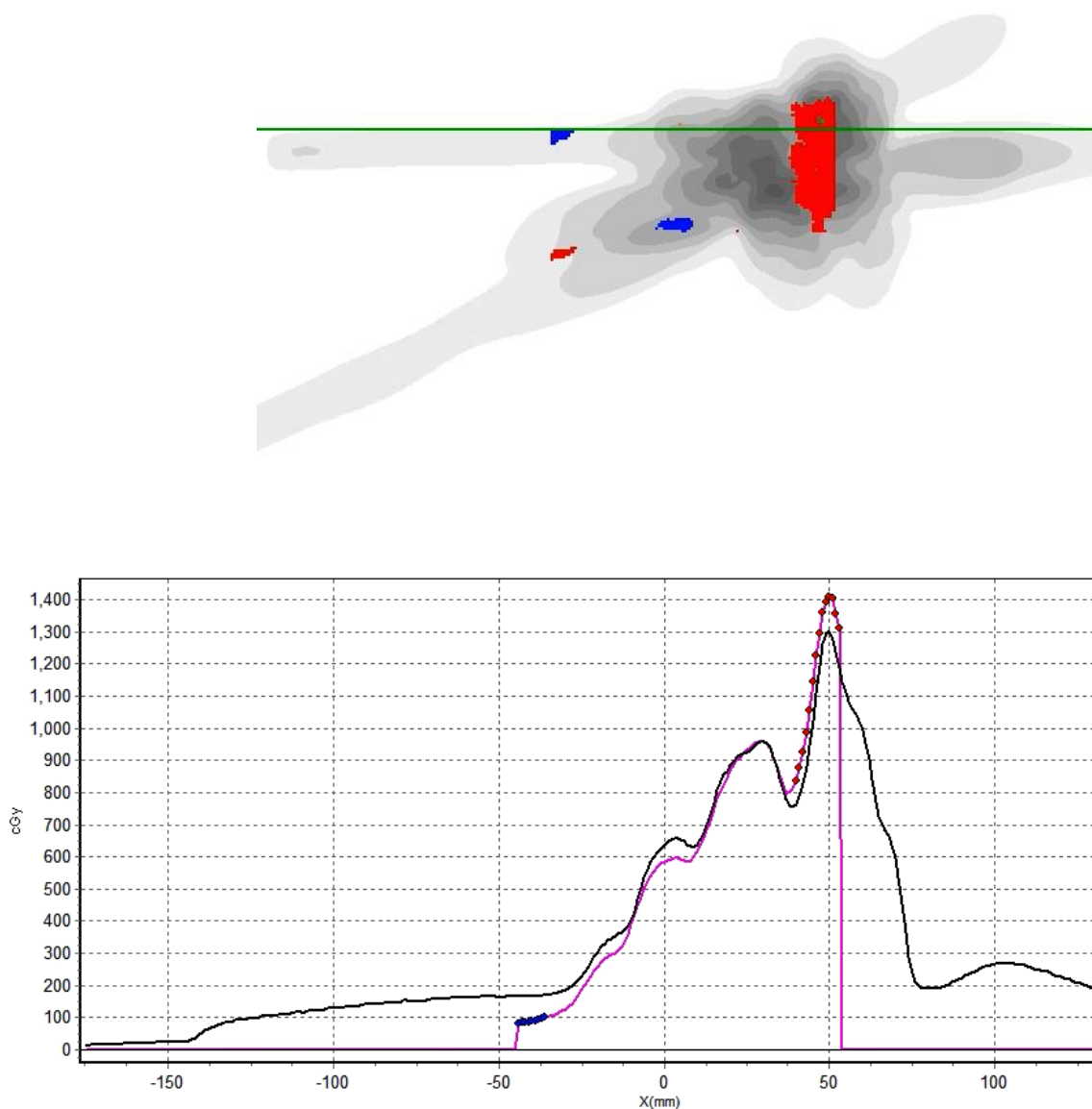


Figure 3.26 Apparent dose magnitude error for PTV1 AB plane CyberKnife dynamic delivery that did not diminish with simple spatial correction. Top: 5%/1mm gamma map, bottom: 1D left-right profile. Red indicates measured dose higher than calculated, blue dots indicate measured dose lower than calculated. Note how the dose difference appears to be a function of position on the left-right axis

Note the high measured dose for the positive X direction (patient left) and the low measured dose for the negative X direction (patient right).

The other outlier in this respect is the PTV3 BC plane where the post-correction results are illustrated below. A similar effect is seen here with a differential of dose similarity in the transverse direction.

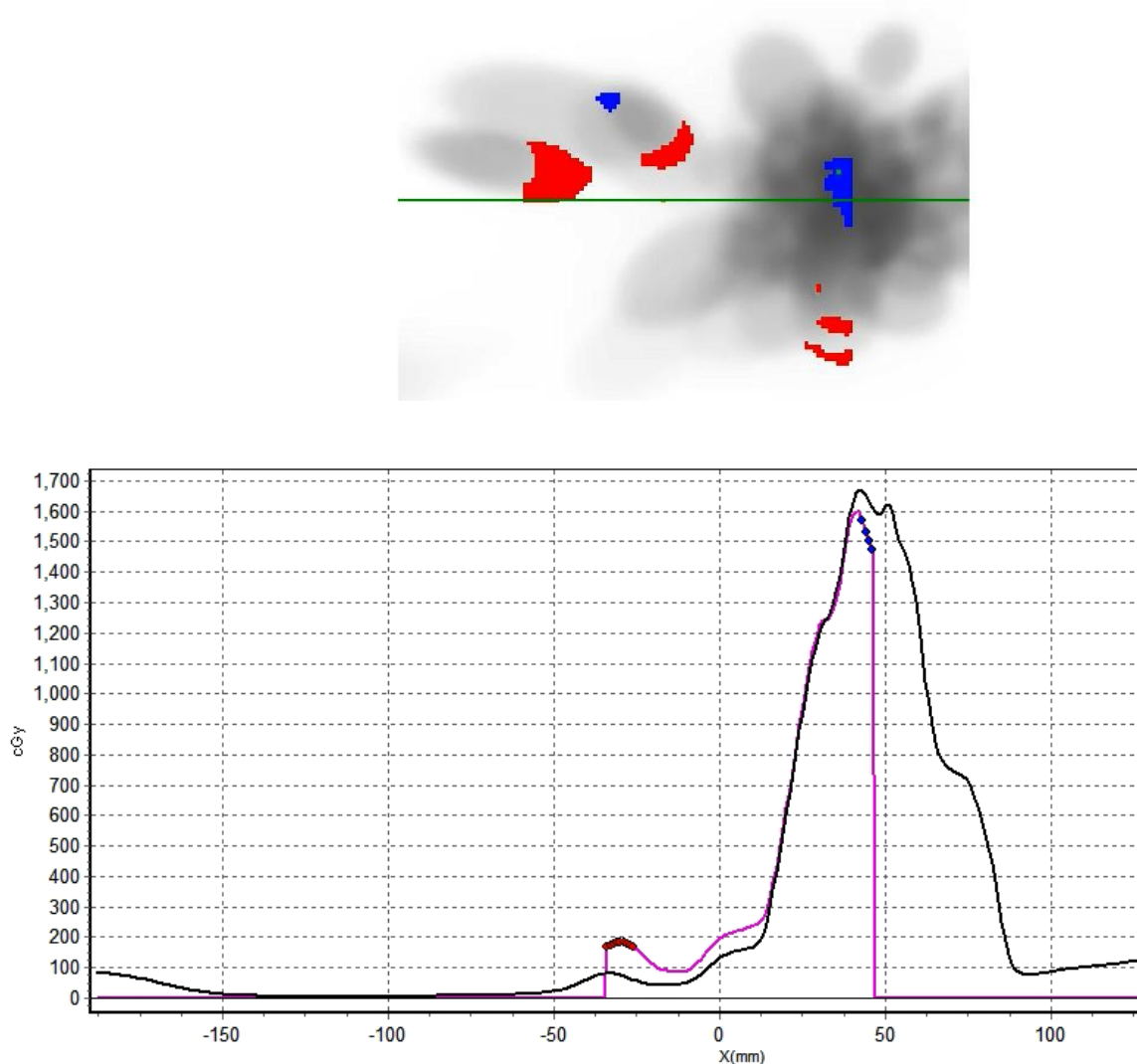


Figure 3.27 Apparent dose magnitude error for PTV3 BC plane CyberKnife dynamic delivery that did not diminish with simple spatial correction. Top: 5%/1mm gamma map, bottom: 1D profile. Note how the dose difference appears to be a function of position on the left-right axis

Chapter 4: Discussion

4.1 Phantom design and fabrication critique

Although the materials used to produce the phantom insert used in this study did not meet the ideal criteria set out in terms of their radiation properties, the selected materials proved to be reasonable analogues in terms of optimising for both imaging contrast requirements for kV CT and kV cone-beam CT and to reasonably mimic human tissues in terms of treatment beam characteristics. A truly comprehensive exhaustive search for the most optimal print materials was not possible due to the lack of published specifications for radiation characteristics meaning that it became impractical to measure properties of a wide range of 3D print materials using CT analysis. It is recognised that the increased relative electron density of both materials will lead to a small increase in radiological path length compared with the anatomical environment, however this would be negligible given the small physical distances involved. Steps were undertaken to reduce the likelihood of dose perturbation close to the dose measurement planes that would reduce the reliability and applicability of results; specifically, unwanted air gaps were minimised in the 3D phantom design, high density materials were not used to co-locate the modular elements or to define the geometric origin of the dose planes in the final assembly. Instead, the 3D print materials themselves were used for co-location of the module parts and small grooves in the 3D printed model were used to define the planar origins in object and imaging space. The measured film plane origins were easily identifiable on 3DCT and 4DCT imaging using the grooves in the phantom, even in the presence of 10 mm of peak-to-

trough motion using a near-expiration reference phase, narrow temporal binning and windowing.

The production of samples and prototypes was necessary to ensure that appropriate materials were selected, and that the 3D model was printable without modelling errors at a level of morphological quality that reflected cardiac anatomy, and that image contrast was sufficient. This iterative process was time-consuming but ultimately instructive in identifying model limitations and therefore improving the final model quality.

The phantom motion employed in this study was simple periodic craniocaudal motion which typically reflects the largest respiratory magnitude seen anatomically in the thorax (Sceheter, Resar & McVeigh, 2006). The magnitude of the simulated motion reflects the largest motion that is likely to be seen for the SABR technique before motion reduction or management techniques are employed (UK SABR Consortium guidance v6.1). This magnitude was also chosen to increase the sensitivity to respiratory tracking or gating delivery errors with conservative distance-to-agreement metrics pertinent to the quality assessment of SABR plans. Although only 1D motion was used in this research, the cylindrical design of the phantom insert coupled with coaxial positioning of the motion actuator allows for the addition of rotation to the insert, effectively enabling future additional simulation of motion in the transaxial plane, thus making the phantom motion 3D in nature.

Cardiac motion was specifically not within the scope of this work given time constraints and the current inability of treatment systems to gate or track using a cardiac motion trigger. In fact, the largest clinical trial to assess the efficacy and safety

of cardiac SABR in VT patients did not attempt to consider or characterise cardiac motion but instead accounted only for respiratory motion with a full ITV method to ensure target coverage was maintained within the prescription dose. This work whilst going a step further in terms of motion compensation than the seminal clinical trial in examining respiratory motion compensation, also allows for future extension to examine the effects of cardiac motion on end-to-end dose delivery accuracy using modified CIRS phantom motion files that contain additional cardiac motion, albeit in a rigid fashion.

Two planes of interest were selected in this phantom configuration that were optimised to allow for adequate dosimetric assessment of target coverage for the main current clinical indication of VT but also for the potential indication of HOCM and also to allow assessment of doses to potential organs at risk. Using a fully 3D printed design as advocated in this work, it would be possible to add planes or change the planes in the 3D model relatively easily. However, the planes used in this study were found to be both reasonable for the targets studied but also a practicable number balancing phantom fabrication complexity with maximising dosimetric characterisation.

As acknowledged in section 2.1.2, the cardiac modular component was downscaled in all three dimensions by a factor of 25% in order that the cardiac components were of the same scale as the thoracic phantom but also to maintain anatomical accuracy of as much as possible for the position of the heart within the mediastinum. The impact of this on the applicability of the dosimetric results is likely to be minimal. First, all components were scaled by the same degree for internal consistency. Second, for context, it is important to recognise that there is a significant degree of heart size

variation in the normal population, as reported by Pfaffenberger et. al. (2013). These authors found significant differences in 2-D measurements of the heart using echocardiography that were correlated with sex, BMI and age, with the largest difference being more than 30% variation in left ventricular end-diastole diameter.

As a result of this variation due to non-cardiac prognostic factors in addition to the wide variation in target shape due to pathological aetiology, it is unrealistic to be able to account for all shapes and sizes of target in this dosimetric validation research. A range of target shapes were chosen to represent varying degrees of target complexity (three VT circuits and one HOCM pathology) and what is acknowledged is that it is more difficult to deliver well-modelled calculated patient dosimetry to smaller, more intricate targets. This is due to increased uncertainty in the definition of output factors for smaller aperture sizes that are more likely to be required to provide a conformal dose distribution to smaller and/or more intricate shapes using a finite resolution MLC leaf size (in the case of Varian Truebeam) or fixed circular collimator size (in the case of Accuray CyberKnife). In this case, due to the phantom heart analogue being geometrically down-scaled compared with the single original anatomical source, it is likely that the dosimetric complexity examined here is at least as complex as the average case, taking in to account the relative magnitudes of the down-scaling factor and the normal anatomical variation.

4.2 Interpretation of dosimetric verification results

Tables 3.8 – 3.11 show the results of gamma tests at 5%/1mm and 3%/2mm for the range of plans and treatment techniques. These data indicate that the measure of plan delivery accuracy is dependent on the criterion used. As expected, global pass rates (where the dose difference metric examines all dose values using a fixed dose difference as a percentage of the maximum dose to points within threshold) were universally higher than local pass rates (where the dose difference applies as a percentage of each dose value within the threshold). It was also noted that 3%/2mm pass rates were almost universally higher than 5%/1mm pass rates. This indicated that small positional differences between calculated and delivered dose were a more frequent cause of failure than dose difference.

Although there were numerical improvements when moving to a 3%/2mm index, there remained a significant number of results that would be considered to be lower than acceptable using this criterion. This indicated that a closer examination of dose similarity beyond the use of the quantitative gamma metric was warranted to attempt to determine the cause of the dose dissimilarity. Therefore, visual assessment of in-plane 2D isodose overlay and multiple 1D profile assessments were performed in the plane of the films (transverse and craniocaudal directions) to probe the causes of the dose dissimilarity. Spatial corrections were tested in an attempt to improve the global 5%/1mm gamma test result to above 95% which would inform the degree of in-plane spatial misalignment. The required spatial corrections are displayed in histogram format in figures 3.21 (transverse correction) and 3.22 (craniocaudal correction),

indicating that maximum spatial discrepancies of 1 mm were present throughout the delivery techniques and platforms, which is impressive.

The employment of 2D dose measurement methodology exhibits limitations for interpretation of 3D dose distributions, especially in the presence of high dose gradients perpendicular to the plane of measurement. This is illustrated in figure 3.25 where (although there is variability in the data) there exists a signal for association between potential planar dose similarity improvement and the magnitude of out-of-plane doses. Rather than attempting to mitigate for the effect of out-of-plane dose gradients by measurement of multiple dose planes parallel and close to the reference plane which would be impractical, an alternative method was used. This method extended the 2D analysis by also comparing the measured dose plane with calculated dose in planes parallel to the reference plane in 1 mm increments from the reference plane. This method was used similarly to the in-plane method to quantify the spatial corrections required to bring about improvement in dose similarity.

When the out-of-plane spatial corrections applied were analysed, the magnitude of the required corrections (figure 3.23) was found to be similar to those seen in-plane, namely maximum corrections of 1 mm with a median of approximately 0.5 mm.

Following spatial corrections applied in up to three directions required to improve positional similarity, the 5%/1mm global gamma test was re-employed to test the level of dose similarity following these small spatial corrections. These results (figures 3.19 and 3.20) indicate significant improvement in 5%/1mm global gamma pass rate from a median of 87.7% prior to spatial correction to a median of 99.3% (with all individual planar results better than 90%) following spatial correction. Also, critically the

variability in the data was considerably reduced which indicates high levels of sensitivity to very small positional uncertainties. There was no indication of broadening of dose gradients or additional uncertainty in the position of high dose gradients when using the respiratory tracking or gating techniques compared with the static baseline results.

Although this is the first known study to assess cardiac SABR delivered dose accuracy, there is value in setting these results in the context of those from the large recent UK National SRS dose audit by Dimitriadis et. al (2020). This audit examined the calculated vs measured dose accuracy from 33 intracranial treatment plans for a range of treatment techniques including VMAT, CyberKnife and GammaKnife. The fractional prescription doses were also similar to this research (16-21 Gy SRS vs 25 Gy cardiac SABR) and the dosimeter of choice for determination of dose gradient and positional accuracy was EBT-XD film with the radiochromic film analysis methodology largely reflecting the methodology used in this research, including a two-dose point linear scaling method to mitigate for post-exposure film blackening and variations in scanner response and choice of gamma criterion. Interestingly the authors also allowed up to 1 mm geometric adjustment to optimise the final published gamma pass rates.

The SRS audit results demonstrate a gamma pass rate median and spread of results very similar to the cardiac SABR results. Using a global 5%/1mm criterion (threshold 2 Gy due to the user freedom in setting prescription dose values) to compare calculated vs measured doses, all except three films in the audit showed a greater than 90% pass rate with median pass rates between 98.3% and 99.3% depending on platform, but with no statistical difference detected between platforms (alpha 0.05). This is highly

reflective of the results achieved in this research which revealed a median pass rate of 99.3% (following the allowable 1 mm spatial corrections) and no observable difference between platforms. Although the authors of the SRS audit did not publish the geometrically uncorrected results which would have been useful for establishing if the sensitivity of the plan to spatial set up / co-registration accuracy, that notwithstanding it is encouraging that for a similar plan objectives very similar high dosimetric quality is achieved; the national audit is also supportive of the approach taken in this research to acknowledge and allow mitigation for small spatial co-registration set up inaccuracies of the order 0 – 1 mm that are difficult to detect and correct for in practice, even with the highest levels of film fixing and origin identification.

In addition to examining spatial errors, dose magnitude differences between calculated and measured were also examined using the high-dose regions of each film. This was necessary to detect any systematic dose magnitude errors between treatment planning and delivery, results are illustrated in figure 3.24. Although data indicates a degree of variation for both platforms, increased variation was demonstrated for CyberKnife with an interquartile range of the order 4.5 %, however this range crossed zero dose difference with a median delivered dose within 1.5% of calculated. Varian Truebeam results revealed less variation (interquartile range of up to 0.7%) within its platform but signalled a potential for systematic delivered dose reduction compared with calculated, however the median dose difference remained better than 2.5%. These apparent dose similarities should be viewed in the context of an estimated measurement method uncertainty of 2.2% (section 3.2.4) and so it is

highly likely that there is no meaningful dose difference that calculated and delivered for either treatment platform examined.

There was no indication of a systematic degradation in absolute dose accuracy for the high dose region when using respiratory management techniques compared with the static delivery counterparts.

Overall, when seen in the context of the estimated overall uncertainty in the dose measurement methodology using radiochromic film alone, the dosimetric validation results show a very high degree of similarity between calculated and delivered doses, reflecting well-modelled treatment beams in each treatment planning system accompanied by equivalently high accuracy modelling of MLC transmission and the dosimetric leaf gap for the Varian VMAT technique. The high degree of dosimetric accuracy also indicates that the VMAT planning class solution of 4 arcs to deliver 25 Gy in a single fraction meant that plans were not overly modulated to an extent that affected their deliverability in a clinically significant way.

Although almost all spatial discrepancies were explainable with a simple small translational correction, there were two outliers that warranted further investigation. These were PTV1 CyberKnife dynamic (AB plane) and PTV 3 CyberKnife dynamic (BC plane), figures 3.26 and 3.27 respectively. Notably these cases both resulted from CyberKnife deliveries and also notable is that the measured dose planes were in the lower dose regions away from the cardiac target in the presence of significant out-of-plane dose gradients. In both of these cases, there is a differential of dose similarity across the patient transverse direction observable in the figures. Although these two

cases were also the cases with the highest out of plane dose gradients, a simple out-of-plane translational spatial correction was not able to resolve the differences between the calculated and measured doses. Furthermore, in both cases the dose difference is not systematic across the measurement plane and so can also not be explained by a simple calibration error alone.

The main hypothesis for the cause is that the cardiac insert exhibited a small amount of roll compared with the planned position as the cardiac insert was not locked for roll with respect to the outer thorax phantom in this design. A small amount of roll amounting to 1 - 2 mm at the cardiac insert intersection with the thorax phantom might have gone undetected visually on the phantom during the set-up stage but would lead to differential out of plane dosimetric errors of the order or magnitude seen in the presence of high out-of-plane dose gradients. Interestingly, cardiac insert roll rotation of this order was indeed detected by CBCT on multiple occasions for the Truebeam platform, and was subsequently corrected prior to proceeding to treatment. This indicates that this magnitude error was possible to go unnoticed by eye. Following CyberKnife localisation using the spinal anatomy, only 2 ICD electrodes were able to be used for final translational corrections to the cardiac insert due to reported high uncertainty from automatic detection of the third ICD electrode in the stereoscopic images. As a result of only 2 electrodes being usable, rotation detection with respect to the outer thorax phantom was not detectable by the system.

This degree of uncorrected roll rotation in the presence of high dose gradients would manifest itself in the measured dose appearing higher than expected for one lateral

side of the phantom where the plane is closer to the target and lower than planned on the other where the plane is further from the target.

The other film present in the same treatment delivery that bisected the high dose target in each case was subject to a very low gradient perpendicular to the measurement plane ($< 1\%/mm$). This meant that the sensitivity to a roll error there was significantly diminished and is corroborated by the very high gamma pass-rate for those films despite what would be an equivalent magnitude of roll rotation.

These apparent failures are useful in initiating interrogation and hypothesis generation but more importantly illustrate the ability of this analysis method (and metrics employed) to detect very small potential spatial errors, including rotation. Overall though, following spatial corrections up to 1 mm in all directions, delivered dosimetry was extremely similar to calculated dosimetry indicating very accurate reproduction of calculated dose gradients and spatial targeting accuracy.

By examination of spatial corrections across the range of plans, a signal was detected that may indicate a slightly inferior positional accuracy in the craniocaudal correction from the Truebeam gated delivery (median discrepancy 1mm) when compared with the Truebeam static and CyberKnife tracked techniques (median discrepancies up to 0.5 mm). This was, on reflection, unsurprising given that that technique was subject to additional known spatial uncertainties, dominated by the use of a gating window of finite width (that allow for practical duty cycles of 50 or 70%), but also the determination of the reference temporal phase for treatment planning from 4DCT that is not infinitesimally small. Applying the gating windows to the 4DCT data revealed

phantom positional deviations of $\pm 1\text{mm}$ or $\pm 2\text{mm}$ for 50% or 70% duty cycles (respectively) with respect to the calculated phase plane in the craniocaudal direction.

Given these additional calculated phase uncertainties coupled with the prospectively gated 4D-CBCT acquisition of the phase of interest prior to treatment followed by the prospective gated delivery, a 1 mm systematic error is very low when considered in context of the contributory sources of potential positional error.

Importantly, there was no evidence detected of additional dose blurring detected in the plane of interest in the direction of the phantom motion that might be expected to manifest itself in broadening of the dosimetric penumbrae in that direction. This would likely be detected quantitatively by a reduction in the 5%/1mm gamma pass rate or qualitatively via profile overlay examination following any spatial correction.

Aside from the slight degradation in spatial positioning accuracy in the direction of motion for the Truebeam gated technique, there is very little indication that there is any other systematic offset in positional accuracy of a clinically meaningful magnitude between the two linac manufacturers. This is despite significant differences in the localisation methods between manufacturers. CBCT for the Truebeam technique provided sufficient image contrast between the myocardium, the blood pool and the extracardiac elements to facilitate 3D image co-registration with the reference CT. A relatively narrow image window width was used to optimise visualisation, followed by verification using the ICD electrode positions (with an accompanying broadening of the image window width to visualise the electrode without image 'flare'). This is reflective of the methodology that would be used for clinical treatment for this indication for Truebeam. Although there was a large amount of 3D data available to the user in

terms of the full tomographic image, there was an absence of quantitative metrics for co-registration on this platform and so localisation accuracy was essentially reliant on visual inspection of the co-registration alone. This is quite different to the CyberKnife platform where 2D stereoscopic kV imaging was used to co-register on-treatment imaging with reference imaging using the bony anatomy of the spine followed by ICD electrode positions. Despite the stereoscopic 2D nature of the CyberKnife localisation method, the spatial resolution in the plane of the kV image was higher than the 3D Varian system and there also were a number of on-treatment quantitative metrics available (described in section 2.4.1) that allowed for additional evaluation of co-registration error. In summary, although the localisation methods for each platform were very different and each had their different challenges, there was no clear overall superior method demonstrated by the spatial accuracy delivery results.

In terms of drawing comparisons between dose calculation algorithms, this is difficult due to the small number of data points and the overall high pass-rates following spatial correction. That said, investigation for significant deviation should be made using the static delivery data in order to exclude any confounding uncertainties potentially arising from motion compensation aspects. By comparing the static delivery results, there appears no evidence for a systematic difference in the spatially corrected 5%/1mm global gamma test results. The difference in median global 5%/1mm pass-rate between CyberKnife and Truebeam systems is less than 1 % (98.6% and 99.4%, respectively) accompanied by very low levels variation about each median which provides some indication as to the reliability of this small difference.

The degree of similarity between calculated and measured dose might have initially been expected to lower given the relative proximity of the left aspect of the cardiac boundary with the lower density lung analogue. This is especially true of the CyberKnife calculation algorithm which is of particularly low sophistication for regions of tissue inhomogeneity. The RayTracing algorithm is a look-up table system that is only able to model changes in photon fluence in the beam travel direction by means of modification of depth to radiological depth. It is not able to compensate for changes in lateral electron dose deposition as a result of inhomogeneity. The AAA algorithm, by comparison, employed in this work for Varian Truebeam deliveries is more sophisticated being a superposition (Type B) algorithm able to model 3D lateral changes in electron dose deposition in the presence of inhomogeneity. This algorithm would also be able to model re-build-up of dose at the lung-cardiac insert boundary relatively accurately whereas this would not be modelled at all in the RayTracing calculation.

Although the film positioning in this phantom was designed to be as close as possible to the left lateral boundary of the cardiac insert to inform the dose accuracy to the left ventricle, the film remains a finite distance (approximately 5 millimetres) from the lung boundary due to the mechanical requirements of the phantom to retain rigidity and due to film post-processing cropping to remove edge artefacts. Furthermore, the most significant differences in dose calculation would be seen where the radiation beam traverses the lung-cardiac insert boundary. However, due to the distance between the film and the lung boundary coupled with a significant proportion of the dose delivered to that boundary arising from beams that have traversed the cardiac insert from the

right lateral side, the relative proportion of dose at the boundary that is subject to relatively high uncertainty is diminished for both platforms and so this may also explain the small difference in dosimetric accuracy detected between algorithms at the measurement positions.

4.3 Measurement methodology critique

The use of EBT-3 film with single channel dosimetry is relatively contentious for the measurement of doses up to 35 Gy as was performed in this research. Of course, each dosimeter has its own inherent uncertainty. In this research, extreme care was taken to characterise and minimise the dominating film-based artefacts originating from the batch calibration curve, lateral dose scanning artefacts and measurement reproducibility. These potential measurement artefacts, when explored arithmetically, were calculated to contribute an overall relatively low level of uncertainty (namely 2.2%), especially when compared with the main pertinent overall uncertainty budget of 5% as part of the gamma criterion, but also in the context of clinically meaningful dose differences for stereotactic radiotherapy. The dose accuracy variability appeared higher for CyberKnife than for Truebeam which warrants some further investigation, but this is unlikely to be due to dosimeter-based sources given the low levels of variability seen for the Truebeam deliveries. This research indicates that EBT-3 film and single channel dosimetry should not be dismissed as a potential dosimeter of choice for measurement of cardiac SABR dosimetry, when compared with the results of Devic (2011) who also indicate an overall uncertainty of approximately 2% ($k=1$) using multi-channel dosimetry for an equally high dose range.

In terms of the method of dosimetric analysis, a large amount of manual intervention was necessary to post-process the radiochromic film files in this research which could lead to an unnecessary source of processing error. This meant that a high level of data checking was necessary in order to ensure data validity. Future expansion of this research would benefit from some degree of automation of these processes in order

to make the analysis more robust and to improve efficiency, especially if this was used in a large, centralised quality assurance programme.

For the preparation of the calculated dose files in to 2D planes, although the SNC Patient software was able to produce an extracted plane from the 3D dicom data, the co-ordinate convention and origin was reset during this software extraction process and so a high level of manual intervention was required in order to determine the origin of the plane. The only means to determine this was from the edge of the 3D dose cube. Again, this had to be carefully handled and checked to ensure that the 2D planar origin definition was accurate as otherwise this would impact the spatial accuracy results. The software had other limitations including not having the functionality to directly output mean distance-to-agreement for direct comparison with other authors. The software was also not able to import structures and project them on to the dosimetric plane of interest and so interpretation of dose differences at specific points in the target or organ at risk was difficult. Other software should be explored that allows for the import of the cardiac structures to aid interpretation for specific cardiac elements.

Gamma index criteria of global 3%/2mm and global 5%/1mm are both dose similarity metrics employed for the assessment of dose distributions in centralised quality assurance for spinal, nodal and soft tissue SABR in the UK. As such, these metrics were chosen initially to characterise the accuracy of the dose gradients used in cardiac SABR. The rationale for employing the 5%/1mm criterion (a very conservative distance-to-agreement component) allows for increased sensitivity to positional error which was useful for the determination of spatial correction but also reflective of the increased

importance of positional accuracy in SABR in the presence of high dose gradients, compared with conventionally fractionated radiotherapy. Additionally, the 5% dose-difference budget better allows for the 2.1% estimated overall measurement method uncertainty that was characterised as part of this research. Using a 5%/1mm gamma test metric as a measure of dosimetric deliverability is then able to detect clinically meaningful dosimetric differences in the presence of very high dose gradients used in stereotactic radiotherapy whilst remaining respective of (and therefore robust to) the uncertainty from the dosimeter alone.

The justification for measurement of overall dosimeter uncertainty for setting the results in context removed the requirement for repetition of every end-to-end measurement. This was validated by repeating the measurement of only Truebeam static delivery of PTV1 a further three times (section 2.5.4 and table 3.12). These results demonstrate that the 5%/1mm gamma test results remain highly robust in terms of the gamma test similarity with all results remaining above a 95% pass-rate threshold once a spatial correction of up to 1 mm is applied.

Although global gamma tests as a quantitative measure were beneficial when used alongside visual inspection to determine spatial error in 3 orthogonal directions, local gamma results were not found to be instructive in study interpretation due to variable and low values despite good visual profile overlay results.

Spatial errors were expected to be discovered in this research and those that are instructive arise from end-to-end system delivery errors. Origins of such errors are, for example, imaging-treatment system coincidence error, imaging localisation accuracy error arising from image quality, image co-registration error of the on-treatment

imaging with reference imaging, etc. However other sources of spatial uncertainty are possible from the study methodology itself, originating from sources such as the uncertainty in the spatial definition of the plane origin in treatment planning system as a result of the finite spatial resolution and the uncertainty in the definition of the origin on the film arising from the transfer of the origin from the insert with pen. When taken in combination, there was the possibility of these unwanted error sources to combine to produce spatial positional errors that would obscure the true delivery accuracy. Although all steps were taken to minimise these errors by using appropriate resolution for image acquisition & calculation grids and film pen marking accuracy, these potential errors were not zero. However, from the measurement of many plans in this research, the end-to-end positional accuracy determined (both the median and range) were very small which implies that such unwanted sources of error were both small and relatively randomly distributed.

Acknowledgement of the difficulty in minimising physical radiochromic film set-up errors to zero is important and the approach of allowing for a small (up to 1 mm) spatial correction before publishing gamma test results has been used in a recent national for stereotactic radiotherapy audit which adds to the justification of this technique (Dimitriadis et. al., 2020) alongside employment of the 5%/1mm gamma criterion.

4.4 Interpretation in the wider context

Although there exists no data specific to cardiac SABR in the literature to directly compare in terms of dose accuracy, nor are the same metrics used, there is value in attempting to draw some comparisons with the work of others for wider context. Distefano et. al. (2015), for example, found a mean spatial distance-to-agreement at the prescription isodose level of 1.3mm (1 s.d. of 2.2mm) in statically delivered lung SABR. Although the software used in this research did not allow for the same metric to be used, in lieu of this, sensitive gamma index was used to detect spatial errors in three orthogonal planes. Using this method, the magnitude of spatial corrections required were close to 0.5 mm median in all planes for all applications with a maximum of 1 mm which compares excellently to the published data, especially given the additional respiratory motion employed in this study. Although the quantitative metric used here is different and has lower resolution (as minimum spatial increments of only 1 mm were possible), there is an indication that these results are not only concordant with the findings of Distefano et. al., 2015 but also are commensurate with the current employment of uncertainty margins (3 mm to 5 mm) used in this clinical application. Small spatial errors detected for a rigid phantom with respiratory motion alone are beneficial when considering additional potential uncertainties arising from cardiac motion. In order to assess the impact of this motion further on the imaging quality and treatment delivery accuracy, this work should be extended to simulate cardiac motion, albeit in a rigid setting.

In terms of comparing the magnitude of dose differences in this research to others, this is more difficult as studies use various dosimeters each with their own inherent

uncertainty for absolute dose. In this research, however, using a single colour channel and EBT-3 film, the estimated achievable overall uncertainty from the dosimeter itself is characterised as a little over 2 % ($k=1$). This is justified as an acceptable level of measurement uncertainty for the determination of absolute delivered dose accuracy in the context of stereotactic radiotherapy for this indication where the presence of very high dose gradients mean that distance-to-agreement can be argued to be a more useful measure than dose difference, certainly in the centre of the target. Furthermore, the magnitude of measurement uncertainty is also in concordant with uncertainties found in others' research (Devic, 2011) despite the use of single colour channel dosimetry in this study.

When taking into account of the magnitude of the inherent underlying measurement uncertainty, the absolute dosimetric validation results (comparing calculated with measured dose) are highly encouraging in the context of the desired accuracy.

Considering each treatment platform independently, the median dose deviation between measured and calculated dose for CyberKnife was closer to zero (-1.5%) but with a relatively high interquartile range (4.5%); Truebeam VMAT had a median dose difference of -2.5% with a lower interquartile range of 0.7%. Note that the median dose deviation levels are comparable with the combined measurement uncertainty itself.

Although it is also difficult to compare parametric and non-parametric data variation, when considered in the context of Thwaites' (2013) exploration of the accuracy of modulated radiotherapy using point-based dosimetry in a non-anthropomorphic phantom for modulated radiotherapy techniques, our median results are within his

projected dose deviations of $\pm 2.5\%$ (1 s.d.) with our interquartile range within 2 s.d. of the work of Thwaites (2013). Similarly, when compared with the results of Hussein et. al., 2012 who project overall cumulative uncertainties of 1.8% to 3.4% (1 s.d.), the results of this research are, again, favourable.

Of course, it is recognised that the work of Thwaites and Hussein, was around a decade ago and there are likely to have been interim improvements in dose optimisation parameters for modulated radiotherapy in the TPS as well as improvements in the overall accuracy dose calculation engines over this time, therefore it is also useful to attempt to compare this research against more contemporary data. The work of Distefano et. al. (2021) examined lung SABR dose verification and demonstrated point dose variations of 1.7% (1 s.d.), similar to those variations seen by Hussein, although the level of calculation complexity was higher for Distefano due to proximate tissue heterogeneity.

It should further be acknowledged that the dose difference measure in this research is, in the main, not like-for-like with other authors. Other studies measured dose at discrete points, positionally designed to be in a low dose gradient region, whereas this research used a mean dose difference in a larger high dose region of a 2D dose plane that was not optimised to limit the dose gradient in that region and so this research is likely to be more vulnerable to gradient-based uncertainty in this context. That said, the median dose differences in this study, however, remain between 1 and 2 standard deviations of others' work, i.e., are of the same order of magnitude to those demonstrated by other authors.

The published exception in terms of measurement methodology is the work of Dimitriadis et. al. (2020) which did use radiochromic film to examine 2D dose similarity for intracranial stereotactic radiotherapy in a national audit in the same prescription dose range as this research. Interestingly those authors used the same gamma pass criteria as used in this study and achieved very similar levels of dose similarity; namely median pass rates (5%/1mm) greater than 98% when small spatial corrections were permitted, and no statistical detected between platform of delivery. Although the intracranial targets were arguably a simpler shape, the absolute dose interrogated and the dose gradients were of a similar magnitude meaning that it is encouraging that the achievable delivered dose accuracy appears transferable between one clinical indication and another, despite the increase in target shape complexity.

The overall small variations achieved in the Truebeam validation results coupled with similar results to those published by others indicate the potential for EBT-3 film to be used as an absolute dosimeter in the presence of high dose gradients, however a deeper examination of the causes of variability in the CyberKnife results is arguably justified.

Despite this variability in measured dose accuracy, the overall accuracy demonstrated in this research are encouraging when considered in the context of patient outcome and cardiac toxicity. The work of Darby et. al. (2013) predicts a 7% increase in the risk of a major coronary event per Gray of mean absorbed dose (figure 1.1). Given the mean doses to the left ventricle (PTV subtracted) in this study were of the order 4 - 7 Gy, a 1 Gy increase (7% rise in projected toxicity) is then equivalent to 14-25% increase in mean dose delivered to that region. Thus, if this research finds delivered dose to be

within a few per cent of calculated dose in the context of a very similar magnitude measurement uncertainty then this indicates that this methodology would provide a sensitive means to detect potentially clinically prognostic factors for major coronary event.

For control of the arrhythmic pathology, the dosimetric accuracy required is currently unknown, however it would be prudent to aim for dose accuracy of within 3 – 5%, based on what is achievable from the work of others and what is known from early pre-clinical cardiac SABR research. This novel research is able to provide significant assurance that this level of accuracy is achievable. Nonetheless, it is rightly acknowledged that given the magnitude of the combined dosimetric measurement uncertainty is of the same order as the resultant delivered dose accuracy, it would be beneficial to corroborate dosimetric accuracy results by including a second independent dosimeter, especially if this equipment and methodology is to be expanded for use in centralised quality assurance programmes. In such programmes, it is typical to include alanine as a second dosimeter for point dose measurement in low dose gradient regions in addition to radiochromic film to determine 2D dose accuracy. Alanine could easily be integrated with a simple 3D modelling phantom modification allowing alanine pellets to be inserted to an appropriate high dose region.

In summary, overall dose gradient similarity between calculated and measured doses are extremely high in this study and concordant with the most recent UK audit examining intracranial stereotactic radiotherapy. 5%/1mm gamma criterion and qualitative dose profile comparisons were used to detect and characterise spatial errors in 3D with those spatial errors being universally less than 1 mm in all planes.

Dose accuracy measurements of the order 1.5% to 2.5% (median) indicate a high level of agreement in the context of the work of others, are commensurate with the combined standard uncertainty arising from using radiochromic film as a sole dosimeter and differences of this order or magnitude can be justified in the clinical application and patient cohort examined.

Chapter 5: Conclusions

Cardiac SABR is an increasing area of interest that brings together the disciplines of cardiology, electrophysiology, clinical oncology, radiotherapy, and radiotherapy physics. It is of clinical interest due to the significant early evidence of its efficacy in the treatment of patients with debilitating and life-limiting cardiac arrhythmia that are refractory to existing treatment methods.

While initial clinical trial results appear to be positive, the use of SABR to treat these indications offer some distinct challenges in terms of target complexity for treatment planning, very high fractional absolute dose, novel means of target localisation and the existence of very proximate organs at risk. In the absence of future detrimental clinical results from patients undergoing the first treatments, all indications are that the use of cardiac SABR will continue to grow and become a common treatment for cardiac pathologies in the coming years.

Quality assurance is historically embedded in radiotherapy as a necessary step in the verification of treatment delivery accuracy; despite this, at the time of writing, there is no evidence found that systematically examines the end-to-end treatment delivery accuracy for this novel indication to provide convincing assurance of its quality. To facilitate prospective and retrospective patient outcome analyses, it is prudent that treatment planning and delivery systems are directly verified for accuracy so that calculated dose can be used as an accurate surrogate of delivered dose. This is critical where there exists historical evidence of cardiac doses being potentially predictive of cardiac morbidity and mortality.

This work has demonstrated that it is possible to design and produce an anthropomorphic cardiac phantom insert using 3D printing technology that can be housed in an existing and widely available commercial thorax phantom. Unlike other methods of verification of modulated radiotherapy that offer surrogate methods of fluence measurement and dose back-projection, this phantom provides direct absorbed dose measurement in critical cardiac planes using imaging localisation and motion management techniques typical to contemporary clinical practice.

When using this phantom alongside with carefully characterised EBT-3 film and single channel dosimetry as an absolute dosimeter, measurement uncertainty can be limited to an extent where it is a usable dosimeter to verify cardiac SABR planned dosimetry. Excellent levels of dosimetric accuracy for CyberKnife VSI and Varian Truebeam VMAT platforms have been demonstrated with achievable accuracy levels that are commensurate with the requirements of this indication and in keeping with others' findings for complex modulated radiotherapy.

Although there was an indication of a small but systematic spatial discrepancy of the order 1 mm when employing the prospectively gated technique, dosimetric accuracy was maintained compared with the static phantom setting. These positive results indicate that sophisticated motion management techniques should be explored for this indication in order to reduce the patient treated volume.

There is scope for this work to be furthered to include investigation of the effects of simulated cardiac motion in addition to respiratory motion examined here. Also, other phantom materials could be explored in order to expand the versatility of the phantom

to include more commercial linear accelerators beyond those using 2D or 3D kV imaging. Finally, the addition of an independent dosimeter to corroborate the absolute film dosimetry results and to allow direct point dose comparison with existing SABR quality assurance data might be of benefit. This is possible through simple modification of the modular configurable 3D model.

This anthropomorphic cardiac model and measurement methodology described facilitates independent examination of dose delivery accuracy for the mainstay of commercial radiotherapy delivery systems. This, in turn, facilitates the potential establishment (and maintenance) of minimum quality standards via centralised quality assurance. Minimising variation in radiotherapy delivery quality has the potential to improve future patient outcomes and/or reduce confounding factors in future large scale clinical trials for this novel indication.

References

- American Association of Physicists in Medicine. Report number 54: Stereotactic Radiosurgery. Report of Task Group 42 Radiation Therapy Committee.
https://aapm.org/pubs/reports/rpt_54.pdf (last accessed 12 January 2021).
- Ball, D., Mai, G.T., Vinod, S., Babington, S., Ruben, J., Kron, T., Chesson, B., Herschtal, A., Vanevski, M., Rezo, A., Elder, C., Skala, M., Wirth, A., Wheeler, G., Lim, A., Shaw, M., Schofield, P., Irving, L., Solomon, B., Nedev, N., Le, H., 2019. Stereotactic ablative radiotherapy versus standard radiotherapy in stage 1 non-small-cell lung cancer (TROG 09.02 CHISEL): a phase 3, open-label, randomised controlled trial. *The Lancet Oncology* 0. [https://doi.org/10.1016/S1470-2045\(18\)30896-9](https://doi.org/10.1016/S1470-2045(18)30896-9)
- Banfill, K., Sun, F., McWilliam, A., Abravan, A., Lilley, J., Wheller, B., Schmitt, M., Franks, K., Herk, M.V., Faivre-Finn, C., 2019. P1.16-20 Trial in Progress: Cardiac Toxicity in Patients Undergoing Curative Intent Radiotherapy for Lung Cancer. *Journal of Thoracic Oncology* 14, S594.
<https://doi.org/10.1016/j.jtho.2019.08.1246>
- Barbaro, N.M., Quigg, M., Ward, M.M., Chang, E.F., Broshek, D.K., Langfitt, J.T., Yan, G., Laxer, K.D., Cole, A.J., Sneed, P.K., Hess, C.P., Yu, W., Tripathi, M., Heck, C.N., Miller, J.W., Garcia, P.A., McEvoy, A., Fountain, N.B., Salanova, V., Knowlton, R.C., Bagić, A., Henry, T., Kapoor, S., McKhann, G., Palade, A.E., Reuber, M., Tecoma, E., 2018. Radiosurgery versus open surgery for mesial temporal lobe epilepsy: The randomized, controlled ROSE trial. *Epilepsia* 59, 1198–1207. <https://doi.org/10.1111/epi.14045>
- Bardinet E, Cohen LD, Ayache N. Tracking and motion analysis of the left ventricle with deformable superquadrics. *Medical Image Analysis*, 1996, 1 (2), pp.129-149.
<https://doi.org/10.1016/S1361-8415>
- Barker, F.G., Jannetta, P.J., Bissonette, D.J., Larkins, M.V., Jho, H.D., 1996. The Long-Term Outcome of Microvascular Decompression for Trigeminal Neuralgia. *New England Journal of Medicine* 334, 1077–1084. <https://doi.org/10.1056/NEJM199604253341701>
- Bartolomei, F., Hayashi, M., Tamura, M., Rey, M., Fischer, C., Chauvel, P., Régis, J., 2008. Long-term efficacy of gamma knife radiosurgery in mesial temporal lobe epilepsy. *Neurology* 70, 1658–1663. <https://doi.org/10.1212/01.wnl.0000294326.05118.d8>

- Benedict, S.H., Yenice, K.M., Followill, D., Galvin, J.M., Hinson, W., Kavanagh, B., Keall, P., Lovelock, M., Meeks, S., Papiez, L., Purdie, T., Sadagopan, R., Schell, M.C., Salter, B., Schlesinger, D.J., Shiu, A.S., Solberg, T., Song, D.Y., Stieber, V., Timmerman, R., Tomé, W.A., Verellen, D., Wang, L., Yin, F.-F., 2010. Stereotactic body radiation therapy: The report of AAPM Task Group 101. *Medical Physics* 37, 4078–4101. <https://doi.org/10.1118/1.3438081>
- Blanck, O., Bode, F., Gebhard, M., Hunold, P., Brandt, S., Bruder, R., Grossherr, M., Vonthein, R., Rades, D., Dunst, J., 2014. Dose-escalation study for cardiac radiosurgery in a porcine model. *Journal of Radiation Oncology* 89, 590–598. <https://doi.org/10.1016/j.ijrobp.2014.02.036>
- Blomgren, H., Lax, I., Näslund, I., Svanström, R., 1995. Stereotactic High Dose Fraction Radiation Therapy of Extracranial Tumors Using An Accelerator: Clinical experience of the first thirty-one patients. *Acta Oncologica* 34, 861–870. <https://doi.org/10.3109/02841869509127197>
- Bonomo, P., Cipressi, S., Desideri, I., Masi, L., Doro, R., Iermano, C., Greto, D., Simontacchi, G., Mangoni, M., Paiar, F., Meattini, I., Scoccianti, S., Santoro, G., Valente, S., Gensini, G.F., Livi, L., 2015. Stereotactic Body Radiotherapy with Cyberknife for Cardiac Malignancies. *Tumori Journal* 101, 294–297. <https://doi.org/10.5301/tj.5000280>
- Bradley, J.D., Paulus, R., Komaki, R., Masters, G., Blumenschein, G., Schild, S., Bogart, J., Hu, C., Forster, K., Magliocco, A., Kavadi, V., Garces, Y.I., Narayan, S., Iyengar, P., Robinson, C., Wynn, R.B., Koprowski, C., Meng, J., Beitler, J., Gaur, R., Curran, W., Choy, H., 2015. Standard-dose versus high-dose conformal radiotherapy with concurrent and consolidation carboplatin plus paclitaxel with or without cetuximab for patients with stage IIIA or IIIB non-small-cell lung cancer (RTOG 0617): a randomised, two-by-two factorial phase 3 study. *The Lancet Oncology* 16, 187–199. [https://doi.org/10.1016/S1470-2045\(14\)71207-0](https://doi.org/10.1016/S1470-2045(14)71207-0)
- Brahme, A., 1984. Dosimetric Precision Requirements in Radiation Therapy. *Acta Radiologica: Oncology* 23, 379–391. <https://doi.org/10.3109/02841868409136037>
- Brown, P.D., Jaeckle, K., Ballman, K.V., Farace, E., Cerhan, J.H., Anderson, S.K., Carrero, X.W., Barker, F.G., Deming, R., Burri, S.H., Ménard, C., Chung, C., Stieber, V.W., Pollock, B.E., Galanis, E., Buckner, J.C., Asher, A.L., 2016. Effect of Radiosurgery Alone vs Radiosurgery With Whole Brain Radiation Therapy on Cognitive Function in Patients With 1 to 3 Brain Metastases. *JAMA* 316, 401–409. <https://doi.org/10.1001/jama.2016.9839>

- Carlson, L.E., Watt, G.P., Tonorezos, E.S., Chow, E.J., Yu, A.F., Woods, M., Lynch, C.F., John, E.M., Mellekjær, L., Brooks, J.D., Knight, J.A., Reiner, A.S., Liang, X., Smith, S.A., Bernstein, L., Dauer, L.T., Cerviño, L.I., Howell, R.M., Shore, R.E., Boice, J.D., Bernstein, J.L., Bernstein, J.L., Capanu, M., Orlow, I., Robson, M., Olsen, J.H., Malone, K.E., Stovall, M., Blackmore, K., Harris, I., Langballe, R., O'Brien, C., Weathers, R., West, M., Hunter, L., Goldstein, J., Ramos, E., 2021. Coronary Artery Disease in Young Women After Radiation Therapy for Breast Cancer: The WECARE Study. *JACC: CardioOncology* 3, 381–392.
<https://doi.org/10.1016/j.jaccao.2021.07.008>
- Carmel, R.J., Kaplan, H.S., 1976. Mantle irradiation in Hodgkin's disease. An analysis of technique, tumor eradication, and complications. *Cancer* 37, 2813–2825.
- Castro, P., García-Vicente, F., Mínguez, C., Floriano, A., Sevillano, D., Pérez, L., Torres, J.J., 2008. Study of the uncertainty in the determination of the absorbed dose to water during external beam radiotherapy calibration. *Journal of Applied Clinical Medical Physics* 9, 70–86.
<https://doi.org/10.1120/jacmp.v9i1.2676>
- Chen, X., Dong, J.-Z., Du, X., Wu, J.-H., Yu, R.-H., Long, D.-Y., Ning, M., Sang, C.-H., Jiang, C.-X., Bai, R., Wen, S.-N., Liu, N., Li, S.-N., Xu, Z.-Y., Ma, C.-S., Tang, R.-B., 2018. Long-term outcome of catheter ablation for atrial fibrillation in patients with apical hypertrophic cardiomyopathy. *J. Cardiovasc. Electrophysiol.* 29, 951–957. <https://doi.org/10.1111/jce.13645>
- Clark, C.H., Aird, E.G., Bolton, S., Miles, E.A., Nisbet, A., Snaith, J.A., Thomas, R.A., Venables, K., Thwaites, D.I., 2015. Radiotherapy dosimetry audit: three decades of improving standards and accuracy in UK clinical practice and trials. *Br J Radiol* 88. <https://doi.org/10.1259/bjr.20150251>
- Clark, C.H., Hurkmans, C.W., Kry, S.F., of Radiation, T.G.Q.A., Group, T.C.T.H., 2017. The role of dosimetry audit in lung SBRT multi-centre clinical trials. *Physica Medica* 44, 171–176.
- Clark, C.H., Hussein, M., Tsang, Y., Thomas, R., Wilkinson, D., Bass, G., Snaith, J., Gouldstone, C., Bolton, S., Nutbrown, R., Venables, K., Nisbet, A., 2014. A multi-institutional dosimetry audit of rotational intensity-modulated radiotherapy. *Radiotherapy and Oncology* 113, 272–278.
<https://doi.org/10.1016/j.radonc.2014.11.015>
- Clark, C.H., Jornet, N., Muren, L.P., 2018. The role of dosimetry audit in achieving high quality radiotherapy. *Physics and Imaging in Radiation Oncology* 5, 85–87.
<https://doi.org/10.1016/j.phro.2018.03.009>
- Cohn, K.E., Stewart, J.R., Fajardo, L.F., Hancock, E.W., 1967. Heart disease following radiation. *Medicine* 46, 281–298.

- Conibear, J., Spezi, E., Gujral, D., Miah, A., Bernstein, D., Wells, E., Nutting, C., 2013. PO-0937: Impact of quality assurance on contour conformity within two UK head & neck radiotherapy trials. *Radiotherapy and Oncology* 106, S359. [https://doi.org/10.1016/S0167-8140\(15\)33243-6](https://doi.org/10.1016/S0167-8140(15)33243-6)
- Corn, B.W., Trock, B.J., Goodman, R.L., 1990. Irradiation-related ischemic heart disease. [Review] [56 refs]. *Journal of Clinical Oncology* 8, 741–750.
- Cuculich, P.S., Schill, M.R., Kashani, R., Mutic, S., Lang, A., Cooper, D., Faddis, M., Gleva, M., Noheria, A., Smith, T.W., Hallahan, D., Rudy, Y., Robinson, C.G., 2017. Noninvasive Cardiac Radiation for Ablation of Ventricular Tachycardia. *Journal of Medicine* 377, 2325–2336. <https://doi.org/10.1056/NEJMoa1613773>
- Cuomo, J.R., Sharma, G.K., Conger, P.D., Weintraub, N.L., 2016. Novel concepts in radiation-induced cardiovascular disease. *World J Cardiol* 8, 504–519. <https://doi.org/10.4330/wjc.v8.i9.504>
- Darby, S.C., Ewertz, M., McGale, P., Bennet, A.M., Blom-Goldman, U., Brønnum, D., Correa, C., Cutter, D., Gagliardi, G., Gigante, B., Jensen, M.-B., Nisbet, A., Peto, R., Rahimi, K., Taylor, C., Hall, P., 2013. Risk of Ischemic Heart Disease in Women after Radiotherapy for Breast Cancer. *New England Journal of Medicine* 368, 987–998. <https://doi.org/10.1056/NEJMoa1209825>
- Devic, S., 2011. Radiochromic film dosimetry: Past, present, and future. *Physica Medica* 27, 122–134. <https://doi.org/10.1016/j.ejmp.2010.10.001>
- Devic, S., Tomic, N., Lewis, D., 2016. Reference radiochromic film dosimetry: Review of technical aspects. *Physica Medica* 32, 541–556. <https://doi.org/10.1016/j.ejmp.2016.02.008>
- Dimitriadis, A., Tsang, Y., Thomas, R.A.S., Palmer, A.L., Eaton, D., Lee, J., Patel, R., Patallo, I.S., Gouldstone, C., Snaith, J.A.D., Kirkby, K.J., Nisbet, A., Clark, C.H., 2020. Multi-institutional dosimetric delivery assessment of intracranial stereotactic radiosurgery on different treatment platforms. *Radiotherapy and Oncology* 147, 153–161. <https://doi.org/10.1016/j.radonc.2020.05.024>
- Distefano, G., Jafari, S.M., Lee, J., Gouldstone, C., Mayles, H.M.O., Clark, C.H., 2015. OC-0155: UK SABR Consortium Lung Dosimetry Audit; absolute dosimetry results. *Radiotherapy and Oncology* 115, S75–S76. [https://doi.org/10.1016/S0167-8140\(15\)40153-7](https://doi.org/10.1016/S0167-8140(15)40153-7)
- Dunbar, S.B., Dougherty, C.M., Sears, S.F., Carroll, D.L., Goldstein, N.E., Mark, D.B., McDaniel, G., Pressler, S.J., Schron, E., Wang, P., Zeigler, V.L., American Heart Association Council on Cardiovascular Nursing, Council on Clinical Cardiology, and Council on Cardiovascular Disease in the Young, 2012. Educational and psychological interventions to improve outcomes for recipients of implantable cardioverter defibrillators and their families: a scientific statement

- from the American Heart Association. *Circulation* 126, 2146–2172.
<https://doi.org/10.1161/CIR.Ob013e31825d59fd>
- Eaton DJ, S, B., Ra, T., Ch, C., 2015. Inter-departmental dosimetry audits - development of methods and lessons learned. *J Med Phys* 40, 183–189. <https://doi.org/10.4103/0971-6203.170791>
- Eaton, D.J., Tyler, J., Backshall, A., Bernstein, D., Carver, A., Gasnier, A., Henderson, J., Lee, J., Patel, R., Tsang, Y., Yang, H., Zotova, R., Wells, E., 2017. An external dosimetry audit programme to credential static and rotational IMRT delivery for clinical trials quality assurance. *Physica Medica* 35, 25–30. <https://doi.org/10.1016/j.ejmp.2017.02.012>
- Escalated-dose versus standard-dose conformal radiotherapy in prostate cancer: first results from the MRC RT01 randomised controlled trial - The Lancet Oncology [WWW Document], n.d. URL [https://www.thelancet.com/journals/lanonc/article/PIIS1470-2045\(07\)70143-2/fulltext](https://www.thelancet.com/journals/lanonc/article/PIIS1470-2045(07)70143-2/fulltext) (accessed 5.19.21).
- Esposito, M., Ghirelli, A., Pini, S., Alpi, P., Barca, R., Fondelli, S., Grilli Leonulli, B., Paoletti, L., Rossi, F., Bastiani, P., Russo, S., 2021. Clinical implementation of 3D in vivo dosimetry for abdominal and pelvic stereotactic treatments. *Radiotherapy and Oncology* 154, 14–20.
<https://doi.org/10.1016/j.radonc.2020.09.011>
- European Commission guidelines on clinical audit. Statement by the European Society of Radiology, 2011. . *Insights Imaging* 2, 97–98. <https://doi.org/10.1007/s13244-011-0065-8>
- Faivre-Finn, C., Fenwick, J.D., Franks, K.N., Harrow, S., Hatton, M.Q.F., Hiley, C., McAleese, J.J., McDonald, F., O'Hare, J., Peedell, C., Pope, T., Powell, C., Rulach, R., Toy, E., 2020. Reduced Fractionation in Lung Cancer Patients Treated with Curative-intent Radiotherapy during the COVID-19 Pandemic. *Clinical Oncology* 32, 481–489.
<https://doi.org/10.1016/j.clon.2020.05.001>
- Fields, H.L., 1996. Treatment of trigeminal neuralgia. *N. Engl. J. Med.* 334, 1125–1126.
<https://doi.org/10.1056/NEJM199604253341709>
- Gardner, E.A., Sumanaweera, T.S., Blanck, O., Iwamura, A.K., Steel, J.P., Dieterich, S., Maguire, P., 2012. In vivo dose measurement using TLDs and MOSFET dosimeters for cardiac radiosurgery. *Journal of Applied Clinical Medical Physics* 13, 190–203.
<https://doi.org/10.1120/jacmp.v13i3.3745>
- Gianni, C., Mohanty, S., Trivedi, C., Di Biase, L., Al-Ahmad, A., Natale, A., David Burkhardt, J., 2017. Alternative Approaches for Ablation of Resistant Ventricular Tachycardia. *Cardiac Electrophysiology Clinics* 9, 93–98. <https://doi.org/10.1016/j.ccep.2016.10.006>

- Gomez, D.R., Blumenschein, G.R., Lee, J.J., Hernandez, M., Ye, R., Camidge, D.R., Doebele, R.C., Skoulidis, F., Gaspar, L.E., Gibbons, D.L., Karam, J.A., Kavanagh, B.D., Tang, C., Komaki, R., Louie, A.V., Palma, D.A., Tsao, A.S., Sepesi, B., William, W.N., Zhang, J., Shi, Q., Wang, X.S., Swisher, S.G., Heymach, J.V., 2016. Local consolidative therapy versus maintenance therapy or observation for patients with oligometastatic non-small-cell lung cancer without progression after first-line systemic therapy: a multicentre, randomised, controlled, phase 2 study. *The Lancet Oncology* 17, 1672–1682. [https://doi.org/10.1016/S1470-2045\(16\)30532-0](https://doi.org/10.1016/S1470-2045(16)30532-0)
- Grams, M.P., Gustafson, J.M., Long, K.M., de los Santos, L.E.F., 2015. Technical Note: Initial characterization of the new EBT-XD Gafchromic film. *Medical Physics* 42, 5782–5786. <https://doi.org/10.1118/1.4930058>
- Halasz, L.M., Uno, H., Hughes, M., D’Amico, T., Dexter, E.U., Edge, S.B., Hayman, J.A., Niland, J.C., Otterson, G.A., Pisters, K.M.W., Theriault, R., Weeks, J.C., Punglia, R.S., 2016. Comparative effectiveness of stereotactic radiosurgery versus whole-brain radiation therapy for patients with brain metastases from breast or non-small cell lung cancer. *Cancer* 122, 2091–2100. <https://doi.org/10.1002/cncr.30009>
- Halvorsen, P.H., Cirino, E., Das, I.J., Garrett, J.A., Yang, J., Yin, F.-F., Fairbrent, L.A., 2017. AAPM-RSS Medical Physics Practice Guideline 9.a. for SRS-SBRT. *Journal of Applied Clinical Medical Physics* 18, 10–21. <https://doi.org/10.1002/acm2.12146>
- Hussein, M., Tsang, Y., Thomas, R., Gouldstone, C., Maughan, D., Snaith, J., Bolton, S., Clark, C.H., 2012. OC-0064 ROTATIONAL RADIOTHERAPY IN THE UK – A PILOT AUDIT. *Radiotherapy and Oncology Supplement* 1, S25–S26. [https://doi.org/10.1016/S0167-8140\(12\)70403-6](https://doi.org/10.1016/S0167-8140(12)70403-6)
- Ibbott, G.S., 2010. QA in Radiation Therapy: The RPC Perspective. *J. Phys.: Conf. Ser.* 250, 012001. <https://doi.org/10.1088/1742-6596/250/1/012001>
- ICRU Report 83, Prescribing, Recording, and Reporting Intensity-Modulated Photon-Beam Therapy (IMRT) – ICRU <https://www.icru.org/report/prescribing-recording-and-reporting-intensity-modulated-photon-beam-therapy-imrticru-report-83/> (accessed 9.11.22).
- Izewska, J., Andreo, P., 2000. The IAEA/WHO TLD postal programme for radiotherapy hospitals. *Radiotherapy and Oncology* 54, 65–72. [https://doi.org/10.1016/S0167-8140\(99\)00164-4](https://doi.org/10.1016/S0167-8140(99)00164-4)
- Jin, Q., Jacobsen, P.K., Pehrson, S., Chen, X., 2017. Prediction and prognosis of ventricular tachycardia recurrence after catheter ablation with remote magnetic navigation for electrical storm in patients with ischemic cardiomyopathy. *Clinical Cardiology* 40, 1083–1089. <https://doi.org/10.1002/clc.22773>

- Joensuu, H., 1989. Acute myocardial infarction after heart irradiation in young patients with Hodgkin's disease. *Chest* 95, 388–390.
- Johansson, K.-A., Hanson, W.F., Horiot, J.C., 1988. Workshop of the EORTC radiotherapy group on quality assurance in cooperative trials of radiotherapy: A recommendation for EORTC cooperative groups. *Radiotherapy and Oncology* 11, 201–203. [https://doi.org/10.1016/0167-8140\(88\)90001-1](https://doi.org/10.1016/0167-8140(88)90001-1)
- Johnson-Hart, C.N., Price, G.J., Faivre-Finn, C., Aznar, M.C., van Herk, M., 2018. Residual Setup Errors Towards the Heart After Image Guidance Linked With Poorer Survival in Lung Cancer Patients: Do We Need Stricter IGRT Protocols? *Int. J. Radiat. Oncol. Biol. Phys.* 102, 434–442. <https://doi.org/10.1016/j.ijrobp.2018.05.052>
- Kim, E.J., Vermeulen, S., Li, F.J., Newell, D.W., 2014. A review of cerebral arteriovenous malformations and treatment with stereotactic radiosurgery. *Translational Cancer Research* 3, 399–410–410. <https://doi.org/10.21037/2951>
- Kroiss, M., Patel, R., Diez, P., 2022. PO-1030 Quantitative benefit of centralised quality assurance for the implementation of Lung SABR. *Radiotherapy and Oncology* 170, S866. [https://doi.org/10.1016/S0167-8140\(22\)02994-2](https://doi.org/10.1016/S0167-8140(22)02994-2)
- Kron, T., Fox, C., Ebert, M.A., Thwaites, D., 2022. Quality management in radiotherapy treatment delivery. *Journal of medical imaging and radiation oncology* 66, 279–290. <https://doi.org/10.1111/1754-9485.13348>
- Lee, J., Bates, M., Shepherd, E., Riley, S., Henshaw, M., Metherall, P., Daniel, J., Blower, A., Scoones, D., Wilkinson, M., Richmond, N., Robinson, C., Cuculich, P., Hugo, G., Seller, N., McStay, R., Child, N., Thornley, A., Kelland, N., Atherton, P., Peedell, C., Hatton, M., 2021. Cardiac stereotactic ablative radiotherapy for control of refractory ventricular tachycardia: initial UK multicentre experience. *Open Heart* 8, e001770. <https://doi.org/10.1136/openhrt-2021-001770>
- Lee, J., Mayles, H.M.O., Baker, C.R., Jafari, S.M., Distefano, G., Clark, C.H., 2015. UK SABR Consortium Lung Dosimetry Audit; relative dosimetry results, in: *Radiotherapy and Oncology. Presented at the European Society for Radiotherapy and Oncology conference (3rd ESTRO Forum), Elsevier, Barcelona, Spain, pp. S74–S75.*
- Lee, J., Dean, C., Patel, R., Webster, G., Eaton, D.J., 2019. Multi-center evaluation of dose conformity in stereotactic body radiotherapy. *Physics and Imaging in Radiation Oncology* 11, 41–46. <https://doi.org/10.1016/j.phro.2019.08.002>

- Loo, B.W.J., Soltys, S.G., Wang, L., Lo, A., Fahimian, B.P., Iagaru, A., Norton, L., Shan, X., Gardner, E., Fogarty, T., Maguire, P., Al-Ahmad, A., Zei, P., 2015. Stereotactic ablative radiotherapy for the treatment of refractory cardiac ventricular arrhythmia. *Circulation: Arrhythmia and Electrophysiology* 8, 748–750. <https://doi.org/10.1161/CIRCEP.115.002765>
- Low, D.A., Mutic, S., Dempsey, J.F., Gerber, R.L., Bosch, W.R., Perez, C.A., Purdy, J.A., 1998. Quantitative dosimetric verification of an IMRT planning and delivery system. *Radiotherapy and Oncology* 49, 305–316. [https://doi.org/10.1016/S0167-8140\(98\)00125-X](https://doi.org/10.1016/S0167-8140(98)00125-X)
- Lydiard, Pgd., Suzanne, Blanck, O., Hugo, G., O'Brien, R., Keall, P., 2021. A Review of Cardiac Radioablation (CR) for Arrhythmias: Procedures, Technology, and Future Opportunities. *International Journal of Radiation Oncology* Biology* Physics* 109, 783–800. <https://doi.org/10.1016/j.ijrobp.2020.10.036>
- MacDougall, N.D., Graveling, M., Hansen, V.N., Brownsword, K., Morgan, A., 2017. In vivo dosimetry in UK external beam radiotherapy: current and future usage. *Br J Radiol* 90, 20160915. <https://doi.org/10.1259/bjr.20160915>
- McCaw, T.J., Micka, J.A., DeWerd, L.A., 2011. Characterizing the marker-dye correction for Gafchromic® EBT2 film: A comparison of three analysis methods. *Medical Physics* 38, 5771–5777. <https://doi.org/10.1118/1.3639997>
- McDonald, C.R., Norman, M.A., Tecoma, E., Alksne, J., Iragui, V., 2004. Neuropsychological change following gamma knife surgery in patients with left temporal lobe epilepsy: a review of three cases. *Epilepsy Behav* 5, 949–957. <https://doi.org/10.1016/j.yebeh.2004.08.014>
- McWilliam, A., Kennedy, J., Hodgson, C., Vasquez Osorio, E., Faivre-Finn, C., van Herk, M., 2017. Radiation dose to heart base linked with poorer survival in lung cancer patients. *Eur. J. Cancer* 85, 106–113. <https://doi.org/10.1016/j.ejca.2017.07.053>
- Menzel, H.-G., 2014. International commission on radiation units and measurements. *Journal of the ICRU* 14, 1–2.
- Merskey, H.E., 1986. Classification of chronic pain: descriptions of chronic pain syndromes and definitions of pain terms. *Pain*.
- Mijnheer, B.J., Battermann, J.J., Wambersie, A., 1987. What degree of accuracy is required and can be achieved in photon and neutron therapy? *Radiotherapy and Oncology* 8, 237–252. [https://doi.org/10.1016/S0167-8140\(87\)80247-5](https://doi.org/10.1016/S0167-8140(87)80247-5)

- Møller, S., Jensen, M.-B., Ejlersen, B., Bjerre, K.D., Larsen, M., Hansen, H.B., Christiansen, P., Mouridsen, H.T., 2008. The clinical database and the treatment guidelines of the Danish Breast Cancer Cooperative Group (DBCG); its 30-years experience and future promise. *Acta Oncologica* 47, 506–524. <https://doi.org/10.1080/02841860802059259>
- Moore, A.R., Jim Warrington, A.P., Aird, E.G.A., Margaret Bidmead, A., Dearnaley, D.P., 2006. A versatile phantom for quality assurance in the UK Medical Research Council (MRC) RT01 trial (ISRCTN47772397) in conformal radiotherapy for prostate cancer. *Radiotherapy and Oncology* 80, 82–85. <https://doi.org/10.1016/j.radonc.2006.06.003>
- NHS England Commissioning Board. Clinical Commissioning Policy: Stereotactic Radiosurgery for Cerebral Ateriovenous Malformations. April 2013. <https://www.england.nhs.uk/commissioning/wp-content/uploads/sites/12/2013/10/d05-p-c.pdf> (last accessed 15 August 2022)
- NHS England Commissioning Board. Clinical Commissioning Policy: Sterotactic Radiosurgery for Trigeminal Neuralgia. April 2013. [NHS England » Clinical Commissioning Policy: Stereotactic Radiosurgery for Trigeminal Neuralgia](#) (last accessed 12 August 2022)
- Niroomand-Rad, A., Chiu-Tsao, S.-T., Grams, M., Lewis, D., Soares, C., Battum, L.J., Das, I., Trichter, S., Kissick, M., Massillon-JI, G., Alvarez, P., Chan, M., 2020. Report of AAPM Task Group 235 Radiochromic Film Dosimetry: An Update to TG-55. *Medical Physics* 47, 5986–6025. <https://doi.org/10.1002/mp.14497>
- Ohri, N., Shen, X., Dicker, A.P., Doyle, L.A., Harrison, A.S., Showalter, T.N., 2013. Radiotherapy protocol deviations and clinical outcomes: a meta-analysis of cooperative group clinical trials. *Journal of the National Cancer Institute* 105, 387–393.
- Olch, A.J., 2002. Dosimetric performance of an enhanced dose range radiographic film for intensity-modulated radiation therapy quality assurance. *Medical Physics* 29, 2159–2168. <https://doi.org/10.1118/1.1500398>
- Onishi, H., Araki, T., Shirato, H., Nagata, Y., Hiraoka, M., Gomi, K., Yamashita, T., Niibe, Y., Karasawa, K., Hayakawa, K., Takai, Y., Kimura, T., Hirokawa, Y., Takeda, A., Ouchi, A., Hareyama, M., Kokubo, M., Hara, R., Itami, J., Yamada, K., 2004. Stereotactic hypofractionated high-dose irradiation for stage I nonsmall cell lung carcinoma: clinical outcomes in 245 subjects in a Japanese multiinstitutional study. *Cancer* 101, 1623–1631. <https://doi.org/10.1002/cncr.20539>

- Palma, D.A., Olson, R.A., Harrow, S., Gaede, S., Louie, A.V., Haasbeek, C., Mulroy, L.A., Lock, M.I., Rodrigues, G., Yaremko, B.P., Schellenberg, D., Ahmad, B., Griffioen, G., Senthil, S., Liu, M.C., Moore, K., Currie, S., Bauman, G.S., Warner, A., Senan, S., 2018. Stereotactic Ablative Radiation Therapy for the Comprehensive Treatment of Oligometastatic Tumors (SABR-COMET): Results of a Randomized Trial. *International Journal of Radiation Oncology • Biology • Physics* 102, S3–S4. <https://doi.org/10.1016/j.ijrobp.2018.06.105>
- Palmer, A.L., Bradley, D., Nisbet, A., 2014. Evaluation and implementation of triple-channel radiochromic film dosimetry in brachytherapy. *Journal of Applied Clinical Medical Physics* 15, 280–296. <https://doi.org/10.1120/jacmp.v15i4.4854>
- Pappone, C., Rosanio, S., Oreto, G., Tocchi, M., Gugliotta, F., Vicedomini, G., Salvati, A., Dicandia, C., Mazzone, P., Santinelli, V., Gulletta, S., Chierchia, S., 2000. Circumferential radiofrequency ablation of pulmonary vein ostia: A new anatomic approach for curing atrial fibrillation. *Circulation* 102, 2619–2628.
- Pedersen, C.T., Kay, G.N., Kalman, J., Borggrefe, M., Della-Bella, P., Dickfeld, T., Dorian, P., Huikuri, H., Kim, Y.-H., Knight, B., Marchlinski, F., Ross, D., Sacher, F., Sapp, J., Shivkumar, K., Soejima, K., Tada, H., Alexander, M.E., Triedman, J.K., Yamada, T., Kirchhof, P., Lip, G.Y.H., Kuck, K.H., Mont, L., Haines, D., Indik, J., Dimarco, J., Exner, D., Iesaka, Y., Savelieva, I., 2014. EHRA/HRS/APHRS expert consensus on ventricular arrhythmias. *Journal of Arrhythmia* 30, 327–349. <https://doi.org/10.1016/j.joa.2014.08.001>
- Pfaffenberger, S., Bartko, P., Graf, A., Pernicka, E., Babayev, J., Lolic, E., Bonderman, D., Baumgartner, H., Maurer, G., Mascherbauer, J., 2013. Size Matters! Impact of Age, Sex, Height, and Weight on the Normal Heart Size. *Circulation: Cardiovascular Imaging* 6, 1073–1079. <https://doi.org/10.1161/CIRCIMAGING.113.000690>
- Priori, S.G., Blomström-Lundqvist, C., Mazzanti, A., Blom, N., Borggrefe, M., Camm, J., Elliott, P.M., Fitzsimons, D., Hatala, R., Hindricks, G., Kirchhof, P., Kjeldsen, K., Kuck, K.-H., Hernandez-Madrid, A., Nikolaou, N., Norekvål, T.M., Spaulding, C., Van Veldhuisen, D.J., ESC Scientific Document Group, 2015. 2015 ESC Guidelines for the management of patients with ventricular arrhythmias and the prevention of sudden cardiac death: The Task Force for the Management of Patients with Ventricular Arrhythmias and the Prevention of Sudden Cardiac Death of the European Society of Cardiology (ESC). Endorsed by: Association for European Paediatric and Congenital Cardiology (AEPC). *Eur. Heart J.* 36, 2793–2867. <https://doi.org/10.1093/eurheartj/ehv316>

- Quigg, M., Harden, C., 2014. Minimally invasive techniques for epilepsy surgery: stereotactic radiosurgery and other technologies. [Review]. *Journal of Neurosurgery* 1, 232–240.
<https://doi.org/10.3171/2014.8.GKS141608>
- Régis, J., Bartolomei, F., Rey, M., Genton, P., Dravet, C., Semah, F., Gastaut, J.L., Chauvel, P., Peragut, J.C., 1999. Gamma knife surgery for mesial temporal lobe epilepsy. *Epilepsia* 40, 1551–1556.
- Rink, A., Vitkin, I.A., Jaffray, D.A., 2007. Energy dependence (to) of radiochromic films assessed using a real-time optical dosimeter. *Medical Physics* 34, 458–463.
<https://doi.org/10.1118/1.2431425>
- Sahgal, A., Aoyama, H., Kocher, M., Neupane, B., Collette, S., Tago, M., Shaw, P., Beyene, J., Chang, E.L., 2015. Phase 3 Trials of Stereotactic Radiosurgery With or Without Whole-Brain Radiation Therapy for 1 to 4 Brain Metastases: Individual Patient Data Meta-Analysis. *International Journal of Radiation Oncology*Biophysics* 91, 710–717.
<https://doi.org/10.1016/j.ijrobp.2014.10.024>
- Santangeli, P., Frankel, D.S., Tung, R., Vaseghi, M., Sauer, W.H., Tzou, W.S., Mathuria, N., Nakahara, S., Dickfeldt, T.M., Lakkireddy, D., Bunch, T.J., Di Biase, L., Natale, A., Tholakanahalli, V., Tedrow, U.B., Kumar, S., Stevenson, W.G., Della Bella, P., Shivkumar, K., Marchlinski, F.E., Callans, D.J., International VT Ablation Center Collaborative Group, 2017. Early Mortality After Catheter Ablation of Ventricular Tachycardia in Patients With Structural Heart Disease. *J. Am. Coll. Cardiol.* 69, 2105–2115. <https://doi.org/10.1016/j.jacc.2017.02.044>
- Sapp, J.L., Wells, G.A., Parkash, R., Stevenson, W.G., Blier, L., Sarrazin, J.-F., Thibault, B., Rivard, L., Gula, L., Leong-Sit, P., Essebag, V., Nery, P.B., Tung, S.K., Raymond, J.-M., Sterns, L.D., Veenhuizen, G.D., Healey, J.S., Redfearn, D., Roux, J.-F., Tang, A.S.L., 2016. Ventricular Tachycardia Ablation versus Escalation of Antiarrhythmic Drugs. *New England Journal of Medicine* 375, 111–121. <https://doi.org/10.1056/NEJMoa1513614>
- Schröttner, O., Eder, H.G., Unger, F., Feichtinger, K., Pendl, G., 1998. Radiosurgery in Lesional Epilepsy: Brain Tumors. *SFN* 70, 50–56. <https://doi.org/10.1159/000056406>
- Shalek, R.J., 1977. Determination of absorbed dose in a patient irradiated by beams of X or gamma rays in radiotherapy procedures. Wiley Online Library.
- Sharma, A., Wong, D., Weidlich, G., Fogarty, T., Jack, A., Sumanaweera, T., Maguire, P., 2010. Noninvasive stereotactic radiosurgery (CyberHeart) for creation of ablation lesions in the atrium. *Heart Rhythm* 7, 802–810. <https://doi.org/10.1016/j.hrthm.2010.02.010>

- Shechter, G., Resar, J.R., McVeigh, E.R., 2006. Displacement and velocity of the coronary arteries: Cardiac and respiratory motion. *IEEE transactions on medical imaging* 25, 369–375.
<https://doi.org/10.1109/TMI.2005.862752>
- Shrimpton, P.C., 1981. Electron density values of various human tissues: in vitro Compton scatter measurements and calculated ranges. *Phys. Med. Biol.* 26, 907–911.
<https://doi.org/10.1088/0031-9155/26/5/010>
- Soares, C.G., Devic, S., n.d. Chapter 23 Radiochromic Film 56.
- Sorriaux, J., Kacperek, A., Rossomme, S., Lee, J.A., Bertrand, D., Vynckier, S., Sterpin, E., 2013. Evaluation of Gafchromic® EBT3 films characteristics in therapy photon, electron and proton beams. *Physica Medica: European Journal of Medical Physics* 29, 599–606.
<https://doi.org/10.1016/j.ejmp.2012.10.001>
- Speirs, C.K., DeWees, T.A., Rehman, S., Molotievski, A., Velez, M.A., Mullen, D., Fergus, S., Trovo, M., Bradley, J.D., Robinson, C.G., 2017. Heart Dose Is an Independent Dosimetric Predictor of Overall Survival in Locally Advanced Non-Small Cell Lung Cancer. *J Thorac Oncol* 12, 293–301.
<https://doi.org/10.1016/j.jtho.2016.09.134>
- Stam, B., Peulen, H., Guckenberger, M., Mantel, F., Hope, A., Werner-Wasik, M., Belderbos, J., Grills, I., O’Connell, N., Sonke, J.-J., 2017a. Dose to heart substructures is associated with non-cancer death after SBRT in stage I–II NSCLC patients. *Radiotherapy and Oncology* 123, 370–375.
- Stam, B., van der Bijl, E., van Diessen, J., Rossi, M.M.G., Tjhuis, A., Belderbos, J.S.A., Damen, E., Sonke, J.-J., 2017b. Heart dose associated with overall survival in locally advanced NSCLC patients treated with hypofractionated chemoradiotherapy. *Radiother Oncol* 125, 62–65.
<https://doi.org/10.1016/j.radonc.2017.09.004>
- Stereotactic radiosurgery for trigeminal neuralgia using the gamma knife | Guidance and guidelines | NICE URL <https://www.nice.org.uk/guidance/ipg85> (accessed 2.18.19).
- Stevenson, W.G., Wilber, D.J., Natale, A., Jackman, W.M., Marchlinski, F.E., Talbert, T., Gonzalez, M.D., Worley, S.J., Daoud, E.G., Hwang, C., Schuger, C., Bump, T.E., Jazayeri, M., Tomassoni, G.F., Kopelman, H.A., Soejima, K., Nakagawa, H., 2008. Irrigated Radiofrequency Catheter Ablation Guided by Electroanatomic Mapping for Recurrent Ventricular Tachycardia After Myocardial Infarction: The Multicenter Thermocool Ventricular Tachycardia Ablation Trial. *Circulation* 118, 2773–2782. <https://doi.org/10.1161/CIRCULATIONAHA.108.788604>
- Stewart, J.R., Fajardo, L.F., 1978. Cancer and coronary artery disease. *Int. J. Radiat. Oncol. Biol. Phys.* 4, 915–916.

- Thwaites, D., 2013. Accuracy required and achievable in radiotherapy dosimetry: have modern technology and techniques changed our views? *J. Phys.: Conf. Ser.* 444, 012006. <https://doi.org/10.1088/1742-6596/444/1/012006>
- Timmerman, R., Galvin, J., Michalski, J., Straube, W., Ibbott, G., Martin, E., Abdulrahman, R., Swann, S., Fowler, J., Choy, H., 2006. Accreditation and quality assurance for Radiation Therapy Oncology Group: Multicenter clinical trials using Stereotactic Body Radiation Therapy in lung cancer. *Acta Oncologica* 45, 779–786. <https://doi.org/10.1080/02841860600902213>
- Timmerman, R., Papiez, L., McGarry, R., Likes, L., DesRosiers, C., Frost, S., Williams, M., 2003. Extracranial stereotactic radioablation: results of a phase I study in medically inoperable stage I non-small cell lung cancer. *Chest* 124, 1946–1955.
- Timmerman, R.D., 2008. An overview of hypofractionation and introduction to this issue of seminars in radiation oncology. *Semin Radiat Oncol* 18, 215–222. <https://doi.org/10.1016/j.semradonc.2008.04.001>
- Tino, R.B., Yeo, A.U., Brandt, M., Leary, M., Kron, T., 2022. A customizable anthropomorphic phantom for dosimetric verification of 3D-printed lung, tissue, and bone density materials. *Medical Physics* 49, 52–69. <https://doi.org/10.1002/mp.15364>
- Torras, M.G., Fundowicz, M., Aliste, L., Asensio, E., Boladeras, A.M., Borràs, J.M., Carvalho, L., Castro, C., Deantonio, L., Konstanty, E., Krengli, M., Kruszyna, M., Lencart, J., Macià, M., Marín, S., Muñoz-Montplet, C., Pisani, C., Pinto, D., Puigdemont, M., Guedea, F., Aguiar, A., Milecki, P., Malicki, J., 2017. Improving radiation oncology through clinical audits: Introducing the IROCA project. *Rep Pract Oncol Radiother* 22, 408–414. <https://doi.org/10.1016/j.rpor.2017.07.004>
- UK SABR Consortium Guidance v6.1, January 2019. <https://www.sabr.org.uk/wp-content/uploads/2019/04/SABRconsortium-guidelines-2019-v6.1.0.pdf> (accessed 09.02.22)
- Venkatesulu BP, Mallick S, Lin SH, Krishnan S. A systematic review of the influence of radiation-induced lymphopenia on survival outcomes in solid tumors. *Crit Rev Oncol Hematol*. 2018 Mar;123:42-51. doi: 10.1016/j.critrevonc.2018.01.003. Epub 2018 Feb 2. PMID: 29482778.
- Venables, K., Winfield, E., Deighton, A., Aird, E., Hoskin, P., group, on behalf of the S.T. manage, 2001. The START Trial - measurements in semi-anatomical breast and chest wall phantoms. *Phys. Med. Biol.* 46, 1937–1948. <https://doi.org/10.1088/0031-9155/46/7/314>

- Veselka, J., Jensen, M.K., Liebrechts, M., Januska, J., Krejci, J., Bartel, T., Dabrowski, M., Hansen, P.R., Almaas, V.M., Seggewiss, H., Horstkotte, D., Tomasov, P., Adlova, R., Bundgaard, H., Steggerda, R., ten Berg, J., Faber, L., 2016. Long-term clinical outcome after alcohol septal ablation for obstructive hypertrophic cardiomyopathy: results from the Euro-ASA registry. *European Heart Journal* 37, 1517–1523. <https://doi.org/10.1093/eurheartj/ehv693>
- Wang JL, Ma R, Kong W, Zhao R, Wang YY. Lymphopenia in Esophageal Cancer: What Have We Learned? *Front Oncol.* 2021 Mar 11;11:625963. doi: 10.3389/fonc.2021.625963. PMID: 33791213; PMCID: PMC8006429.
- Wang, Y., Riederer, S.J., Ehman, R.L., 1995. Respiratory Motion of the Heart: Kinematics and the Implications for the Spatial Resolution in Coronary Imaging. *Magn. Reson. Med.* 33, 713–719. <https://doi.org/10.1002/mrm.1910330517>
- Wilcox, E.E., Daskalov, G.M., 2007. Evaluation of GAFCHROMIC® EBT film for CyberKnife® dosimetry. *Medical Physics* 34, 1967–1974. <https://doi.org/10.1118/1.2734384>
- Yamamoto, M., Serizawa, T., Shuto, T., Akabane, A., Higuchi, Y., Kawagishi, J., Yamanaka, K., Sato, Y., Jokura, H., Yomo, S., Nagano, O., Kenai, H., Moriki, A., Suzuki, S., Kida, Y., Iwai, Y., Hayashi, M., Onishi, H., Gondo, M., Sato, M., Akimitsu, T., Kubo, K., Kikuchi, Y., Shibasaki, T., Goto, T., Takanashi, M., Mori, Y., Takakura, K., Saeki, N., Kunieda, E., Aoyama, H., Momoshima, S., Tsuchiya, K., 2014. Stereotactic radiosurgery for patients with multiple brain metastases (JLGK0901): a multi-institutional prospective observational study. *Lancet Oncol.* 15, 387–395. [https://doi.org/10.1016/S1470-2045\(14\)70061-0](https://doi.org/10.1016/S1470-2045(14)70061-0)
- Ze Paul C., Mak Raymond, 2019. Noninvasive Stereotactic Radioablation for Ventricular Tachycardia. *Circulation* 139, 322–324. <https://doi.org/10.1161/CIRCULATIONAHA.118.038285>
- Zhang, J., Yang, M., Zhou, M., He, L., Chen, N., Zakrzewska, J.M., 2013. Non-antiepileptic drugs for trigeminal neuralgia. *Cochrane Database of Systematic Reviews*. <https://doi.org/10.1002/14651858.CD004029.pub4>
- Zhao, D.-S., Shen, Y., Zhang, Q., Lin, G., Lu, Y.-H., Chen, B.-T., Shi, L.-S., Huang, J.-F., Lu, H.-H., 2016. Outcomes of catheter ablation of atrial fibrillation in patients with hypertrophic cardiomyopathy: a systematic review and meta-analysis. *Europace* 18, 508–520. <https://doi.org/10.1093/europace/euv339>

Appendix I: Stakeholder engagement exercise

For this work I have engaged widely with stakeholders in the design of the phantom itself and the design of the radiotherapy targets, however here I examine the views on this innovation from potential end-users interested in cardiac SABR patient safety. I held recorded structured interviews between 30 and 60 minutes with colleagues from cardiology at Barts Health and from UK centralised radiotherapy quality assurance group. The key excerpts presented illustrate the benefits of this innovation as a vehicle to safe implementation of cardiac SABR in the UK and beyond.

AI.1 Patty Diez interview excerpt

CD: So why don't you start off by telling me your role?

PD: I am lead clinical scientist in RTTQA national radiotherapy trials quality assurance group. We do quality assurance for any clinical trial that involves any radiotherapy within the NIHR portfolio. We ensure that centres comply with the protocol of the trial so that patients get a safe treatment but also we're trying to ensure there's consistency between all the centres that are participating to ensure that the radiotherapy is being delivered to the standard required by that trial protocol... We do external dosimetry audits and, we do it differently whether it's for SABR or not.

CD: And maybe you could tell me on what basis was that made?

PD: It was mostly to do with the difference in doses and dose gradients that we deliver in SABR versus what we deliver in conventional radiotherapy, we have very steep dose gradients and delivering very high doses per fraction [for SABR], so you want to make sure that what you've been planning you can deliver, that your machines can actually reproduce those dose gradients correctly... You have very high doses and in not many fractions. If one of those fractions is given in the wrong place, you have lost a big chunk of your treatment, plus also obviously potentially delivered that that dose to an organ at risk that you were also, especially in SABR, we plan to tolerance of those constraints most of the time.

CD: In terms of the thinking on those lines of complexity, do you do you think there's a need for cardiac SABR specific quality assurance in your experience?

PD: I would say yes. I mean, I think the delivery is... very different and the volumes are different. We are targeting where has always been an organ at risk with a very high dose and it's also an organ that is beating so it would make me a lot happier if there was QA for sure.

CD: Do you see any benefits just in terms of the anthropomorphic nature in terms of testing using the kind of imaging and that they would use on treatment? Is that a key part of SABR QA in your in your opinion?

PD: I think it'd be worth it yes, definitely. In the in the area for cardiac you won't be relying on things like ribs. But yeah, you wanna definitely test that they're seeing what they need to see to be able to deliver that treatment.

CD: If you were setting up [a cardiac SABR] centralized QA service, what metrics might you use and what ... do you think are the critical things to test in that in that plan delivery?

PD: I mean you are looking at small field dosimetry. You've got steep dose gradients and so you want to make sure that that the dose that is being delivered to that point is correct and ... that the dose gradient is appropriate, which you can't obviously see if you just measuring one point in the middle... and so ... gamma indices... and distance to agreement... those are the two that we use.

CD: You mentioned the spinal SABR [phantom] you had modified specifically for centralized QA purposes, maybe you want to comment on the kind of configurability [required] from an RTTQA perspective.

PD: Our main issue will be that we don't have an audit where we would be able to test delivery in motion and everything that we have at the moment is static. Generally, there's been something that was out there, but we've been able to then make modifications with the company and I think with something complex ... we would have to consider all options ... because we haven't assessed it at all yet. A piece of anthropomorphic phantom that doesn't do anything is very costly ... I don't know that we would want to compromise that warranty [and] then you would need plenty of time in advance to make sure that that was delivered to you how you wanted it.

CD: Yeah, or you work with someone, that has already done those modifications and can provide you with a 3D print of a something ... knowing the fact that it can be reconfigured very straightforwardly by just doing another 3D print.

PD: Yes, that sounds a very good option too. To be honest, we have been discussing after the last two [phantoms] that we've bought that next time it'd be worth 3D printing and not bothering with companies... So yes, we'll be very interested in seeing what you've got.

AI.1 Oliver Guttman interview excerpt

CD: So kick us off by introducing yourself and tell us a bit about your role?

OG: My name is Oliver Guttman, I am a consultant cardiologist specialising in inflammatory and inherited heart muscle diseases, which include hypertrophic cardiomyopathy and as part of this I do alcohol septal ablations which is one of the treatments for left ventricular outflow tract obstructive disease.

CD: And for this disease maybe could give us your view on current treatments for that?

OG: Treatments are medical therapy, pacemaker or alcohol septal ablation. Invasive alcohol ablation is for patients that have obstructive disease. We gain access via the wrist or the groin to the septal artery. If we find a vessel that goes to the right place and not anywhere else, we would inject alcohol for approximately 8 minutes. This causes a localised heart attack and over the next 6-12 months the thickened heart muscle decreases, opening the orifice and that should improve the patient symptoms. We quote a risk of 0.5-1% for most symptoms and of approximately 10% for damage to conduction the conduction system.

CD: For those patients that do proceed to this treatment maybe you could say something about the accuracy of the current treatment, how much control do you feel you have in terms of where the alcohol is going and where the scar will eventually manifest itself?

OG: All are based on experience, but we don't have the ability to pinpoint the target... compared with MRI and CT it's not very precise. We also don't have any data on how much alcohol to give. We give 0.1 ml per mm of thickness, but this is empirical and it's based on the experience of the operator. It's not very precise.

CD: On inter-operator variability, do you collect data for complexity of the target, thickness, etc and attempt to correlate with outcome?

OG: We collect lots of data, but the issue is with a symptom based-outcome, over a time course where the patient might change between the procedure and the next 6-12 months. We put a pacemaker in to patients and so there are many confounders.

CD: Thinking about cardiac SABR, what do you see as the main benefits of cardiac SABR from your clinical perspective compared with existing methods?

OG: The precision of where to target is dramatically improved. With the techniques you have developed, it would be amazing if you could really pinpoint the area you want to target without causing damage to any other areas. The other thing of course is that it's much less invasive, if everything goes well, patients don't have to have open heart surgery, patients don't have to be in hospital, you don't have to achieve access from the wrist. If this goes well it would be a miracle treatment to treat patients more precisely, targeting what you want and they could come in in the morning and go home in the evening.

CD: you mentioned the precision, based on your clinical experience, do you have a feel for the level of precision you suspect you would need in order to achieve success?

OG: At the moment with our techniques, we are probably talking about 0.5 to 1 cm for what we can achieve, but if we can go down to the millimetres, that is dramatically improved. Also what we definitely know from alcohol ablation is that for some patients, the subsequent formation of the scar shows a ridge where the alcohol couldn't get to but we can't see that precisely when we do the procedure [from the contrast angiography]. Very often areas of the thickened bit are not targeted with the alcohol ... and this will then affect the anatomy of the heart and can sometimes not achieve the desired effect. If you can pinpoint that area as a whole without leaving any gaps, that's the advantage of the SABR.

CD: If cardiac SABR wasn't available for patients that are screened out of alcohol ablation, what are the alternatives?

OG: If they are not suitable for interventional therapy then most times it's supportive therapy when we often put a pacemaker or just medication and tell patients that they just have to live with those symptoms.

CD: So having a non-invasive day procedure [cardiac SABR] would be beneficial to those patients?

OG: Yes

CD: Is there anything you want to add?

OG: I think the truth is that we are all hoping that a non-invasive way of treating this will revolutionise the way we look after this.

Appendix II: Taught Programme Elements

DClinSci Appendix – List of AMBS A units and Medical Physics B units together with assignments – Christopher Dean

AMBS – A Units			
Unit title	Credits	Assignment wordcount	
A1: Professionalism and professional development in the healthcare environment	30	Practice paper – 2000 words A1 – assignment 1 – 1500 words A1 – assignment 2 – 4000 words	
A2: Theoretical foundations of leadership	20	A2 – assignment 1 – 3000 words A2 – assignment 2 – 3000 words	
A3: Personal and professional development to enhance performance	30	A3 – assignment 1 – 1500 words A3 – assignment 2 – 4000 words	
A4: Leadership and quality improvement in the clinical and scientific environment	20	A4 – assignment 1 – 3000 words A4 – assignment 2 – 3000 words	
A5: Research and innovation in health and social care	20	A5 – assignment 1 – 3000 words A5 – assignment 2 – 3000 words	
Medical Physics – B Units			
B1: Medical Equipment Management	10	2000 word assignment	
B2: Clinical and Scientific Computing	10	2000 word assignment	
B3: Dosimetry	10	Group presentation 1500 word assignment	
B4: Optimisation in Radiotherapy and Imaging	10	Group presentation 1500 word assignment	
B6: Medical statistics in medical physics	10	3000 word assignment	
B8: Health technology assessment	10	3000 word assignment	
B9: Clinical applications of medical imaging technologies in radiotherapy physics	20	Group presentation 2000 word assignment	
B10a: Advanced Radiobiology	10	Virtual experiment + 1500 word report	
B10c: Novel and specialised external beam radiotherapy	10	1500 word report/piece of evidence for portfolio	
B10e: Novel imaging techniques	10	1500 word report/piece of evidence for portfolio	
Generic B Units			
B5: Contemporary issues in healthcare science	20	1500 word assignment + creative project	
B7: Teaching Learning Assessment	20	20 minute group presentation	
Section C			
C1: Innovation Project	70	4000-5000 word Literature Review Lay Presentation	